TECHNISCHE UNIVERSITÄT MÜNCHEN

TUM School of Computation, Information and Technology

Contrast and resolution in radiofrequency induced thermoacoustic imaging

Yuanhui Huang

Acknowledgements

I gained my One Piece in the journey, and I have always been so grateful. Along the journey, I have worked and partied with great people. Their lovely personalities and vivid images were shining during the hard times and will be shining through the future highs and lows: Dr. Juan Pablo Fuenzalida Werner, Dr. Weili Tian, Dr. Lucas Riobó, Dr. Lu Ding, Dr. Hsiao-Chun Amy Lin, Dr. Ivan Olefir, Dr. Georg Wissmeyer, Dr. Christian Zakian, Dr. Paul Vetschera, Dr. Hans-Peter Wieser, Dr. Julie Lascaud, Dr. Xiaopeng Ma, Dr. Jiangli Zhang, Dr. Jin Gao, Dr. Zhe Ji, Dr. Yue Li, Dr. Gael Diot, Jannis Schauer, Dr. Susanne Stern, Sarah Glasl, Dr. Bingwen Wang, and so many others. I thank you all. To the names only appeared on media, papers and books, thank you for sharing your stories of exploration.

To see and experience everything together with my loving wife Dr. Hong Yang, is an ecstasy beyond languages. To my parents, brothers and sisters, friends in China, thank you for looking after me. I am loving you all and see you all in the future. The PhD journey ends here, and many more adventures await. Here and now that I have experienced, labors my ideals in mind into the future reality.

Abstract

Thermoacoustic wave is induced by thermal expansion due to the absorption of various energy forms, such as photons, accelerated particles, and radio frequency (RF). RF induced thermoacoustics is of interest because RF below hundreds of megahertz can penetrate into tissue deeper than photons and microwave. Combined with the penetration and imaging resolution of ultrasound, thermoacoustic imaging could find broad biomedical applications. However, whether and how the thermoacoustic contrast can resolve anatomical or functional information remained unknown.

In this dissertation, in order to foster the further application of thermoacoustic technology, high-sensitive and high-resolution RF induced thermoacoustic imaging methods are studied. I developed sensing modalities and investigated whether RF fields with wavelengths exceeding 10 meters can enable imaging of small conductivities in mice and fish. Exploiting the second harmonic generation of thermoacoustic waves, for the first time, RF energy can be used for high-resolution label-free blood vessel visualization based on the difference in electrical conductivity between blood and surrounding tissues. To study the microscopic cause of thermoacoustic contrast, I built a thermoacoustic microscope based on transmission line design to 'concentrate' RF energy and revealed with high signal-to-noise ratio the unseen-before millimeter-scale distribution of free ions in zebrafish embryo and larva.

In summary, thermoacoustics was shown with capability to deliver non-invasive blood-to-muscle contrast macroscopically, rich details microscopically, high dynamic range of conductivity detection, and the ability to perform simultaneous RF-induced passive ultrasound imaging. These results support the suitability of thermoacoustics as a promising method for high-resolution, label-free assessment of tissue conductivity in biomedical applications.

Zusammenfassung

Thermoakustische Wellen werden durch Wärmeausdehnung aufgrund der Absorption verschiedener Energieformen wie Photonen, beschleunigten Teilchen und Hochfrequenz (HF) induziert. Die HF-induzierte Thermoakustik ist von Interesse, da HF, die geringer ist als einige hundert Megahertz, tiefer in Gewebe eindringen kann als Photonen und Mikrowellen. In Kombination mit der Durchdringung und Bildauflösung von Ultraschall könnte die thermoakustische Bildgebung breite biomedizinische Anwendungen finden. Ob und wie der thermoakustische Kontrast jedoch anatomische oder funktionelle Informationen auflösen kann, ist bislang noch unbekannt.

In dieser Dissertation werden hochempfindliche und hochauflösende HF-induzierte thermoakustische Bildgebungsverfahren untersucht, um die weitere Anwendung der thermoakustischen Technologie zu fördern. Ich habe Sensormodalitäten entwickelt und untersucht, ob HF-Felder mit Wellenlängen von mehr als 10 Metern die Abbildung kleiner Leitfähigkeiten bei Mäusen und Fischen ermöglichen können. Durch die Nutzung von Frequenzverdopplung (englisch Second Harmonic Generation) thermoakustischer Wellen kann HF-Energie zum ersten Mal für eine hochauflösende, markierungsfreie Visualisierung von Blutgefäßen verwendet werden, basierend auf dem Unterschied der elektrischen Leitfähigkeit zwischen Blut und umgebendem Gewebe. Um die mikroskopische Ursache des thermoakustischen Kontrasts zu untersuchen, baute ich ein Thermoakustisches Mikroskop basierend auf einem Übertragungsleitungsdesign. So konnte ich die HF-Energie „konzentrieren" und zeigte mit einem hohen Signal-Rausch-Verhältnis erstmalig die millimetergroße Verteilung freier Ionen in Zebrafischembryonen und Larven.

Zusammenfassend lässt sich sagen, dass die Thermoakustik makroskopisch einen nicht-invasiven Blut-Muskel-Kontrast, mikroskopischen Detailreichtum, einen hohen Dynamikbereich der Leitfähigkeitsdetektion und die Fähigkeit zur simultanen HF-induzierten passiven Ultraschallbildgebung ermöglicht. Diese Ergebnisse unterstreichen die Eignung der Thermoakustik als vielversprechende Methode zur hochauflösenden, markierungsfreien Bewertung der Gewebeleitfähigkeit in biomedizinischen Anwendungen.

List of publications

This thesis is a publication-based dissertation upon (<u>equal contribution</u>):
1. Y. Huang, M. Omar, W. Tian, H. Lopez-Schier, G. G. Westmeyer, A. Chmyrov, G. Sergiadis, V. Ntziachristos, Noninvasive visualization of electrical conductivity in tissues at the micrometer scale. Science Advances 7, eabd1505 (2021).
2. <u>Y. Huang, S. Kellnberger</u>, G. Sergiadis, V. Ntziachristos, Blood vessel imaging using radiofrequency-induced second harmonic acoustic response. Sci. Rep. 8, 15522 (2018).

And all my following contributions deepened my understanding of the problem:
3. <u>J. Schauer, H.-P. Wieser</u>, Y. Huang, H. Ruser, J. Lascaud, M. Würl, A. Chmyrov, M. Vidal, J. Herault, V. Ntziachristos, W. Assmann, K. Parodi, Günther Dollinger. Proton beam range verification by means of ionoacoustic measurements at clinically relevant doses using a correlation-based evaluation. Frontiers in Oncology 12:925542 (2022).
4. <u>K. Mishra, J. P. Fuenzalida Werner, F. Pennacchietti</u>, R. Janowski, A. Chmyrov, Y. Huang, C. Zakian, U. Klemm, I. Testa, D. Niessing, V. Ntziachristos, A. C. Stiel, Genetically encoded photo-switchable molecular sensors for optoacoustic and super-resolution imaging. Nature Biotechnology (2021).
5. <u>H.-P. Wieser, Y. Huang, J. Schauer, J.</u> Lascaud, M. Wuerl, S. Lehrack, D. Radonic, M. Vidal, J. Herault, A. Chmyrov, V. Ntziachristos, W. Assmann, K. Parodi, G. Dollinger, Experimental demonstration of accurate Bragg Peak localization with ionoacoustic Tandem Phase Detection (iTPD). Physics in Medicine and Biology (2021).
6. N. Liu, V. Gujrati, J. Malekzadeh-Najafabadi, J. P. F. Werner, U. Klemm, L. Tang, Z. Chen, J. Prakash, Y. Huang, A. Stiel, G. Mettenleiter, M. Aichler, A. Blutke, A. Walch, K. Kleigrewe, D. Razansky, M. Sattler, V. Ntziachristos, Croconaine-based nanoparticles enable efficient optoacoustic imaging of murine brain tumors. Photoacoustics 22, 100263 (2021).
7. <u>J. P. Fuenzalida Werner, Y. Huang</u>, K. Mishra, R. Janowski, P. Vetschera, C. Heichler, A. Chmyrov, C. Neufert, D. Niessing, V. Ntziachristos, A. C. Stiel, Challenging a Preconception: Optoacoustic Spectrum Differs from the Optical Absorption Spectrum of Proteins and Dyes for Molecular Imaging. Analytical Chemistry 92, 10717-10724 (2020).
8. K. Mishra, M. Stankevych, J. P. Fuenzalida-Werner, S. Grassmann, V. Gujrati, Y. Huang, U. Klemm, V. R. Buchholz, V. Ntziachristos, A. C. Stiel, Multiplexed whole-animal imaging with reversibly switchable optoacoustic proteins. Science Advances 6, eaaz6293 (2020).
9. J. P. Fuenzalida Werner, K. Mishra, Y. Huang, P. Vetschera, S. Glasl, A. Chmyrov, K. Richter, V. Ntziachristos, A. C. Stiel, Structure-Based Mutagenesis of Phycobiliprotein smURFP for Optoacoustic Imaging. ACS Chemical Biology 14, 1896-1903 (2019).

10. K. Tamarov, M. Gongalsky, L. Osminkina, Y. Huang, M. Omar, V. Yakunin, V. Ntziachristos, D. Razansky, V. Timoshenko, Electrolytic conductivity-related radiofrequency heating of aqueous suspensions of nanoparticles for biomedicine. Physical Chemistry Chemical Physics 19, 11510-11517 (2017).

List of figures

List of tables

List of abbreviations

CT	Compter tomography
CW	Continuous wave
DAQ	Data acquisition
DBS	Deep brain stimulation
DI	De-ionized water
EM	Electromagnetics
FG	Function generator
FOV	Field of view
FRET	Förster resonance energy transfer
FWHM	Full width at half maximum
HF	High frequency
IONA	Ionoacoustics
MASER	Microwave amplification by stimulated emission of radiation
MRI	Magnetic resonance imaging
MW	Microwave
NDT	Non-destructive test
OA	Optoacoustics
PA	Photoacoustics
PE	Polyethylene
PRR	Pulse repetition rate
PVC	Polyvinyl chloride
RF	Radio frequency
RISHA	Radiofrequency induced second harmonic acoustics
RSOM	Raster-scan optoacoustic mesoscopy
SHG	Second harmonic generation
SNR	Signal-to-noise ratio
TA	Thermoacoustics
US	Ultrasound

Table of contents

1. Introduction

1.1 Thermoacoustics

Thermoacoustics (TA) [1, 2] is a general term encompassing radio frequency (RF) induced thermoacoustics [3, 4], microwave (MW) induced thermoacoustics [5, 6], accelerated charge particles induced ionoacoustics [7, 8] (IONA, protoacoustics [9]), optoacoustics [10, 11] (OA, photoacoustics or PA [12-14]), and etc. All the above-mentioned include a process of acoustic wave generation induced by thermal expansion (*section 1.2*). The major difference resides in the absorption mechanism (*section 1.3*) of the specific energy form that deposits substantial amount of transient heat in subject.

The most perceived concept is photoacoustic effect [12]. It describes the phenomenon of acoustic wave generation due to light absorption. Since the first report by Alexander Graham Bell [12] in 1881, it is not until 1973 that photoacoustics had been used for the studies of biological tissues by Allan Rosencwaig [13]. And only on the advent of pulsed laser technology being able to deliver high peak power pulses, photoacoustics found profound developments and broad applications in spectroscopy and imaging [15].

Microwave (>gigahertz, GHz) induced thermoacoustics, due to the immediate availability of microwave source and antenna, has seen major developments [5, 6] as well since first time reported by Theodore Bowen [1, 2] in 1981. But it is still limited in terms of sensitivity and imaging resolution due to the lack of high peak power source [like MASER (microwave amplification by stimulated emission of radiation, a counterpart of laser in the microwave range [16])]. Nonetheless, microwave induced thermoacoustics has found applications in imaging of breast cancer, inflammatory arthritis in joints [17], and *in vitro* tests of polar molecules [18], and etc..

In lower range of a few megahertz (MHz), radio frequency induced thermoacoustics using nearfield coupling was proposed and developed since 2010 to overcome the challenges of the limited sensitivity and imaging resolution [3, 19-21] in microwave induced thermoacoustics. Nearfield RF coupling enables substantial energy density deposited in sample, and therefore led to my developments in the macroscopic high-sensitivity blood vessel imaging [22] (*Chapter 2*), and high imaging resolution of a few micrometers in small model animal[23] (*Chapter 3*). Now we start to see the wonderful biological world in the eyes of radio frequencies.

As I marched towards advancing the understanding of the fundamentals of nearfield thermoacoustics, and its applications in life science, there were fundamental questions appeared and some of them intertwined. For example, reducing the pulse width of RF excitation increases imaging resolution [24] but reduces the sensitivity due to the limited peak power of RF pulser. We therefore choose to separate the problems and solve them piece by piece. These problems are: intrinsic biological contrast

source (*section 1.5.1*), resolution limit (*section 1.5.2*), and high RF coupling efficiency for detections of high signal-to-noise ratio (SNR, *section 1.6*). The following of this chapter is meant to provide a theory background (*sections 1.2–1.3*), the rationale (*section 1.4*), the methodology (*section 1.6*) to approach the research questions, and my summary and outlook towards future developments (*section 1.7*).

1.2 Thermoacoustic wave generation

A fundamental understanding of the physics of thermoacoustic wave generation could guide the engineering practice in harnessing radiofrequency induced thermoacoustics for novel imaging applications. The following theory background is provided towards a better understanding of thermoacoustic contrast mechanisms.

1.2.1 Time domain

The ultrasound (US) propagates in homogeneous media (assuming medium density ρ_0 constant) can be described by the wave equation [25]:

$$\nabla^2 p(\boldsymbol{r}, t) - \frac{1}{c_s^2} \frac{\partial^2 p(\boldsymbol{r}, t)}{\partial^2 t} = 0, \tag{1}$$

where $p(\boldsymbol{r}, t)$ is the acoustic pressure wave (Pa, J/m^3, or N/m^2) dependent on the spatial location $\boldsymbol{r}$ at a specific time t; ∇^2 denotes the Laplacian operator ($\nabla \cdot \nabla$) given by the divergence of the gradient of the acoustic pressure in space; ∂ is the differential symbol; and c_s is speed of sound in the medium.

A thermoacoustic wave is generated if there is a temperature change (T in Kelvin). Thus the homogeneous wave equation becomes the one with source [25]. The thermoacoustic wave equation can be derived as following from the combination of the generalized Hooke's law (thermal expansion equation) and Newton's second law of motion (the linear inviscid force equation, ignoring kinematic viscosity) [25, 26].

The fractional volume expansion, indicated by medium displacement $\xi(\boldsymbol{r}, t)$ which can be induced by force and by temperature, is written as:

$$\nabla \cdot \xi(\boldsymbol{r}, t) = -\kappa p(\boldsymbol{r}, t) + \beta T(\boldsymbol{r}, t). \tag{2}$$

The force applied to unit volume equals to the mass times the displacement:

$$\nabla p(\boldsymbol{r}, t) = -\rho \frac{\partial^2 \xi(\boldsymbol{r}, t)}{\partial^2 t}. \tag{3}$$

Here κ is the isothermal compressibility (Pa^{-1}) indicating the relative volume change when given pressure change at constant temperature:

$$\kappa = \frac{C_P}{\rho c_s^2 C_V}; \tag{4}$$

β is the thermal expansion coefficient (K^{-1}) indicating the volume change in response to temperature change; ρ is the density of medium (kg/m^3); C_V is the specific heat capacity per unit volume in unit of J/(kg·K); and C_p is the specific heat capacity at constant pressure (isobaric).

Taking the divergence of *Eq. (3)* and substitute into *Eq. (2)* yields the general thermoacoustic wave equation:

$$\nabla^2 p(\boldsymbol{r},t) - \frac{1}{c_s^2}\frac{\partial^2 p(\boldsymbol{r},t)}{\partial^2 t} = -\frac{\beta}{\kappa c_s^2}\frac{\partial^2 T(\boldsymbol{r},t)}{\partial t^2}. \tag{5}$$

The temperature change can be caused by various energy forms, such as nonionizing electromagnetic (EM) radiations like light, microwave, radio frequencies, and ionizing accelerated charged particles and radiation, or by thermal conduction. Assuming the homogeneous medium is even isotropic, the temperature change can be described by heat equation:

$$\frac{\partial T(\boldsymbol{r},t)}{\partial t} = \frac{1}{\rho C_V}\big(H(\boldsymbol{r},t) + k\nabla^2 T(\boldsymbol{r},t)\big), \tag{6}$$

where k is the thermal conductivity in unit of W/(m·K); and $H(\boldsymbol{r},t)$ is the heating function denoting the thermal energy deposited in unit volume and unit time (W/m³).

The thermoacoustic wave equation expressed in both source terms of the heating function and the thermal conduction is therefore:

$$\nabla^2 p(\boldsymbol{r},t) - \frac{1}{c_s^2}\frac{\partial^2 p(\boldsymbol{r},t)}{\partial^2 t} = -\frac{\beta}{\rho C_V \kappa c_s^2}\frac{\partial^2\big(H(\boldsymbol{r},t) + k\nabla^2 T(\boldsymbol{r},t)\big)}{\partial t^2}. \tag{7}$$

In photoacoustics [25], if given sufficiently short pulses of laser excitation, the thermal confinement is usually considered satisfied (the thermal conduction term is negligible). The heat equation is therefore further simplified yielding the classic photoacoustic wave equation:

$$\left(\frac{\partial^2}{\partial^2 t} - c_s^2 \cdot \nabla^2\right)\cdot p(\boldsymbol{r},t) = \Gamma\frac{\partial H(\boldsymbol{r},t)}{\partial t}, \tag{8}$$

where Γ is the dimensionless Grüneisen parameter indicating the conversion efficiency from heat energy to pressure / kinetic energy, and

$$\Gamma = \frac{\beta}{\rho C_V \kappa} = \frac{\beta c_s^2}{C_p}. \tag{9}$$

It is to be noted that *Eq. (8)* holds only when the heating function has a considerably short pulse width, thus the thermal confinement is met. Thermal confinement is defined by the thermal relaxation time:

$$\tau_{th} = \frac{d^2}{\alpha} = \frac{d^2}{\frac{k}{\rho C_p}}. \tag{10}$$

Here *d* is determined by the interested dimension of the sample, assuming the penetration of the used energy form is deeper than the sample of interest; and α is thermal diffusivity (m²/s).

In addition, the stress confinement that is determined by the stress relaxation time, τ_s, should also be met if high imaging resolution is required, i.e., eliminating the effect of the pulse shape of the heating function by using pulse width shorter than:

$$\tau_s = \frac{d}{c_s}. \tag{11}$$

Satisfying both the thermal and stress confinements, the energy source function $[H(\mathbf{r})$, J/m^3] is a delta pulse at t=0. Given the initial conditions, the general photoacoustic wave equation, *Eq. (8)*, as a Cauchy problem can be solved by using the forward Green's function method [25, 27]:

$$p(\mathbf{r}, t) = \frac{\Gamma}{4\pi} \int_V \frac{\partial}{\partial t} \frac{H_r(\mathbf{r}')}{|\mathbf{r}-\mathbf{r}'|} d^3\mathbf{r}'. \tag{12}$$

Upon such delta heating, the initial pressure wave that is generated is:

$$p_0(\mathbf{r}) = \Gamma \cdot H(\mathbf{r}). \tag{13}$$

Table 1. Thermal dynamic properties of some materials.

Material	σ at 20 °C S/m	ρ kg/m^3	C_p J/(kg·K)	k W/(m·K)	α m^2/s
Air	<8.0×10^{-15}	1.3	1 004	0.03	19.2
PVC	1.0×10^{-10}	1 500	1 674	0.17	0.07
H$_2$O	5.5×10^{-6}	1 000	4 184	0.60	0.14
Skin	1.7×10^{-1}	1 000	2 500	0.40	0.16
Fe	1.0×10^7	7 870	448	72	20.4
Cu	5.96×10^7	8 940	385	396	115
Au	4.10×10^7	19 300	128	320	129

In radiofrequency induced thermoacoustics, however, the above assumption does not hold for complex samples of both liquid and solid or air phases, where thermal conductivity is high for solid metal and low for liquid *(Table 1)*.

If no delta heating function and thermal confinement is assumed, i.e., thermal diffusion taken into account, *Eq. (5)* and *Eq. (6)* combined [28] is solved by using Greens function, resulting in:

$$p(\mathbf{r}, t) = \frac{\beta}{4\pi C_p} \int_V \frac{\partial}{\partial t} \frac{[H(\mathbf{r}', t) + k\nabla^2 T(\mathbf{r}', t)]}{|\mathbf{r}-\mathbf{r}'|} d^3\mathbf{r}'. \tag{14}$$

Equation (14) is a more general solution to the thermoacoustic wave equation saying that the thermoacoustic pressure wave generated is results of the time derivative of both the heating function and spatial heat diffusion.

The thermal conductivity term is explicitly expressed here because there might be further relation between the heating and diffusion if Joule heating due to conductivity absorption is involved [29-31]. For metal or materials of high electrical conductivity, there is empirical Wiedemann–Franz law [32] states that the ratio of the electronic

contribution of the thermal conductivity to the electrical conductivity (σ) of a metal is proportional to the temperature using electronic conduction model:

$$\frac{\kappa}{\sigma} = \text{L}T = \frac{\pi^2}{3}\left(\frac{k_B}{e}\right)^2 T,$$ (15)

where the constant L is known as Lorentz number (2.44×10^{-8} WΩK^{-2}); k_B is the Boltzmann constant (1.38×10^{-23} J·K^{-1}); and e here is the charge of an electron (1.6×10^{-19} Coulombs).

1.2.2 Frequency domain

In Fourier domain, thermoacoustic wave equation, *Eq. (7)*, is transformed into an inhomogeneous Helmholtz equation [33], with the time-dependent functions being expressed in frequency spectrum components $p(r,t) = \tilde{p}(r,\omega)e^{i\omega t}$:

$$\nabla^2 \tilde{p}(r,\omega) - \tilde{k}^2 \tilde{p}(r,\omega) = -\frac{i\omega\beta}{C_P}[H(r,\omega) + k\nabla^2 T(r,\omega)].$$ (16)

Here $\omega/c_s = \tilde{k}$ is the acoustic wave number and ω is the angular frequency. Solving the Helmholtz equation using Green's function (in unbounded media) yields the solution of pressure field in Fourier domain [33]:

$$\tilde{p}(r,\omega) = -\frac{i\omega\beta}{4\pi C_P}\int_V \frac{e^{i\tilde{k}|r-r'|}}{|r-r'|}[H(r,\omega) + k\nabla^2 T(r,\omega)]d^3r'.$$ (17)

1.2.3 Second harmonic generation

The frequency domain result indicates second harmonic generation (SHG). Electrically conductive materials, when exposed to continuous wave (CW) radiofrequency excitation at frequency f_{RF}, emit radiofrequency induced second harmonic acoustic waves (RISHA) at double the frequency of the excitation radiofrequency wave[20, 22, 34], i.e. $2 \times f_{RF}$. RISHA waves $p(r,\omega)$ at angular frequency ω and detected at position r result from the absorption of RF energy by the conductive material. Ignoring the thermal conduction term, RISHA wave can be described using the thermoacoustic wave equation in the frequency domain, assuming an RF E-field source[20]:

$$\left[\nabla^2 + \left(\frac{\omega}{c_s}\right)^2\right]\tilde{p}(r,\omega) = \frac{-i\omega\beta}{C_p}\sigma(r)|\tilde{E}(r,\omega_0)|^2.$$ (18)

where $\sigma(\vec{r})$ is the spatial distribution of electrical conductivity of the medium imaged; $\tilde{E}(\vec{r},\omega_0)$ is the spectral electric field amplitude in the medium. Assuming the applied electric field has an angular frequency $\omega_0 = 2\pi f_{RF}$, i.e. $E(r,t) = e_r E_0 \cos(\omega_0 t) = e_r E_0 \cos(2\pi f_{RF} t)$, the RF power distribution in the Fourier domain can be then calculated as:

$$|\tilde{E}(r,\omega_0)|^2 = \frac{\pi}{2}E_0^2[\delta(\omega - 2\omega_0) + \delta(\omega + 2\omega_0) + 2\delta(\omega)].$$ (19)

Substituting *Eq. (19)* into *Eq. (18)* and solving for the $\tilde{p}(r,\omega)$ yields a second harmonic acoustic pressure wave with a frequency resonating at two times the E-field frequency $\omega = 2\omega_0$, i.e. $f_{RISHA} = 2 \times f_{RF}$. It has been shown[20, 22, 34] that conductive

materials absorbing RF energy with $f_{RF} = 3.2$ MHz generate RISHA waves at $f_{RISHA} = 2 \times f_{RF} = 6.4$ MHz, based on the thermoacoustic effect (**Figure 1**).
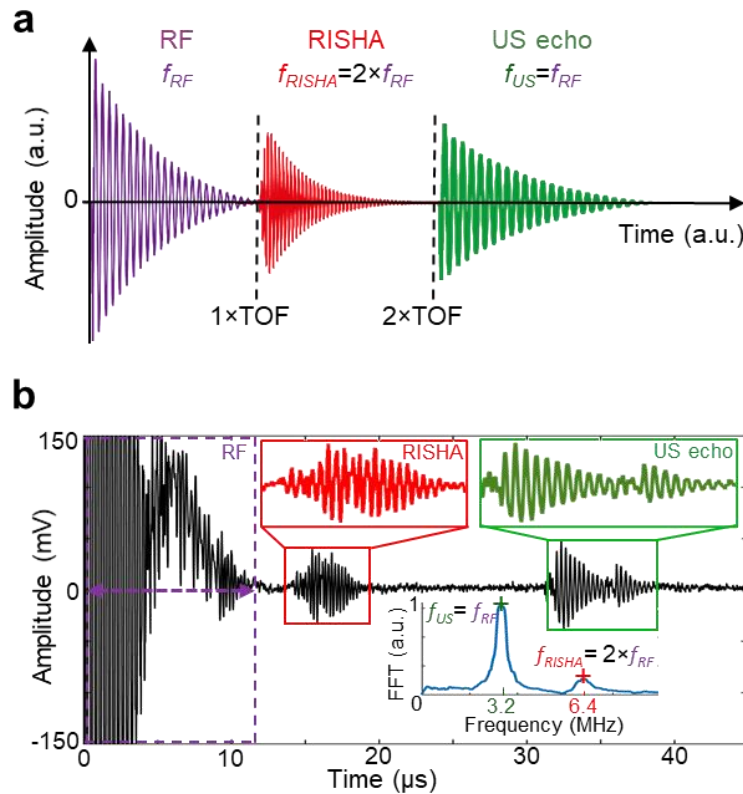
Figure 1 | Radiofrequency induced second harmonic acoustic signals (RISHA). (**a**) Illustration of second harmonic generation. (**b**) Experimentally measured signals. The ultrasound echo is a result of electromagnetic interference coupled to the transducer causing ultrasound emission due to inverse-piezoelectric effect. Reprinted with permission from ref [22] (Copyright © 2018 The Authors).

Second harmonic acoustic wave generation in thermoacoustics is universal to all EM radiation excitation and not limited to the RF spectrum. While here we show second harmonic acoustic waves only at RF frequencies, this phenomenon is also occurring at higher frequencies, such as in the GHz and THz band, however detection of GHz and THz acoustic waves is technically challenging due to the unavailability of acoustic detectors in this frequency band and the strong acoustic attenuation. At a relatively low frequency in the RF range, RISHA is interesting because 1) the second harmonic acoustic wave is within the detection bandwidth of our transducers, 2) the acoustic attenuation is moderate as acoustic attenuation increases as an exponential function of frequency [35], and 3) low frequency RF penetrates deeper in tissue [36].

Second harmonic generation predicted a way to improve SNR in thermoacoustic imaging. Because of the lack of high-peak power RF generator like a maser / laser, thermoacoustic excitation is a limited peak power problem [3, 37]. Utilizing the second

harmonic generation principle, one can use high sensitivity detection techniques like lock-in amplifier [38], and chirping radar [33].

1.3 RF absorption mechanisms

To deposit energy [via heating function $H(r, t)$] in sample to generate thermoacoustic wave, the energy must be absorbed and converted to internal thermal energy of material, i.e., converted into the form of the kinetic energy of randomly moving individual particles. Many different mechanisms can cause such thermal energy deposition, manifesting the versatile contrasts of thermoacoustic imaging. One exotic example is ionoacoustics. Accelerated charged particles, such as the protons that are used in proton tumor therapy in the clinics, can cause temperature rise at the Bragg peak where the most particles are deposited and the kinetic energy (tens to a few hundred MeV) is converted into thermal energy as well as other high-energy electromagnetic radiation like prompt gamma emission [7, 8, 38]. In the broad electromagnetic spectrum, the interactions with matters [39-41] vary from 1) the ionization even atomic activation of high energy photons (γ-rays, X-rays, ultraviolet), 2) to the electron transitions of outer shell of atoms in the visible and near infrared range, 3) to the molecular vibrations in the infrared / terahertz (THz) range, and 4) to the molecular rotation and torsion of polar molecules in the microwave range [28]. Among all the interactions, parts of the energy absorbed are converted to the thermal agitation of atoms and molecules (via friction of molecules, internal conversion of electron state, inter-system crossing and the following non-radiative relaxation, and etc.) and eventually become the source of thermoacoustic wave [11].

Radio frequencies deposit energy through three major mechanisms: 1) the Joule heating due to electrical conductivity, 2) the dielectric heating due to electric dipole relaxation, and 3) the hysteresis losses due to magnetic dipole relaxation. This is described by the following according to Poynting's theorem [26]:

$$P_{loss} = \sigma(r)|E(r,t)|^2 + \frac{\varepsilon''(r)}{2}|E(r,t)|^2 + \frac{\mu''(r)}{2}|H(r,t)|^2. \tag{20}$$

Here P_{loss} is the energy loss density; $\varepsilon''(r)$ is the imaginary part of the complex electric permittivity; $\mu''(r)$ is the imaginary part of the complex magnetic permeability; $E(r, t)$ the electric field amplitude (V/m) in the medium; and $H(r, t)$ is the magnetizing field amplitude (A/m). Because its permeability has negligible imaginary part, biological samples are considered nonmagnetic. Therefore, the magnetic field induced loss is usually ignored, unless ferromagnetic or ferrimagnetic materials are administered on purpose, such as in magnetoacoustics [4].

In microwave (>1 GHz) induced thermoacoustics, both electrical conductivity and permittivity play important roles in the heating function. There are both experimental data [42-44] and theoretical analysis [21] showing the coexisting of two heating mechanisms in microwave induced thermoacoustics. It is sometimes beneficial to image the water content in biological bodies using microwave excitation [5, 6, 17, 45, 46],

and experiment have shown dipole molecules respond differently in microwave induced thermoacoustics [18]. But to quantitatively image either the electrical conductivity or the permittivity is still a challenge due to the mixed contrast, and due to the influence of ubiquitous water content in tissue.

Differently, In the range of MHz to a few hundred megahertz, the major part of RF energy is absorbed via Joule heating [26, 28, 47, 48] in tissue which is determined by the current density, $J(\boldsymbol{r}, \boldsymbol{t})$, which is determined by the electrical conductivity:

$$H(\boldsymbol{r}, t) = \boldsymbol{J}(r, t) \cdot \boldsymbol{E}(r, t) = \sigma(\boldsymbol{r})\boldsymbol{E}(r, t) \cdot \boldsymbol{E}(r, t) = \sigma(\boldsymbol{r})|\boldsymbol{E}(r, t)|^2. \quad (21)$$

Table 2. Tissue conductivity at 3 MHz.

Tissue type	σ (S/m) at 3 MHz
DI water	5.50×10^{-6}
Copper	5.96×10^{7}
NaCl 0.9%	1.54
Blood	0.98
Muscle	0.57
Fat	0.026
Bile	1.4
Gallbladder	0.9
Cerebrospinal fluid	2.0
Intervertebral disc	0.83

At macroscopic level, many tissues, such as blood and muscle, exhibit high electrical conductivity compared to skin, fat, or bones [42-44, 49], as shown in *Table 2*. Many diseases cause imbalances in the cellular distributions of these ions, and thus changes in local conductivities [50]; examples include allergic diseases [51], cancer [52, 53], diabetes mellitus [54], cardiovascular diseases [55], neuronal dysfunctions [56], and renal abnormalities [57].

At microscopic level, distributions of electrical conductivity in cells depend on the concentrations and mobilities of critical charged species [31], such as proteins, nucleic acids, sodium, potassium, and calcium. As shown in *Figure 2* when exposed to an electric field that is stronger than the Johnson noise-equivalent field strength, a charged ion is accelerated along or against the electric field lines depending on the charge types. The added kinetic energy of the ion dissipates as heat due to collisions with other particles in the medium, causing a temperature rise and the subsequent thermal expansion, thus eventually emanating the thermoacoustic waves. According

to the classic view as Drude model of electrical conduction in solid [29-31], the electrical conductivity can be derived as:

$$\sigma = \frac{n(qe)^2\tau}{m_{ion}},\tag{22}$$

where q, e, n, m_{ion}, and τ are respectively the number of charges, electron charge, number density of the ions, mass of the ion specie, and the mean free time between ionic collisions.
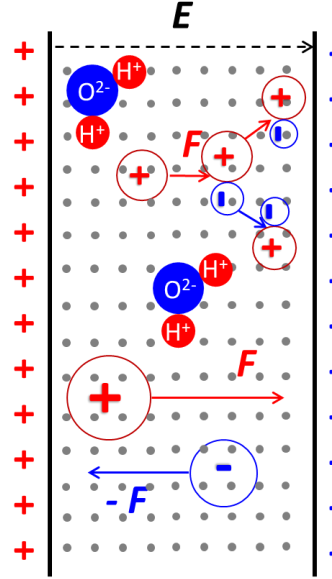
Figure 2 | Schematic of the free ions in electric field. For free ions, the electric field applies force and accelerates the particles to gain kinetic energy. If the field strength is large enough, Townsend discharging may happen.

Substituting *Eq. (22)* into *Eq. (21)* the heating function now becomes:

$$H(\boldsymbol{r},t) = \left[\frac{n(qe)^2\tau}{m_{ion}}\right]|\boldsymbol{E}(\boldsymbol{r},t)|^2.\tag{23}$$

The microscopic source of the radiofrequency induced thermoacoustic signal makes the imaging contrast very interesting. The charge-to-mass ratio of ions may indicate a signal measurement similar to mass spectrometry. This may represent one of the future goals of low-MHz radiofrequency induced thermoacoustic imaging / sensing, to resolve the concentration of specific types of ions of same charge-to-mass ratio.

The above heating function also indicates induced nonlinearity in the case of an excessive electric field strength, larger than the breakdown voltage of a given dielectric like water (65–70 MV/m). In such case Townsend discharging could happen causing avalanche multiplication in carriers' number due to the collision of accelerated ions / electrons, which may not be visible to human eyes yet during dark discharging [58] stage. Such effect is also illustrated in *Figure 2*:

$$n = n_0 e^{\alpha(|\boldsymbol{E}|)\cdot x},\tag{24}$$

where, n_0 is the intrinsic carrier number density, and x is the path length of accelerated charge carriers, and α is the multiplication coefficient of Townsend at unit distance.
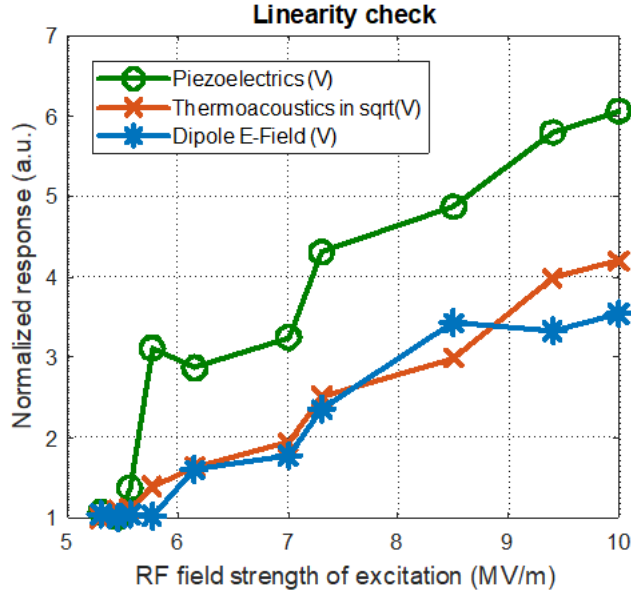
Figure 3 | Linearity check. The piezoelectric effect is known to be linear to some extent (with hysteresis) to the applied E-field strength, as well as the pick-up E-field by dipole antenna that was placed next to transmission line coupler used in ref [23]. But the thermoacoustic effect is linear to the field strength squared. Therefore, in order to put all the data in one graph and compare, the thermoacoustics curve is a square root of original voltage data.

In other words, before the electric field reach to the point that such breakdown happens, the thermoacoustic effect is linear to the square of E-field strength, and the electrical conductivity of sample. Our experiments shown in **Figure 3** confirmed the linearity of thermoacoustic generation to excitation field strength, and also the linearity to conductivity in publication [22, 59]. For highly conductive matters like metal, however, the electric field between conductors of transmission line is effectively increased by reducing the dielectric gap due to equipotential in metal, and thus breakdown could happen causing nonlinear responses. Such electric breakdown induced nonlinearity was not observed in biological tissues in our experiments.

1.4 Theoretical resolution limit

The lateral imaging resolution ($d_{lateral}$) of RF induced thermoacoustic imaging is limited by the acoustic diffraction limit [22], which is defined by the thermoacoustic wavelength (λ_{TA}) and by the *f*-number of the ultrasound transducer, which is *F/D*:

$$d_{lateral} = \lambda_{TA} \cdot \left(\frac{F}{D}\right) = \left(\frac{v_s}{f_{TA}}\right) \cdot \left(\frac{F}{D}\right) = \left(\frac{c_s}{2 \times f_{RF}}\right) \cdot \left(\frac{F}{D}\right) \tag{25}$$

With the presence of coupling medium for RF energy and acoustic wave, the frequency of RF excitation relates to RF wavelength λ_{RF} as follows:

$$f_{RF} = \frac{c_0/\sqrt{\varepsilon_r \mu_r}}{\lambda_{RF}} \tag{26}$$

in which c_0 is the speed of electromagnetic waves in a vacuum (3×10^8 m/s); ε_r is relative permittivity of the medium; and μ_r is relative permeability. Therefore, the lateral resolution of thermoacoustic imaging can be derived as:

$$d_{lateral} = \lambda_{RF} \cdot \left(\frac{c_s}{2 \times c_0/\sqrt{\varepsilon_r \mu_r}} \cdot \frac{F}{D} \right) \tag{27}$$

This says that the achievable imaging resolution of RISHA appears to be a fixed fraction of the excitation RF wavelength employed for a given ultrasound transducer. For example at 3.2 MHz RF excitation the lateral resolution is $1/(2.2 \times 10^4)$ of the RF wavelength (λ_{RF} = 10.5 meters) given *f*-number of two. The axial resolution is similarly determined by the fixed wavelengths ratio of acoustics and RF, and can be calculated using $0.80 \times \lambda_{TA}$ according to Wang *et al.*[60] and Omar *et al.*[24].

It is to be noted that the above analysis only applies when SHG is involved. For pulse modulated excitation (such as microwave and laser induced thermoacoustics) where the intrinsic frequency of the excitation energy cannot be detected and therefore ignored, the resolution limits are analyzed as in refs [24, 60].

1.5 Motivations of RF thermoacoustic imaging

The following sections provide the rationale and literature reviews for the two main topics: contrast (*chapter 2*) and resolution (*chapter 3*).

1.5.1 Intrinsic biological contrast

Conventional pulsed thermoacoustic imaging at 434 MHz has been proposed for early detection of breast cancer [5], while higher excitation frequencies at several GHz have been used to image different biological tissues based on their dielectric losses[46, 61-64]. These microwave-based thermoacoustic imaging methods provide good soft tissue contrast and contrast could be further enhanced by administering contrast agents[62, 65]. Nevertheless, shortcomings include low energy coupling due to far field radiation[66], and poor imaging resolution >1 mm due to the long excitation pulses typically employed (pulse modulation >500 ns).

To image electrical conductivity only (excluding permittivity), we chose excitation frequencies below 300 MHz. In this range, dielectric absorption by polar molecules is minimal [21, 59], as shown by both theory [42] and experiment [22, 59]. For example, the dielectric-to-conductivity absorption ratio is about 1% at frequencies between 13.67-36.34 MHz (<5% up to 300 MHz), corresponding to our readily available ultrasound detection bandwidth of according to the SHG principle [22]. We have confirmed the linear relation between electrical conductivity and thermoacoustic responses at low-

frequencies (low compared to the picosecond relaxation time of polar molecules [67]) using blood [22] and NaCl aqueous solutions [22, 59]. It is thus exciting to show predominantly the contrast from conductivity, especially for tissues with a high ionic content, like blood, body fluids, cerebellum fluids, grey matter in the brain, retinas, corneas, and the aqueous humor in the eye [42].

Among all the contrast candidates in biological body with high electrical conductivity [42-44, 49], blood was found by accident as the first tissue type to be imaged. Nonetheless, vascular imaging plays a central role in the assessment of blood vessels and can be used to diagnose diseases related to abnormal blood flow[68-70]. Different contrast mechanisms have been explored for non-invasive portable imaging of tissue vasculature. While existing methods exploit different properties of blood to visualize vasculature, the underlying contrast mechanism inherently limits the application of these methods in vascular imaging. Ultrasonography exploits differences in the reflection of ultrasound waves between vascular structures and surrounding tissue, allowing the visualization of large blood vessels as hypoechoic regions[71, 72]. Such a method can also identify vessel functionality by detecting Doppler shifts in emitted ultrasonic frequencies because of blood flow[72-74]. Optoacoustic imaging[74, 75], based on the strong optical absorption by hemoglobin, also allows visualization of vessels, typically over a larger diameter span than conventional ultrasonography[76, 77]. Optical coherence tomography[78] has also been considered for imaging fine vasculature, based on variations of reflected light due to blood flow, but it is suited for visualizing only superficial vessels at depths of about 400 microns. In contrast to using mechanical waves or optical energy, higher-energy photons do not provide adequate contrast for blood vessels. Consequently, X-ray computed tomography[79, 80] requires the use of iodine-based contrast agents. Similarly, magnetic resonance angiography[81] requires gadolinium-based contrast agents for vasculature imaging.

Near-field radiofrequency induced thermoacoustic imaging with possible novel contrast could serve as a new, agent-free contrast mechanism for non-invasive blood vessel imaging. First of all, near-field excitation allows efficient non-radiative excitation of ultrasound waves using RF energy to tissue, as opposed to the afore-mentioned microwave systems [5], whereby a large part of the radiated electromagnetic energy is reflected and/or dissipated in space but not in tissue. Therefore, a sensitive thermoacoustic vasculature imaging, exploiting the SHG principle, could offer an alternative to other blood vessel imaging methods by using inexpensive and readily available components that can lead to a low-cost and highly portable sensor. Promising applications of portable RISHA imaging could be general detection of sub-dermal blood vessels for catheter insertion, or inexpensive, disseminated measurements of vasculature, for example in characterizing loss in response to anti-tumor therapies, providing a sensitive and non-invasive tool for assessing changes in blood conductivity[82]. Conductivity sensing could be more generally helpful in assessing bulk ionic content in body fluids, such as urine (1.75 S/m), where ion levels are an important marker of renal abnormalities[57, 83],

offering diagnostic ability in bladder and kidney diseases. Other tissues could also be imaged using RISHA non-invasively aiding to disease diagnosis, including bile (1.4 S/m at 3 MHz), gallbladder (0.9 S/m), cerebrospinal fluid (2.00 S/m), and intervertebral disc (0.83 S/m), to name a few[84-86].

1.5.2 Microscopic imaging resolution

The direct, non-invasive observation of electrical conductivity in a biological system with microscale resolution was an unmet technical challenge. But according to our analysis in the theoretical imaging resolution (*section 1.4*), it may be possible to bring the resolution of radiofrequency induced thermoacoustic imaging into the micrometer range by using higher frequencies of acoustic detection (10-300 MHz), and the corresponding radiofrequency excitation (5-150 MHz) based on the SHG principle. While conductivity absorption remains as the dominant contrast [87], Such high resolution / frequency imaging technique may allow label-free visualization of subcellular ion concentrations, analogous to what has been accomplished with optical / optoacoustic imaging[76], making thermoacoustic imaging an intriguing experimental tool for label-free cellular studies of ion transport and related processes. For example, it may be possible to directly observe changes in ionic content of living cells in response to RF stimuli[88]. The ability to analyze electro-cellular[89, 90] and electro-thermo-cellular interactions may allow thermoacoustics to enrich the bioengineering toolbox with a new, non-invasive electric field method analogous to optics[91], patch-clamp[92], or magnetics based techniques[29, 30, 93].

At microscopic level, distributions of electrical conductivity in cells depend on the concentrations and mobilities of critical charged species [31], such as proteins, nucleic acids, sodium, potassium, and calcium. Many diseases cause imbalances in the cellular distributions of these ions, and thus changes in local conductivities [50]; examples include allergic diseases [51], cancer [52, 53], diabetes mellitus [54], cardiovascular diseases [55], neuronal dysfunctions [56], and renal abnormalities [57]. Therefore, since the invention of the patch-clamp techniques [94] by Sakmann and Neher in 1976, and the earlier, and the voltage-clamp technique [95] by Hodgkin and Huxley in 1952, there have been an explosion of studies elucidating the role of conductivity in tissue physiology, in addition to the electrical behaviors of single ion channel up to a whole cellular network in the nervous system. Patch-clamp is an electrode-based technique that can record electrical signals of isolated cells or tissues [96], but is limited to single-point measurements requiring elaborate skill in order to bring the electrode to close proximity to cellular membranes. Similarly, high-resolution, but superficial, topological conductivity mapping was achieved using micro/nano-pipette based scanning ion-conductance microscopy [97] and cantilever based conductive atomic force microscopy [98]. The evolution of electrical impedance tomography [99], using surface electrodes, enables non-invasive measurements of *in vivo* conductivity changes with high temporal resolution but suffers from poor spatial resolution of centimeters due to the multi-path nature of electric currents. Moreover, whole brain imaging methods like magnetoencephalography or magnetocardiography using

advanced quantum sensing can detect minuscule magnetic fields induced by the small current changes of for example action potentials in neurons but offer poor spatial resolution and require bulky cryogen cooled superconducting quantum interference device [100].

To image electrical signals with high resolution, there have been notable developments in the field of optical imaging using fluorescence dyes or genetically engineered proteins that are sensitive to voltage [101] or transient flux of ions [102]. These methods are based on electrochromic compounds that reversibly change color by voltage controlled electrochemical oxidation and reduction [101], or Förster resonance energy transfer (FRET) based chromophores that couple electronic excitation states of proximate molecules via nonradiative dipole-dipole interactions [101]. These techniques have revealed for example, the receptive map of mouse whiskers [103], the clock and olfactory neurons in model animals [104], <10 ms temporal resolution recordings of single action potential using optical electrophysiology techniques [105], and the possible neurophysiological foundation of gamma rhythm in diseases like autism and schizophrenia [106]. However, fluorescence techniques require invasive measurements to deliver the dyes to the location or require genetic modifications of organisms. Moreover, access to the tissue imaged may also require invasive methods that give access to the depth-limited microscopy method. Recent studies also showed that terahertz (also mid-infrared) spectroscopy can be used to indicate label-free membrane potential change based on vibrational spectra [107], but similarly require invasive procedures due to the very superficial nature of operation, typically reaching depths of only tens of microns to a few hundred microns. Micrometer-range resolution of conductivity in tissue has also shown possible using quantum sensing (optical resonance to electric or magnetic field changes) that exploits a crystal defect's spin state, such as nitrogen-vacancy in diamond [108] to sense the electrical signals from physiological process. However, such electron spin manipulation when used non-invasively to tissue requires close proximity to the site of the activity [109] and thus have often been conducted in *in vitro* studies. The imaging depth is also limited by the readout fluorescence light.

Long wavelength EM radiation, such as micro- and radio waves, penetrates deep into dielectric materials. Microwave (10^{-3}-1 m, 300-0.3 GHz) imaging provides label-free contrast of the complex electrical conductivity / permittivity of tissue due to dielectric heating and wave reflection of the tissue to the incident irradiation, and has been demonstrated for breast cancer imaging [110]. The diffraction-limited resolution of microwave imaging is proportional to wavelength (typically >1 millimeter), while axial resolution was reported to achieve super-resolution of 10 μm [111]. Electrical conductivity measurements can be also inferred from the water self-diffusion tensor, determined by diffusion tensor magnetic resonance imaging (MRI), at resolutions of a few millimeters [112]. However, besides offering indirect measurements of conductivity, MRI requires expensive instrumentation not typically available in the

biological laboratory and further improving the resolution would require excessively strong magnetic fields not readily available.

It is exciting to see how the microscopic contrast look like in the eyes of radio frequencies. Previous microwave induced thermoacoustic imaging techniques visualize both the electrical conductivity and permittivity [18], while lower-frequency RF is less sensitive to the polar molecules like water because the employed frequency (300 MHz) is too low to induce measurable dielectric heating via electric dipole relaxation [67]. Radiofrequency induced thermoacoustic microscopy might offer a new perspective for observing life phenomena by a direct observation on the ionic content in tissue that is playing as both the regulator and indicator in critical physiological processes [51, 54, 56, 57]. Several implementations of thermoacoustic imaging have been used for breast cancer imaging [5] at 434Mhz at 1.5 mm resolution, using long RF pulses (>1 µs width), utilizing mixed contrast from free ions and polarized molecules in tissue [21]. Resolution >300 micrometers has been also achieved at microwave frequencies 1.2-6 GHz (λ = 25-5 cm) [45]. Compared to microwave and millimeter wave excitation, low-frequency RF penetrates deeper into tissue [36] because attenuation (energy drops to $1/e^2$) is much lower at low frequencies than at high frequencies (14.3 cm penetration into muscle at 27.12 MHz vs 1.7 cm at 2.45 GHz). Previous thermoacoustic systems that employed similar near-field energy coupling and short RF pulses have only demonstrated in copper wire phantom resolutions [21] of up to 40 µm, or separation [113] up to 105 µm. Similarly, magnetic field mediated thermoacoustic imaging has demonstrated a 185 µm separation between aluminum sheets [114]. Using a magnetic field to induce eddy currents in conductive matter could potentially provide a similar resolution for conductivity imaging at greater penetration depths than other thermoacoustic methods [115, 116]. Microwave based thermoacoustic systems that employed amplitude modulation [5] have demonstrated resolutions of about 300 µm, but the resolution was limited by modulation width and irrespective of the radiation wavelength. The improved resolution of electrical conductivity map of small tissues increases the relevance of thermoacoustic imaging for biological applications. However, current far-field RF coupling cannot afford high SNR detection of tissue conductivity at high resolution. Using efficient near-field coupling can enable in turn the use of ultra-short radiofrequency pulses (10-100 ns) for broadband ultrasound excitation [21], which give rise to broadband ultrasound waves and high-resolution imaging.

Here the hypothesis is that 1.5 ns RF pulse excitation coupled with an open transmission line would afford orders of magnitude better resolution than allowed by the meters-long-wavelength of the RF pulse itself and allow conductivity imaging with the resolutions in the few tens of micrometers range. To examine this postulation, I have developed a novel raster-scanning radio-frequency thermoacoustic mesoscope (RThAM) and imaged using it copper and suture phantoms to demonstrate the resolution gains. I believe, beyond biological imaging, high-resolution RThAM may find applications in characterization of semiconductor

doping profiles [117]. However, further research would be required to establish precise knowledge on the contrast mechanisms, for example, the microscopic electrical conductivity distribution in small organisms.

1.6 Experimental setups

Details in methodology and materials are in the publications in the Appendix [22, 23].

1.6.1 Sensitive macroscopic imaging
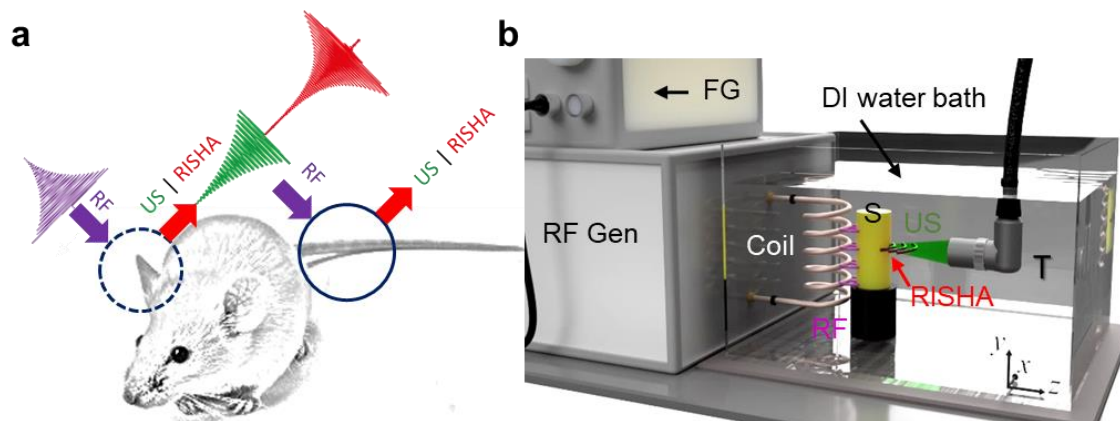
Figure 4 | Schematics and setup of near-field radiofrequency induced second harmonic (RISHA) thermoacoustic imaging. (**a**) RISHA imaging purpose is to resolve intrinsic contrast of blood in mice in vivo, and demonstrate the dual-mode RISHA/US imaging. (**b**) Schematic of RISHA set-up. A function generator (FG) triggers a radiofrequency generator (RF Gen) to produce RF-field bursts. A coil couples RF energy to the samples (S) within its near-field. The induced RISHA waves are detected by an ultrasound transducer (T). The transducer also transmits ultrasound (US) waves due to electromagnetic coupling of the RF field. The coil, sample and transducer are immersed in de-ionized (DI) water. Translational stages (not shown) scan the transducer in the *xy* plane. Reprinted with permission from publication #1 [22] (Copyright © 2018 The Authors).

The dual-mode RISHA/US imaging system [22] (**Figure 4**) is driven by a custom-built quasi-continuous wave RF-field generator containing a resistor-capacitor (RC) discharging circuit and a custom-built helical coil for near-field energy coupling. The helical coil is wound with 3 mm diameter copper wire and shielded with heat shrink tubing (TF31-9/3, HellermannTyton) with dielectric strength of 37 kV/mm. The quality factor of the RF-field generator is 20, allowing the set-up to provide narrowband stimulation of 5% FWHM bandwidth (0.16 MHz) at a central frequency of 3.2 MHz. A function generator (33210A, Agilent Technologies) controls the repetition rate of the quasi-continuous RF bursts (1-50 Hz, max 765 mJ per pulse). We performed raster scanning with a spherically focused transducer (V311, Olympus-NDT; central frequency, 10 MHz; focus, 25.4 mm) mounted on *xy*-translation stages (LTA-HS, ESP 300 controller, Newport Corp) that move across the

sample in 100-μm steps in the *xy* plane, corresponding to 1/5th of the diffraction limit of the 6.4 MHz RISHA wave. The coil, sample, and transducer are immersed in a de-ionized water bath to provide efficient US and RF coupling. To remove low frequency oscillation, we used a high-pass RC filter with cutoff frequency at 300 kHz to filter the signal detected by transducer. In our experiments, a 51-dB amplifier (AU-1332, MITEQ) amplified the signals in copper wire experiments, while a 63-dB amplifier (AU-1291, MITEQ) amplified the signals in experiments with biological tissues. The amplified signals were digitized by a digital oscilloscope (TDS3054B, Tektronix). The digitized data were averaged 16 or 32 times and stored on a personal computer, which was also used for synchronizing the raster scanning and for reconstructing the images. In our *in vivo* mice measurements, we used 16 times averaged signals, with 50 Hz burst repetition rate. Given 0.1 second of data transmission and stage scan for each point, the total imaging time for a 10 mm × 10 mm field of view is ~70 minutes. We simulated using the k-Wave Matlab toolbox [118] the acoustic interference in a tube with a diameter of 3 mm and wall thickness of 0.1 mm according to the experiments.

1.6.2 Thermoacoustic microscopy

The thermoacoustic microscope [23] is shown in ***Figure 5***. An RF pulser (FPG 10-10NK1, FID GmbH) generates 5-10 kV pulses of 1.5 ns at $1\text{-}10^4$ Hz pulse repetition rate (PRR) using drift step recovery diode. We used a flexible 50-Ω coaxial cable (RG213/U, Pasternack) to deliver the energy. To prevent system damage in case of impedance mismatching, we inserted a custom-built 1.5 dB T-pad passive attenuator of 50 Ω impedance before feeding the RF pulse into the energy coupling element. The energy coupling element is an open transmission line (TxLine) by design. Custom-built 50 Ω termination is consisted of 4-by-4 RF power resistors (CHF3725CNP, Bourns). To optimize the electric field strength in the TxLine, we used light silicone oil (PSF-2CSt Silicone Fluid, Clearco Products; specific gravity 873 kg/m^3; speed of sound 931 m/s) as dielectric, which exhibits dielectric breakdown strength ≥14 kV/mm, viscosity 2 cSt at 25°C, and dielectric constant ε_r = 2.45. To maximize radiofrequency energy coupling, the open TxLine was built with 1-mm dielectric height and 3-mm conductor width from 0.3-mm thick copper sheet, to have a 50-Ω characteristic impedance matching to the pulse source and the termination load. The RF design was done using electromagnetic simulation (CST studio) and tested using vector network analyzer (E5061B, Agilent). As a result, a pulsed RF energy of 2.91 mJ was coupled through a cross-section of 1×3 mm^2 of TxLine. As shown in ***Figure 5a***, to prevent direct contact between the samples and TxLines, we firstly sprayed a thin layer of resin (Plastik 70, Kontakt Chemie) on the surface of the copper conductors, then placed a 20 μm thick polyethylene (PE) film between sample and copper conductors. Biological samples were supported by a PE tubing of 1-mm outer diameter. The sample and TxLine were immersed in silicone oil. We used a USB microscope (DigiMicro Profi, DNT) to help with sample installation and positioning. To ensure good acoustic coupling, we used the above-mentioned PE film to contain de-ionized water (5.5×10^{-6} S/m) so as to couple RThAM/ultrasound waves in the detection path of the transducer. We assume

Figure 5 | Schematics and setup of radiofrequency induced thermoacoustic microscope (RThAM). (**a**) Schematic of RThAM principle. (**b**) EM simulation (CST studio) showing the E-field distribution at 300 MHz in TxLine and egg-like sample. (**c**) Diagram of RThAM setup. Radiofrequency (RF) pulser generates 5-10 kV, 1.5 ns pulses which are coupled via coaxial cable to the sample in between open TxLine. The generated RThAM waves (dashed red arcs) are coupled by de-ionized water (DI H_2O) to a spherically focused ultrasound transducer. The RThAM signal is amplified by a 63-dB amplifier and digitized by a data acquisition card (DAQ) in a personal computer (PC). The DAQ is triggered by either the RF pulser or function generator used in active ultrasound imaging. The PC synchronizes the setup, scans the stages to perform raster scan in xy plane, stores and reconstructs the images. The custom-built bypass circuit is inserted to allow for ultrasonography using function generator exciting US emission in transducer. Reprinted with permission from publication #2 [23] (Copyright © 2021 The Authors).

that the de-ionized water and tubing above/in the open TxLine, and the applied resin and contact-avoiding film do not change substantially the electric field in the TxLine. Within the de-ionized water bag, we placed a spherically focused piezoelectric transducer (V3330, Olympus-NDT; central frequency 50 MHz, 90.66% bandwidth, focus 6 mm, diameter 6.35 mm). To enable raster scan in three-dimensional space, we mounted the transducer to xy translation stages (M-683.2U4 and M-404.2PD, Physik Instrumente) and mounted the imaging chamber containing the open TxLine, dielectrics, and samples to a z stage (M-404.2PD). The scanning step is 5-25 μm in general. We used a 63 dB amplifier (AU-1291, MITEQ) to amplify signals detected by the ultrasound transducer, and a data acquisition card (CompuScope 12502-128M, Gage-Applied; sampling rate 500 MS/s; 1024 hardware averages) to digitize the signals. Digitized data were stored in a personal computer, which was also used for synchronizing raster scanning and reconstructing the images in Matlab. A typical raster scan in RThAM mode takes 20 minutes for a FOV of 1.5×1.5 mm^2 using 10 μm steps.

We have also designed an open TxLine of 25 Ω characteristic impedance for characterization experiments using the copper wire samples. Biological tissues, due to their low conductivity (typically a few S/m) and low RThAM signal generation using our chosen RF pulser, require silicone oil and water bag to couple the RThAM signals, but copper generates high thermoacoustic [21] signals due to its high conductivity σ = 5.8×10^7 S/m. So, in the attempt to use water as dielectric we used a de-ionized water filled open TxLine to couple the RF energy and the ultrasound/RThAM waves. The 25-Ω open TxLine is constructed with copper sheet as conductor with dielectric gap of 6 mm and conductor width of 3.5 mm. The TxLine is matched to the 50 Ohm source, by inserting before it a 25 Ω resistor in series and terminating it with a 25 Ω load. This 6-mm gap open TxLine uses water as a dielectric medium and has more operational space for sample handling, but it delivers 72 times less energy flux than the 1-mm oil gap TxLine used for this work, and 1069 times less RF intensity (difference between RF energy attenuation of pure water and pure oil, 30.29 dB) due to the polarization field of water molecule, and therefore is not suitable for biological tissue experiments.

1.7 Summary and outlook

1.7.1 Summary

Thermoacoustic imaging is demonstrated with unique intrinsic contrast in model animals like mice macroscopically and in zebrafish at microscopic level. Using the presented engineering practice, it is possible to harness radio frequency energy for biological and medical applications such as recording bulk body fluids of high conductivity that is deep inside body, and visualize conductivity changes of cells due to developments or disease related physiological change.

I have presented a new label-free, non-invasive method to image conductivity paths within dielectric materials, including animal tissues. RF induced second harmonic acoustic responses allow for blood vessel imaging without the need to administer contrast agents. Imaging experiments *in vivo* and *ex vivo* showed that the second harmonic response of blood, i.e., the blood conductivity, is independent of its oxygenation state. Our technique excites samples with RF in the high frequency band (3–30 MHz), and provides a final image resolution 2.2×10^4 times smaller than the excitation wavelength of 10.5 meters. The use of near-field narrowband energy coupling maximizes thermoacoustic response and minimizes energy loss. thermoacoustic imaging requires only inexpensive, widely available RF hardware as well as widely available US detection hardware, enabling simultaneously US pulse-echo imaging of the sample without additional hardware. Such a technique could be used not only for biomedical imaging, but also for imaging the interior of industrial products, such as integrated circuits, revealing both the conductive paths and morphology of the circuits.

Towards thermoacoustic microscopy, ultrashort RF pulses and an open transmission line for near-field energy coupling is demonstrated to record higher-resolution images of conductive materials versus previous thermoacoustic systems. We challenged the limits of this system by imaging zebrafish eggs and larvae and observed correlations between microscale biological structures with high expected ionic content and thermoacoustic contrast. These are the highest-resolution thermoacoustic images of biological samples to date.

1.7.2 Outlook

The demonstrated imaging depth, contrast and resolution of thermoacoustics is encouraging a promise of new inspection scanner in clinics on daily basis, and could potentially motivate applications, for which direct electrical conductivity readouts could be of use, like angiogenesis of tumors for early-stage detection, ablation monitoring of cancerous tissue, diagnosis of renal abnormalities diagnosis and neuronal dysfunctions, as well as semiconductor doping profiling or printed circuit board inspection. It has seen many scientific explorations emanating: such as the developments of novel technologies [119-123], nanotechnology [124-126], ionoacoustics [127, 128], optoacoustic sensors [11, 129-132], the imaging of arthritis in finger joints [17, 133, 134], hemorrhage [135], osteoporosis [136], tumors [137], tumor therapy [59, 125-128, 138], and beyond biomedical applications [121, 122, 139, 140] such as multiphase flow imaging [140].

In order to push thermoacoustic imaging towards clinical usage and daily biomedical laboratory usage, further developments in instrumentation are required. Simple optimizations can improve the resolution and sensitivity, using for example, optimized RF-field excitation and higher frequencies meeting the thermal and stress confinements. Also with advanced RF coupling designs, water is feasible as the dielectric in transmission line (coplanar strip lines were implemented in the lab) and enables more *in-vivo* biological observations. The signal and image quality could potentially be improved by introducing detection and signal processing techniques

that were developed for optoacoustic mesoscopy [24], such as matched filtering, and using an RF excitation source that matches the frequency range to the detection bandwidth (e.g. 10 ns pulser for RThAM 100 MHz). Because thermoacoustic imaging is usually based on inhomogeneous RF excitation in the reactive near-field of coupling elements[66, 141], future applications on thick samples larger than a mouse may require RF field strength correction[66, 142].

Currently RF pulser of high peak power like laser is still a challenge thus limiting SNR. To overcome the peak power limitation, it is likely that chirping technique as in chirping radar can be used in thermoacoustic excitation using existing waveform generator and RF power amplifier as source [37]. And the energy coupling element can be simply transmission line to deliver the ultrawide-band RF pulses (feasible up to a few GHz). But a long chirp of RF excitation may cause severe EM interference coupled to transducers via fringe fields. Therefore, one may want to confine the chirp to a time and frequency window exploiting the SHG of thermoacoustics to denoise, or better to use interference-immune optical sensing techniques for thermoacoustic detection, such as those open beam methods like laser Doppler vibrometer, Fabry-Perot cavity, or Bragg grating based fiber solutions [143]. It is also possible to adopt encoded-phasic RF excitation. Currently I have only used unbalanced negative pulsing for macroscopic imaging, and only monophasic pulses for microscopic imaging. This translates to the energy transduction from RF field energy to kinetic energy gain from linear acceleration. But in biological samples there may not be long enough path for free ions to accelerate to maximum velocity. In such case it may be possible to use coded amplitude of pulse waveform to effectively increase the acceleration path of free ions. For example, one can encode the pulsing structure to make free ions go in round trip as harmonic oscillation in one dimensional. For spherical objects like cells, one may boost the thermoacoustic signal by using an external static magnetic field to cause circular acceleration of free ions in sample via Lorentz force [115].

There are possibilities to achieve both high-SNR and high molecular specificity in tissue by using contrast agents. Molecular imaging is of crucial importance in modern diagnostics in biological research and clinics [129, 131, 144]. But thermoacoustic imaging is still limited by lack of contrast agents in the low-RF region[59, 65]. The development of contrast agent for low frequency RF absorption is challenging and requires detailed understanding of the contrast mechanism in this frequency band[65, 145]. It has been demonstrated that high salinity nanodroplet containing hypertonic saline can boost up thermoacoustic signal strength and target to prostate cancer in xenograft mouse model [146]. Other methods also include semiconductor nanoparticles, carbon based nanotubes or quantum dots, hyperbolic nanoparticles that consist of alternative dielectric-metal surfaces, and plasmon effect in radio regime by tuning the resonant absorption and Young's modulus to enable resonant acoustic vibrations [124].

There are still research questions in cellular reactions to the applied RF fields. At protein levels, mechanistic research is needed to explain the cellular reactions. RF induced thermoacoustic generation relies on ultra-high field strength. While pushing

for higher excitation field and thus higher thermoacoustic SNR, I would certainly recommend research in cell viability assessment, safety field strength for excitable cells like muscle cells and neurons to avoid direct activation of the ion channels on cellular membrane via depolarization or electroporation. When changing pulsing to chirping excitation, even though direct activation by high RF fields may be avoided, chirping excitation may pose thermal hazards to sample. To study further the microscopic mechanisms of RF-tissue interaction, an image splitter and a fluorescent microscope can be incorporated to the thermoacoustic microscopic to analyze the FRET effect due to electrostatic force via fluorescence readout. It may even be possible to switch fluorescence by RF fields via magneto-optical Faraday effect to add versatility of RF thermoacoustics to the bioengineering toolbox [129, 131].

Radio frequencies due to deep penetration can be used to actively stimulate brain for neuromodulation. Brain stimulation and inhibition is observed caused by RF excitation in the dual-modal thermoacoustic / fluorescence microscope. On the other side of potential adverse events, many lay efforts to use RF waves for therapeutic applications. RF based deep brain stimulations (DBS) exploit direct interactions between low frequency RF and the human brain and include electrical excitation using surface-based or implanted electrodes that offer neuromodulation. DBS can correct abnormal rhythms (tremor) caused in Parkinson's disease [147], dystonia, obsessive compulsive disorder, and epilepsy [40,41]. H-coil based magnetic field stimulation operating according to Faraday's law of electromagnetic induction can offer a non-invasive approach to neuromodulation, but it has not yet been approved for clinical use. Some electric stimulations were reported to cause neuroplasticity as well as neuron apoptosis [147-149]. In preclinical studies non-invasive DBS was achieved based on the principle of transcranial alternating current stimulation (tACS), which can invoke neuronal activity with some spatial certainty[49] using surface electrodes [88] [150]. One of the technical challenges in using RF fields for neuromodulation is the lack of space resolution. But it has been shown that using temporal interference [88] or synthetic antenna array, it is possible to achieve spatial selectivity in deep brain stimulation.

It will be extremely exciting if one could see the possible advancements and bring them into reality by harnessing radiofrequency fields for the multi-dimensional purposes in biomedicine.

2. Blood vessel imaging using radiofrequency-induced second harmonic acoustic response

2.1 Summary

In order to investigate the intrinsic tissue contrast of RF induced thermoacoustic imaging, I developed sensing modalities and investigated whether RF fields with wavelengths exceeding ten meters can enable imaging of small conductivities changes in mice *in vivo*. Exploiting the second harmonic generation of thermoacoustic waves, for the first time, we discovered that RF energy can be used for high-resolution label-free blood vessel visualization based on the difference in electrical conductivity between blood and surrounding tissues. I further examined the dependence of blood RISHA response on oxygenation state and demonstrate the implicit ability of the new modality to produce RF-induced passive ultrasound images. This method demonstrated 6-dB blood-to-muscle contrast, high dynamic range of conductivity detection, and the ability to perform simultaneous RF-induced passive ultrasound imaging using inexpensive instrumentation. We demonstrated the ability to image at depths of up to 2.5 cm in muscle using RISHA imaging. Future system optimizations can improve the resolution and sensitivity using optimized RF-field excitation and higher frequencies. RISHA imaging could be employed in various biomedical applications non-invasively assessing vasculature, overall tissue electrical conductivity, and also for functional imaging like characterization of the relationship between blood oxygenation and conductivity as well as thermoacoustic Doppler flowmetry of blood flow.

I contributed equally with Dr. Stephan Kellnberger, the supervisor of this project. I accidently discovered the thermoacoustic contrast of blood in muscle tissue using an Aldi chicken thigh, and therefore determined to investigate the contrast mechanism. I rebuilt, based on an existing pulser, the high-voltage radiofrequency pulser to achieve voltage output at -30 kV with minimum harmonic distortions. To perform imaging experiments, I assembled the dedicated imaging set-up, designed the image reconstruction algorithms, and performed all the experiments. I performed the acoustic simulation using k-Wave. I prepared the figures, wrote the first manuscripts in which the results were discussed, and the writing was edited and revised with help from Dr. Stephan Kellnberger, Prof. Dr. George Sergiadis and Prof. Dr. Vasilis Ntziachristos. I wrote the response to peer reviews, revised our manuscript with help from Dr. Stephan Kellnberger on editing, and performed the required experiments.

2.2 Publication 1

The data presented is an original work published in Scientific Reports in October 2018 and reprinted under a Creative Commons Attribution License 4.0 (CC BY).

Blood vessel imaging using radiofrequency-induced second harmonic acoustic response. Yuanhui Huang, Stephan Kellnberger, George Sergiadis, Vasilis Ntziachristos. Scientific Reports **8**, 15522 (2018). DOI: 10.1038/s41598-018-33732-0. Copyright © 2018 The Authors.

3. Noninvasive visualization of electrical conductivity in tissues at the micrometer scale

3.1 Summary

Studying the microscopic contrast mechanism of thermoacoustic imaging requires microscopy, which was technically challenging and unmet in using meters-long radio waves to reveal a microscopic view of tissue ionic content. In this work, I explored further the concept of near-field excitation combined with optoacoustic mesoscopy using high-bandwidth US detection. The efficient near-field coupling enables, in turn, the use of ultrashort RF pulses (10 to 100 ns) for broadband US excitation, which give rise to broadband US waves and high-resolution imaging. The detection of ultrasound rather than radio waves enables micrometer-scale resolutions, over several millimeters of tissue depth. The hypothesis was that 1.5-ns RF pulse excitation coupled with an open transmission line would afford orders of magnitude better resolution than allowed by the meters-long wavelength of the RF pulse itself and allow conductivity imaging with resolutions in the range of a few tens of micrometers. To examine this postulation, I developed a novel raster-scanning radio-frequency thermoacoustic mesoscopy (RThAM) arrangement and imaged copper and suture phantoms to demonstrate the resolution gains. We confirmed an imaging resolution of <30 μm in phantoms. To examine whether *in vivo* imaging could be performed, we also visualized the free ionic content distribution in small zebrafish embryos of ~1 mm in diameter, revealing rich details of the electrical conductivity based on tomographic images. We further demonstrate the quantitative potential of RThAM in imaging conductivity changes during zebrafish embryonic development and in zebrafish larvae (1- and 512-cell stages *in vivo*), revealing complex spatial patterns in vivo. Our study demonstrated the high axial and lateral imaging resolution of conductivity in tissues achievable using RThAM, which could be more generally used for noninvasive, label-free investigations that are complementary to electrode- or fluorescence-based methods.

I designed and implemented this study. I built the first prototype of RThAM with Dr. Murad Omar using discontinuity in microstrip transmission line, in which we achieved imaging of copper wire but not biological tissues. With the supervision of Prof. Dr. George Sergiadis, I built and experimented multiple versions of the transmission lines and finally achieved sufficient radiofrequency excitation to tissue using the reported open transmission line. I led the research, built the dedicated imaging setup, implemented the image reconstruction algorithms, performed the experiments, and processed and analyzed the data. Dr. Weili Tian, Dr. Hernán Lopez-Schier, and Prof. Dr. Gil Gregor Westmeyer provided the biological samples and

support in biological experiments. I designed all the figures, wrote the first manuscripts, response letter to peer reviews, and edited the writing with the help from writing scientists Dr. Robert Wilson and Dr. Chapin Rodriguez. All authors participated in the discussion and analysis of results and manuscript writing.

3.2 Publication 2

The data presented is an original work published in Science Advances in May 2021 and reprinted under a Creative Commons Attribution License 4.0 (CC BY).

Noninvasive visualization of electrical conductivity in tissues at the micrometer scale. Yuanhui Huang, Murad Omar, Weili Tian, Hernán Lopez-Schier, Gil Gregor Westmeyer, Andriy Chmyrov, George Sergiadis, Vasilis Ntziachristos. Science Advances **7**-20, eabd1505 (2021). DOI: 10.1126/sciadv.abd1505. Copyright © 2021 The Authors.

Bibliography

1. Bowen, T. Radiation-Induced Thermoacoustic Soft Tissue Imaging. *1981 Ultrasonics Symposium*, 817-822 (1981).
2. Bowen, T., Nasoni, R.L., Pifer, A.E. & Sembroski, G.H. in 1981 Ultrasonics Symposium 823-827 (1981).
3. Razansky, D., Kellnberger, S. & Ntziachristos, V. Near-field radiofrequency thermoacoustic tomography with impulse excitation. *Med. Phys.* **37**, 4602-4607 (2010).
4. Kellnberger, S. et al. Magnetoacoustic Sensing of Magnetic Nanoparticles. *Phys. Rev. Lett.* **116**, 108103 (2016).
5. Kruger, R.A. et al. Breast cancer in vivo: contrast enhancement with thermoacoustic CT at 434 MHz-feasibility study. *Radiology* **216**, 279-283 (2000).
6. Ku, G. & Wang, L.V. Scanning thermoacoustic tomography in biological tissue. *Med. Phys.* **27**, 1195-1202 (2000).
7. Assmann, W. et al. Ionoacoustic characterization of the proton Bragg peak with submillimeter accuracy. *Med. Phys.* **42**, 567-574 (2015).
8. Sulak, L. et al. Experimental studies of the acoustic signature of proton beams traversing fluid media. *Nuclear Instruments and Methods* **161**, 203-217 (1979).
9. Jones, K.C. et al. Experimental observation of acoustic emissions generated by a pulsed proton beam from a hospital‐based clinical cyclotron. *Med. Phys.* **42**, 7090-7097 (2015).
10. Ntziachristos, V., Ripoll, J., Wang, L.V. & Weissleder, R. Looking and listening to light: the evolution of whole-body photonic imaging. *Nat. Biotechnol.* **23**, 313-320 (2005).
11. Fuenzalida Werner, J.P. et al. Challenging a Preconception: Optoacoustic Spectrum Differs from the Optical Absorption Spectrum of Proteins and Dyes for Molecular Imaging. *Anal. Chem.* **92**, 10717-10724 (2020).
12. Bell, A.G. The Production of Sound by Radiant Energy. *Science* **2**, 242-253 (1881).
13. Rosencwaig, A. Photoacoustic spectroscopy of biological materials. *Science* **181**, 657-658 (1973).
14. Wang, L.V. Photoacoustic imaging and spectroscopy. (CRC press, 2009).
15. Patel, C.K.N. & Tam, A.C. Pulsed optoacoustic spectroscopy of condensed matter. *Rev. Mod. Phys.* **53**, 517-550 (1981).
16. Gordon, J.P., Zeiger, H.J. & Townes, C.H. The Maser---New Type of Microwave Amplifier, Frequency Standard, and Spectrometer. *Phys. Rev.* **99**, 1264-1274 (1955).
17. Chi, Z. et al. First assessment of thermoacoustic tomography for in vivo detection of rheumatoid arthritis in the finger joints. *Med. Phys.* **n/a** (2021).
18. Luo, W., Ji, Z., Yang, S. & Xing, D. Microwave-Pumped Electric-Dipole Resonance Absorption for Noninvasive Functional Imaging. *Phys. Rev. Appl.* **10**, 024044 (2018).
19. Kellnberger, S., Hajiaboli, A., Razansky, D. & Ntziachristos, V. Near-field thermoacoustic tomography of small animals. *Phys. Med. Biol.* **56**, 3433-3444 (2011).
20. Kellnberger, S., Omar, M., Sergiadis, G. & Ntziachristos, V. Second harmonic acoustic responses induced in matter by quasi continuous radiofrequency fields. *Appl. Phys. Lett.* **103**, 153706 (2013).
21. Omar, M., Kellnberger, S., Sergiadis, G., Razansky, D. & Ntziachristos, V. Near-field thermoacoustic imaging with transmission line pulsers. *Med. Phys.* **39**, 4460-4466 (2012).
22. Huang, Y., Kellnberger, S., Sergiadis, G. & Ntziachristos, V. Blood vessel imaging using radiofrequency-induced second harmonic acoustic response. *Sci. Rep.* **8**, 15522 (2018).

23.   Huang, Y. et al. Noninvasive visualization of electrical conductivity in tissues at the micrometer scale. *Science Advances* **7**, eabd1505 (2021).

24.   Omar, M., Aguirre, J. & Ntziachristos, V. Optoacoustic mesoscopy for biomedicine. *Nat. Biomed.* **3**, 354-370 (2019).

25.   Wang, L.V. & Wu, H.-i. Biomedical optics: principles and imaging. (John Wiley & Sons, 2012).

26.   Omar, M.A. in Chair for Biological Imaging, Vol. Ph.D. 152 (Technical University of Munich, Munich, Germany; 2015).

27.   Rosenthal, A., Razansky, D. & Ntziachristos, V. Fast semi-analytical model-based acoustic inversion for quantitative optoacoustic tomography. *IEEE Trans. Med. Imaging* **29**, 1275-1285 (2010).

28.   Kellnberger, S. in Chair for Biological Imaging, Vol. Ph.D. 188 (Technical University of Munich, Munich, Germany; 2012).

29.   Drude, P. Zur elektronentheorie der metalle; II. Teil. galvanomagnetische und thermomagnetische effecte. *Ann. Phys. (Berl.)* **308**, 369-402 (1900).

30.   Drude, P. Zur elektronentheorie der metalle; I. Teil. *Ann. Phys. (Berl.)* **306**, 566-613 (1900).

31.   Dressel, M. & Scheffler, M. Verifying the Drude response. *Ann. Phys. (Berl.)* **15**, 535-544 (2006).

32.   Franz, R. & Wiedemann, G. Ueber die Wärme-Leitungsfähigkeit der Metalle. *Ann. Phys. (Berl.)* **165**, 497-531 (1853).

33.   Telenkov, S., Mandelis, A., Lashkari, B. & Forcht, M. Frequency-domain photothermoacoustics: Alternative imaging modality of biological tissues. *J. Appl. Phys.* **105**, 102029 (2009).

34.   Kellnberger, S. et al. Magnetoacoustic Sensing of Magnetic Nanoparticles. *Phys. Rev. Lett.* **116**, 108103 (2016).

35.   Chen, W. & Holm, S. Modified Szabo's wave equation models for lossy media obeying frequency power law. *The Journal of the Acoustical Society of America* **114**, 2570-2574 (2003).

36.   Johnson, C.C. & Guy, A.W. Nonionizing electromagnetic wave effects in biological materials and systems. *Proc. IEEE* **60**, 692-718 (1972).

37.   Nan, H. & Arbabian, A. Peak-power-limited frequency-domain microwave-induced thermoacoustic imaging for handheld diagnostic and screening tools. *IEEE Trans. Microw. Theory Tech.* **65**, 2607-2616 (2017).

38.   Wieser, H.-P. et al. Experimental demonstration of accurate Bragg Peak localization with ionoacoustic Tandem Phase Detection (iTPD). *Physics in Medicine and Biology* (2021).

39.   Griffiths, D.J. Introduction to electrodynamics. (Prentice Hall, 1962).

40.   Feymann, R., Leighton, R.B. & Sands, M. The Feynman Lectures on Physics. (Addison-Wesley, Reading, Massachusetts, 1965).

41.   Balanis, C.A. Advanced engineering electromagnetics. (John Wiley & Sons, 2012).

42.   Gabriel, S., Lau, R.W. & Gabriel, C. The dielectric properties of biological tissues: III. Parametric models for the dielectric spectrum of tissues. *Phys. Med. Biol.* **41**, 2271-2293 (1996).

43.   Gabriel, S., Lau, R.W. & Gabriel, C. The dielectric properties of biological tissues: II. Measurements in the frequency range 10 Hz to 20 GHz. *Phys. Med. Biol.* **41**, 2251-2269 (1996).

44.   Gabriel, C., Gabriel, S. & Corthout, E. The dielectric properties of biological tissues: I. Literature survey. *Phys. Med. Biol.* **41**, 2231-2249 (1996).

45. Nie, L., Xing, D., Zhou, Q., Yang, D. & Guo, H. Microwave-induced thermoacoustic scanning CT for high-contrast and noninvasive breast cancer imaging. *Med. Phys.* **35**, 4026-4032 (2008).

46. Ku, G. & Wang, L.V. Scanning microwave-induced thermoacoustic tomography: signal, resolution, and contrast. *Med. Phys.* **28**, 4-10 (2001).

47. Patch, S.K. et al. Thermoacoustic contrast of prostate cancer due to heating by very high frequency irradiation. *Phys. Med. Biol.* **60**, 689-708 (2015).

48. Emerson, J.F. et al. Electromagnetic acoustic imaging. *IEEE Trans Ultrason Ferroelectr Freq Control* **60**, 364-372 (2013).

49. Hasgall, P. et al., Vol. Version 4.0, Edn. May 15, 2018 (2018).

50. Grasland-Mongrain, P. & Lafon, C. Review on Biomedical Techniques for Imaging Electrical Impedance. *IRBM* **39**, 243-250 (2018).

51. Matthias, J. et al. Sodium chloride is an ionic checkpoint for human TH2 cells and shapes the atopic skin microenvironment. *Sci. Transl. Med.* **11**, eaau0683 (2019).

52. Haemmerich, D. et al. In vivo electrical conductivity of hepatic tumours. *Physiol. Meas.* **24**, 251-260 (2003).

53. Schepkin, V.D. et al. In vivo magnetic resonance imaging of sodium and diffusion in rat glioma at 21.1 T. *Magn. Reson. Med.* **67**, 1159-1166 (2012).

54. Gordon, D.M. & Ash, S.R. Lack of correlation of glucose levels in filtered blood plasma to density and conductivity measurements. *ASAIO J.* **55**, 227-230 (2009).

55. Schaefer, M., Gross, W., Ackemann, J. & Gebhard, M.M. The complex dielectric spectrum of heart tissue during ischemia. *Bioelectrochemistry* **58**, 171-180 (2002).

56. Jentsch, T.J., Hubner, C.A. & Fuhrmann, J.C. Ion channels: function unravelled by dysfunction. *Nat. Cell Biol.* **6**, 1039-1047 (2004).

57. Manoni, F. et al. Laboratory diagnosis of renal failure: urine conductivity and tubular function. *Minerva Urol. Nefrol.* **61**, 17-20 (2009).

58. Xiao, D. in Gas Discharge and Gas Insulation. (ed. D. Xiao) 47-88 (Springer Berlin Heidelberg, Berlin, Heidelberg; 2016).

59. Tamarov, K. et al. Electrolytic conductivity-related radiofrequency heating of aqueous suspensions of nanoparticles for biomedicine. *Phys. Chem. Chem. Phys.* **19**, 11510-11517 (2017).

60. Xu, M.H. & Wang, L.H.V. Photoacoustic imaging in biomedicine. *Rev. Sci. Instrum.* **77**, 041101 (2006).

61. Aliroteh, M.S. & Arbabian, A. Microwave-Induced Thermoacoustic Imaging of Subcutaneous Vasculature With Near-Field RF Excitation. *IEEE Trans. Microw. Theory Tech.* **66**, 577-588 (2018).

62. Alireza, M., John H., B. & Susan C., H. Toward contrast-enhanced microwave-induced thermoacoustic imaging of breast cancer: An experimental study of the effects of microbubbles on simple thermoacoustic targets. *Phys. Med. Biol.* **54**, 641–650 (2009).

63. Nie, L., Xing, D., Zhou, Q., Yang, D. & Guo, H. Microwave-induced thermoacoustic scanning CT for high-contrast and noninvasive breast cancer imaging. *Medical physics* **35**, 4026-4032 (2008).

64. Zheng, Z., Huang, L. & Jiang, H. Label-free thermoacoustic imaging of human blood vessels in vivo. *Appl. Phys. Lett.* **113**, 253702 (2018).

65. Ogunlade, O. & Beard, P. Exogenous contrast agents for thermoacoustic imaging: an investigation into the underlying sources of contrast. *Med. Phys.* **42**, 170-180 (2015).

66. Razansky, D., Kellnberger, S. & Ntziachristos, V. Near-field radiofrequency thermoacoustic tomography with impulse excitation. *Medical physics* **37**, 4602-4607 (2010).

67. Buchner, R., Barthel, J. & Stauber, J. The dielectric relaxation of water between 0 C and 35 C. *Chem. Phys. Lett.* **306**, 57-63 (1999).
68. Omar, M., Schwarz, M., Soliman, D., Symvoulidis, P. & Ntziachristos, V. Pushing the optical imaging limits of cancer with multi-frequency-band raster-scan optoacoustic mesoscopy (RSOM). *Neoplasia* **17**, 208-214 (2015).
69. Dronkers, C.E., Klok, F.A. & Huisman, M.V. Current and future perspectives in imaging of venous thromboembolism. *J Thromb Haemost* **14**, 1696-1710 (2016).
70. Carmeliet, P. & Jain, R.K. Angiogenesis in cancer and other diseases. *Nature* **407**, 249-257 (2000).
71. Pandian, N.G. et al. Ultrasound angioscopy: real-time, two-dimensional, intraluminal ultrasound imaging of blood vessels. *Am. J. Cardiol.* **62**, 493-494 (1988).
72. Errico, C. et al. Ultrafast ultrasound localization microscopy for deep super-resolution vascular imaging. *Nature* **527**, 499-502 (2015).
73. Camici, P.G., d'Amati, G. & Rimoldi, O. Coronary microvascular dysfunction: mechanisms and functional assessment. *Nat. Rev. Cardiol.* **12**, 48-62 (2015).
74. Taruttis, A. et al. Optoacoustic Imaging of Human Vasculature: Feasibility by Using a Handheld Probe. *Radiology* **281**, 256-263 (2016).
75. Taruttis, A. & Ntziachristos, V. Advances in real-time multispectral optoacoustic imaging and its applications. *Nat. Photonics* **9**, 219-227 (2015).
76. Omar, M., Soliman, D., Gateau, J. & Ntziachristos, V. Ultrawideband reflection-mode optoacoustic mesoscopy. *Opt. Lett.* **39**, 3911-3914 (2014).
77. Aguirre, J. et al. Precision assessment of label-free psoriasis biomarkers with ultra-broadband optoacoustic mesoscopy. *Nat. Biomed.* **1**, 0068 (2017).
78. Huang, D. et al. Optical coherence tomography. *Science* **254**, 1178-1181 (1991).
79. Treeby, B.E. & Cox, B.T. k-Wave: MATLAB toolbox for the simulation and reconstruction of photoacoustic wave fields. *J. Biomed. Opt.* **15**, 021314 (2010).
80. Chugh, B.P. et al. Measurement of cerebral blood volume in mouse brain regions using micro-computed tomography. *NeuroImage* **47**, 1312-1318 (2009).
81. Lentschig, M.G. et al. Breath-hold gadolinium-enhanced MR angiography of the major vessels at 1.0 T: dose-response findings and angiographic correlation. *Radiology* **208**, 353-357 (1998).
82. Abdalla, S., Al-Ameer, S.S. & Al-Magaishi, S.H. Electrical properties with relaxation through human blood. *Biomicrofluidics* **4**, 34101 (2010).
83. Wang, J.M. et al. Evaluating the performance of urine conductivity as screening for early stage chronic kidney disease. *Clin. Lab.* **60**, 635-643 (2014).
84. Gabriel, S., Lau, R.W. & Gabriel, C. The dielectric properties of biological tissues: III. Parametric models for the dielectric spectrum of tissues. *Phys Med Biol* **41**, 2271-2293 (1996).
85. Gabriel, S., Lau, R.W. & Gabriel, C. The dielectric properties of biological tissues: II. Measurements in the frequency range 10 Hz to 20 GHz. *Phys Med Biol* **41**, 2251-2269 (1996).
86. Hasgall, P. et al., Vol. Version 4.0, Edn. May 15, 2018 (2018).
87. Omar, M., Kellnberger, S., Sergiadis, G., Razansky, D. & Ntziachristos, V. Near-field thermoacoustic imaging with transmission line pulsers. *Medical physics* **39**, 4460-4466 (2012).
88. Grossman, N. et al. Noninvasive Deep Brain Stimulation via Temporally Interfering Electric Fields. *Cell* **169**, 1029-1041 e1016 (2017).
89. Bassett, C.A. & Pawluk, R.J. Electrical behavior of cartilage during loading. *Science* **178**, 982-983 (1972).

90. Shamos, M.H. & Lavine, L.S. Piezoelectricity as a Fundamental Property of Biological Tissues. *Nature* **213**, 267-269 (1967).

91. Boyden, E.S., Zhang, F., Bamberg, E., Nagel, G. & Deisseroth, K. Millisecond-timescale, genetically targeted optical control of neural activity. *Nat Neurosci* **8**, 1263-1268 (2005).

92. Mainen, Z.F. & Sejnowski, T.J. Reliability of spike timing in neocortical neurons. *Science* **268**, 1503-1506 (1995).

93. Munshi, R. et al. Magnetothermal genetic deep brain stimulation of motor behaviors in awake, freely moving mice. *Elife* **6**, e27069 (2017).

94. Neher, E. & Sakmann, B. Single-channel currents recorded from membrane of denervated frog muscle fibres. *Nature* **260**, 799-802 (1976).

95. Hodgkin, A.L. & Huxley, A.F. Propagation of electrical signals along giant nerve fibres. *Proc. Royal Soc. B* **140**, 177-183 (1952).

96. Abbott, J. et al. A nanoelectrode array for obtaining intracellular recordings from thousands of connected neurons. *Nat. Biomed.* **4**, 232-241 (2019).

97. Hansma, P.K., Drake, B., Marti, O., Gould, S.A. & Prater, C.B. The scanning ion-conductance microscope. *Science* **243**, 641 (1989).

98. Cui, X.D. et al. Reproducible Measurement of Single-Molecule Conductivity. *Science* **294**, 571 (2001).

99. Bayford, R.H. Bioimpedance tomography (electrical impedance tomography). *Annu. Rev. Biomed. Eng.* **8**, 63-91 (2006).

100. Boto, E. et al. Moving magnetoencephalography towards real-world applications with a wearable system. *Nature* **555**, 657-661 (2018).

101. Vogt, N. Voltage sensors: challenging, but with potential. *Nat. Methods* **12**, 921-924 (2015).

102. Boyden, E.S., Zhang, F., Bamberg, E., Nagel, G. & Deisseroth, K. Millisecond-timescale, genetically targeted optical control of neural activity. *Nat. Neurosci.* **8**, 1263-1268 (2005).

103. Akemann, W., Mutoh, H., Perron, A., Rossier, J. & Knöpfel, T. Imaging brain electric signals with genetically targeted voltage-sensitive fluorescent proteins. *Nat. Methods* **7**, 643-649 (2010).

104. Cao, G. et al. Genetically targeted optical electrophysiology in intact neural circuits. *Cell* **154**, 904-913 (2013).

105. Gong, Y., Wagner, M.J., Zhong Li, J. & Schnitzer, M.J. Imaging neural spiking in brain tissue using FRET-opsin protein voltage sensors. *Nat. Commun.* **5**, 3674 (2014).

106. Sohal, V.S., Zhang, F., Yizhar, O. & Deisseroth, K. Parvalbumin neurons and gamma rhythms enhance cortical circuit performance. *Nature* **459**, 698-702 (2009).

107. Lee, H.J. et al. Label-Free Vibrational Spectroscopic Imaging of Neuronal Membrane Potential. *J. Phys. Chem. Lett.* **8**, 1932-1936 (2017).

108. Schirhagl, R., Chang, K., Loretz, M. & Degen, C.L. Nitrogen-vacancy centers in diamond: nanoscale sensors for physics and biology. *Annu. Rev. Phys. Chem.* **65**, 83-105 (2014).

109. Fu, C.-C. et al. Characterization and application of single fluorescent nanodiamonds as cellular biomarkers. *Proc. Natl. Acad. Sci. U.S.A.* **104**, 727 (2007).

110. Nikolova, N.K. Microwave Imaging for Breast Cancer. *IEEE Microw. Mag.* **12**, 78-94 (2011).

111. Wang, P., Li, Z., Liu, P. & Pei, Y. Super resolution in depth for microwave imaging. *Appl. Phys. Lett.* **115**, 044101 (2019).

112. Voigt, T., Katscher, U. & Doessel, O. Quantitative Conductivity and Permittivity Imaging of the Human Brain Using Electric Properties Tomography. *Magn. Reson. Med.* **66**, 456-466 (2011).

113.   Lou, C., Yang, S., Ji, Z., Chen, Q. & Xing, D. Ultrashort microwave-induced thermoacoustic imaging: a breakthrough in excitation efficiency and spatial resolution. *Phys. Rev. Lett.* **109**, 218101 (2012).

114.   Liu, S., Zhang, R., Luo, Y. & Zheng, Y. Magnetoacoustic microscopic imaging of conductive objects and nanoparticles distribution. *J. Appl. Phys.* **122**, 124502 (2017).

115.   Feng, X., Gao, F., Kishor, R. & Zheng, Y. Coexisting and mixing phenomena of thermoacoustic and magnetoacoustic waves in water. *Sci. Rep.* **5**, 11489 (2015).

116.   Feng, X.H., Gao, F. & Zheng, Y.J. Magnetically mediated thermoacoustic imaging toward deeper penetration. *Appl. Phys. Lett.* **103**, - (2013).

117.   Murrell, M.P. et al. Spatially resolved electrical measurements of SiO2 gate oxides using atomic force microscopy. *Appl. Phys. Lett.* **62**, 786-788 (1993).

118.   Treeby, B.E. & Cox, B.T. k-Wave: MATLAB toolbox for the simulation and reconstruction of photoacoustic wave fields. *J. Biomed. Opt.* **15**, 021314 (2010).

119.   Emerson, J.F., Chang, D.B., McNaughton, S., Emerson, E.M. & Cerwin, S.A. Electromagnetic acoustic imaging methods: resolution, signal-to-noise, and image contrast in phantoms. *Journal of Medical Imaging* **8**, 067001 (2021).

120.   Zhao, Y. et al. Microwave-excited hybrid thermoacoustic and ultrasound imaging with microwave pulse-width modulation. *AIP Advances* **9**, 015323 (2019).

121.   Scotti, G., Fan, S.-Y., Liao, C.-H. & Chiu, Y. Body-implantable RFID tags based on ormocer printed circuit board technology. *IEEE Sensors Letters* **4**, 1-4 (2020).

122.   del Angel-Arrieta, F., Morales-Pérez, C.J., de Jesus Rangel-Magdaleno, J. & Ramos-García, R. 1-6 (IEEE.

123.   Zheng, Z., Jiang, Y., Huang, L., Zhao, Y. & Jiang, H. An improved method for quantitative recovery of conductivity using tomographically measured thermoacoustic data. *Journal of X-ray science and technology* **28**, 137-145 (2020).

124.   Abraham-Ekeroth, R.M. & De Angelis, F. Radioplasmonics: Plasmonic Transducers in the Radiofrequency Regime for Resonant Thermo-acoustic Imaging in Deep Tissues. *ACS Photonics* **8**, 238-246 (2021).

125.   Gongalsky, M.B. et al. Radiofrequency stimulated and Silicic Acid Enhanced Hyperthermia Effectusing the Biodegradation of Porous Silicon Nanowires. (2019).

126.   Gongalsky, M. et al. Radiofrequency hyperthermia of cancer cells enhanced by silicic acid ions released during the biodegradation of porous silicon nanowires. *ACS omega* **4**, 10662-10669 (2019).

127.   Wieser, H.P. et al. Experimental demonstration of accurate Bragg peak localization with ionoacoustic tandem phase detection (iTPD). *Phys. Med. Biol.* **66**, 245020 (2021).

128.   Wieser, H.-P. et al. First Experimental Demonstration of accurate Bragg Peak Localization with ionoacoustic Tandem Phase Detection (iTPD). *Med. Phys.*, 2579-2674 (2020).

129.   Mishra, K. et al. Genetically encoded photo-switchable molecular sensors for optoacoustic and super-resolution imaging. *Nat. Biotechnol.* (2021).

130.   Liu, N. et al. Croconaine-based nanoparticles enable efficient optoacoustic imaging of murine brain tumors. *Photoacoustics* **22**, 100263 (2021).

131.   Mishra, K. et al. Multiplexed whole-animal imaging with reversibly switchable optoacoustic proteins. *Science Advances* **6**, eaaz6293 (2020).

132.   Fuenzalida Werner, J.P. et al. Structure-Based Mutagenesis of Phycobiliprotein smURFP for Optoacoustic Imaging. *ACS Chem. Biol.* **14**, 1896-1903 (2019).

133.   Chi, Z., Huang, L., Ge, S. & Jiang, H. Anti‐phase microwave illumination‐based thermoacoustic tomography of in vivo human finger joints. *Med. Phys.* **46**, 2363-2369 (2019).

134. Chi, Z., Huang, L., Zheng, Z., Zhao, Y. & Jiang, H. in IEEE International Conference on Computational Electromagnetics (ICCEM) 1-3 (IEEE, 2019).

135. Zhao, Y., Shan, T., Chi, Z. & Jiang, H. Thermoacoustic tomography of germinal matrix hemorrhage in neonatal mouse cerebrum. *Journal of X-ray science and technology* **28**, 83-93 (2020).

136. Chi, Z., Liang, X., Wang, X., Huang, L. & Jiang, H. Detection and Monitoring of Osteoporosis in a Rat Model by Thermoacoustic Tomography. *IEEE Journal of Electromagnetics, RF and Microwaves in Medicine and Biology* **4**, 234-239 (2020).

137. Rahpeima, R., Soltani, M. & Kashkooli, F.M. Numerical study of microwave induced thermoacoustic imaging for initial detection of cancer of breast on anatomically realistic breast phantom. *Computer Methods and Programs in Biomedicine* **196**, 105606 (2020).

138. Qin, H., Cui, Y., Wu, Z., Chen, Q. & Xing, D. Real-time thermoacoustic imaging-guidance for breast tumor resection. *IEEE Photonics Journal* **12**, 1-7 (2020).

139. Zhao, Y., Shan, T., Chi, Z., Huang, L. & Jiang, H. 1-5 (VDE.

140. Wang, S. et al. Digital Twin of Electrical Tomography for Quantitative Multiphase Flow Imaging. *arXiv preprint arXiv:2112.05792* (2021).

141. Nikitin, P.V., Rao, K.V.S. & Lazar, S. in 2007 IEEE International Conference on RFID 167-174 (2007).

142. Kellnberger, S., Hajiaboli, A., Razansky, D. & Ntziachristos, V. Near-field thermoacoustic tomography of small animals. *Phys Med Biol* **56**, 3433-3444 (2011).

143. Wissmeyer, G., Pleitez, M.A., Rosenthal, A. & Ntziachristos, V. Looking at sound: optoacoustics with all-optical ultrasound detection. *Light Sci. Appl.* **7**, 53 (2018).

144. Razansky, D. et al. Multispectral opto-acoustic tomography of deep-seated fluorescent proteins in vivo. *Nat. Photonics* **3**, 412-417 (2009).

145. Pramanik, M., Swierczewska, M., Green, D., Sitharaman, B. & Wang, L.V. Single-walled carbon nanotubes as a multimodal-thermoacoustic and photoacoustic-contrast agent. *J. Biomed. Opt.* **14**, 034018 (2009).

146. Chen, Y.-S. et al. Ultra-high-frequency radio-frequency acoustic molecular imaging with saline nanodroplets in living subjects. *Nature Nanotechnology* (2021).

147. Polanía, R., Nitsche, M.A. & Ruff, C.C. Studying and modifying brain function with non-invasive brain stimulation. *Nat. Neurosci.* **21**, 174-187 (2018).

148. Kalia, S.K., Sankar, T. & Lozano, A.M. Deep brain stimulation for Parkinson,s disease and other movement disorders. *Curr. Opin. Neurol.* **26**, 374-380 (2013).

149. Greenberg, B.D. et al. Deep brain stimulation of the ventral internal capsule/ventral striatum for obsessive-compulsive disorder: worldwide experience. *Mol. Psychiatry* **15**, 64-79 (2010).

150. Hutcheon, B. & Yarom, Y. Resonance, oscillation and the intrinsic frequency preferences of neurons. *Trends Neurosci.* **23**, 216-222 (2000).

Appendix – Publications 1 & 2

SCIENTIFIC REP⚙RTS

OPEN

Blood vessel imaging using radiofrequency-induced second harmonic acoustic response

Yuanhui Huang [1,2], Stephan Kellnberger[1,2,3], George Sergiadis[1,4,5] & Vasilis Ntziachristos[1,2]

We introduce a contrast mechanism for visualizing blood vessels based on radiofrequency-induced second harmonic acoustic (RISHA) signals sensing blood conductivity. We develop a novel imaging system using commonly available inexpensive components, and demonstrate *in vivo* RISHA visualization of blood vessels based on low-power quasi-continuous radiofrequency excitation of tissue at frequencies of a few MHz. We show how the novel approach also implicitly enables radiofrequency-induced passive ultrasound imaging and can be readily applied to non-invasive imaging of blood vessels *ex vivo* and *in vivo*. We discuss the implications of non-invasive conductivity measurements in the context of biomedical applications.

Vascular imaging plays a central role in the assessment of blood vessels and can be used to diagnose diseases related to abnormal blood flow[1–3]. Different contrast mechanisms have been explored for non-invasive portable imaging of tissue vasculature. While existing methods exploit different properties of blood to visualize vasculature, the underlying contrast mechanisms inherently limit the application of these methods in vascular imaging. Ultrasonography exploits differences in the reflection of ultrasound (US) waves between vascular structures and surrounding tissue, allowing the visualization of large blood vessels as hypoechoic regions[4,5]. Such a method can also identify vessel functionality by detecting Doppler shifts in emitted ultrasonic frequencies because of blood flow[5–7]. Optoacoustic imaging[7,8], based on the strong optical absorption by hemoglobin, also allows visualization of vessels, typically over a larger diameter span than conventional ultrasonography[9,10]. Optical coherence tomography[11] has also been considered for imaging fine vasculature, based on variations of reflected light due to blood flow, but it is suited for visualizing only superficial vessels at depths of about 400 microns. In contrast to using mechanical waves or optical energy, higher-energy photons do not provide adequate contrast for blood vessels. Consequently, X-ray computed tomography[12,13] requires the use of iodine-based contrast agents. Similarly, magnetic resonance angiography[14] requires gadolinium-based contrast agents for vasculature imaging.

In this work, we explore a new, agent-free contrast mechanism for non-invasive blood vessel imaging. We show for the first time that radiofrequency (RF) energy can be used for high-resolution label-free blood vessel visualization based on difference in electrical conductivity between blood and surrounding tissues. We explain the basis of radiofrequency-induced second harmonic acoustic (RISHA) generation and explain how quasi-continuous RF waves in the MHz range, delivered by energy coupling in the near-field, can be employed to visualize vasculature *in vivo* and *ex vivo*. We develop a RISHA sensing modality and investigate whether RF fields with wavelengths exceeding 10 meters can enable RISHA imaging of small vasculature in mice. We further examine the dependence of blood RISHA response on oxygenation state and demonstrate the implicit ability of the new modality to produce RF-induced passive ultrasound images.

[1]Helmholtz Zentrum München, Institute for Biological and Medical Imaging (IBMI), Neuherberg, D-85764, Germany. [2]Technische Universität München, Chair for Biological Imaging, München, D-81675, Germany. [3]Cardiovascular Research Center, Cardiology Division, Massachusetts General Hospital, Harvard Medical School, Boston, Massachusetts, 02114, USA. [4]Aristotle University of Thessaloniki, School of Electrical and Computer Engineering, Thessaloniki, 54124, Greece. [5]Chinese Academy of Sciences, Suzhou Institute of Biomedical Engineering and Technology, Suzhou, 215163, China. Yuanhui Huang and Stephan Kellnberger contributed equally. Correspondence and requests for materials should be addressed to S.K. (email: stephan.kellnberger@tum.de) or V.N. (email: v.ntziachristos@tum.de)

Results

Concept of the RISHA signal generation. We have recently[15,16] shown that electrically conductive materials exposed to continuous wave (CW) radiofrequency excitation at frequency f_{RF} emit ultrasonic (RISHA) waves at double the frequency of the excitation radiofrequency wave, i.e. $2 \times f_{RF}$. RISHA waves $p(\vec{r}, \omega)$ at angular frequency ω and detected at position $\vec{r}$ result from the absorption of RF energy by the conductive material. RISHA wave can be described using the thermoacoustic wave equation in the frequency domain, assuming an RF electric field (E-field) source[15]:

$$\left(\nabla^2 + \left(\frac{\omega}{v_s}\right)^2\right) p(\vec{r}, \omega) = \frac{-j\omega\beta}{C_p} \sigma(\vec{r}) \left|\hat{E}(\vec{r}, \omega_0)\right|^2$$

(1)

where ∇^2 denotes the spatial Laplacian operator, v_s is the acoustic speed in medium, β is the thermal expansion coefficient, C_p is the specific heat capacity, $\sigma(\vec{r})$ is the spatial distribution of electrical conductivity of the medium imaged, $\hat{E}(\vec{r}, \omega_0)$ is the spectral E-field amplitude in the medium, and $j = \sqrt{-1}$. Assuming the applied E-field has an angular frequency $\omega_0 = 2\pi f_{RF}$, i.e. $E(\vec{r}, t) = \vec{e_r} E_0 \cos(\omega_0 t) = \vec{e_r} E_0 \cos(2\pi f_{RF} t)$, the RF power distribution in the Fourier domain can be then calculated as:

$$\left|\hat{E}(\vec{r}, \omega)\right|^2 = \frac{\pi}{2} E_0^2 \vec{e_r} [\delta(\omega - 2\omega_0) + \delta(\omega + 2\omega_0) + 2\delta(\omega)]$$

(2)

Substituting Eq. (2) into Eq. (1) and solving for the RISHA wave $p(\vec{r}, \omega)$ yields a second harmonic acoustic pressure wave with a frequency resonating at two times the E-field frequency $\omega = 2\omega_0$, i.e. $f_{RISHA} = 2 \times f_{RF}$. For example, it has been shown[15,16] that conductive materials absorbing RF energy with $f_{RF} = 3.1$ MHz generate RISHA waves at $f_{RISHA} = 2 \times f_{RF} = 6.2$ MHz, based on the thermoacoustic effect.

Second harmonic acoustic wave generation in thermoacoustics is universal to all excitation frequencies and not limited to the RF spectrum. While we show second harmonic acoustic waves only at RF frequencies, this phenomenon is also occurring at higher frequencies in the GHz and THz band. However, the detection of GHz and THz acoustic waves is technically challenging due to the unavailability of acoustic detectors in this frequency band and the strong acoustic attenuation. Therefore, as a proof-of-concept study, we chose a relatively low frequency in the RF range for RISHA sensing, because (1) the second harmonic acoustic wave is within the detection bandwidth of our transducers, (2) the acoustic attenuation is moderate as acoustic attenuation increases as an exponential function of frequency, and (3) low frequency RF enables higher penetration depths in tissue.

RISHA imaging set-up. We hypothesized that near-field[15–19], narrowband RF excitation in the low-MHz range can generate RISHA responses from blood and that these responses can be detected and reconstructed into blood vessel images based on differences in electrical conductivity between blood and surrounding tissues. To test this hypothesis, we implemented a RISHA experimental setup consisting of a custom-built coil to couple RF energy to a sample in its near-field (Fig. 1a). In contrast to typical thermoacoustic imaging implementations[20], which irradiate the sample in the far-field[21,22] usually at GHz-range frequencies, near-field energy coupling enables optimal RF energy deposition even in the few-MHz range and minimizes the requirement for high-power pulsers[15–19,23]. Figure 1a shows diagrammatically the RISHA imaging set-up (see Methods), which comprises a custom-built 3.2 MHz RF generator emitting 12 µs RF-field bursts at a maximum energy of 765 mJ and repetition rate of 1–50 Hz, a homemade coil to couple energy to samples in its near-field, and a 10-MHz transducer (focus, 25.4 mm; central frequency, 10 MHz; f-number, 2) to capture RISHA responses. The coil, samples, and transducer are immersed in de-ionized water (electrical conductivity $< 5.5 \times 10^{-6}$ S/m) for optimal RF energy and RISHA wave coupling. The transducer is mounted on a xy stage for raster scans with 100-µm step size.

Figure 1b schematically describes the temporal signals involved in RISHA sensing. During an RF excitation, electromagnetic coupling of the RF field to the piezoelectric transducer causes transducer relaxation[15,17,18,24], which generates pulse/echo US signals approximately 60 dB weaker than the signal generated by a conventional pulser/receiver unit (Model 5077PR, Olympus-Panametrics, USA), as shown in Supplementary Text 1 and Fig. S1. To separate RISHA signal in temporal sequence from the transducer relaxation, we applied the quasi-CW excitation, instead of CW excitation, as the narrowband RF excitation (0.16 MHz bandwidth defined by full-width at half-maximum, FWHM). Likewise, quasi-CW excitation enables also the temporal separation of RISHA and echo US signal that is generated during transducer relaxation. The echo US signal is herein exploited for simultaneous ultrasonography imaging of hyperechoic target based on time-of-flight (TOF) measurements. For instance, by placing the transducer 18 mm away from the sample imaged, RISHA signals can be detected 12 µs after excitation, i.e. $1 \times$ TOF required to traverse the distance from sample to detector, as shown in Fig. 1b,c. As previously demonstrated[15,16], the RISHA signals oscillate at the second harmonic of the excitation radiofrequency: $f_{RISHA} = 2 \times f_{RF}$. At $2 \times$ TOF, the detector also records the pulse-echo US signal emitted during its RF-induced relaxation. This US signal exhibits a frequency $f_{US} = f_{RF}$. RISHA set-up using quasi-CW excitation enables co-registered dual-mode RISHA/US imaging based on the difference either in frequencies or TOFs measurement (see Methods for details of signal processing and image formation).

RISHA sensing: whole blood. Figure 1c shows the simultaneous RISHA and RF-induced US signals detected from a polyethylene tube containing mouse blood. The blood sample was excited by the quasi-CW RF-field bursts of fundamental frequency $f_{RF} = 3.2$ MHz, and the resulting RISHA waves were detected at the second harmonic of f_{RF}, i.e. $f_{RISHA} = 2 \times f_{RF} = 6.4$ MHz, occurring at a TOF of 15–20 µs after the start of the RF emission. At $2 \times$ TOF (30–40 µs) of the same sequence, ultrasound echoes of the tubing walls were detected. The
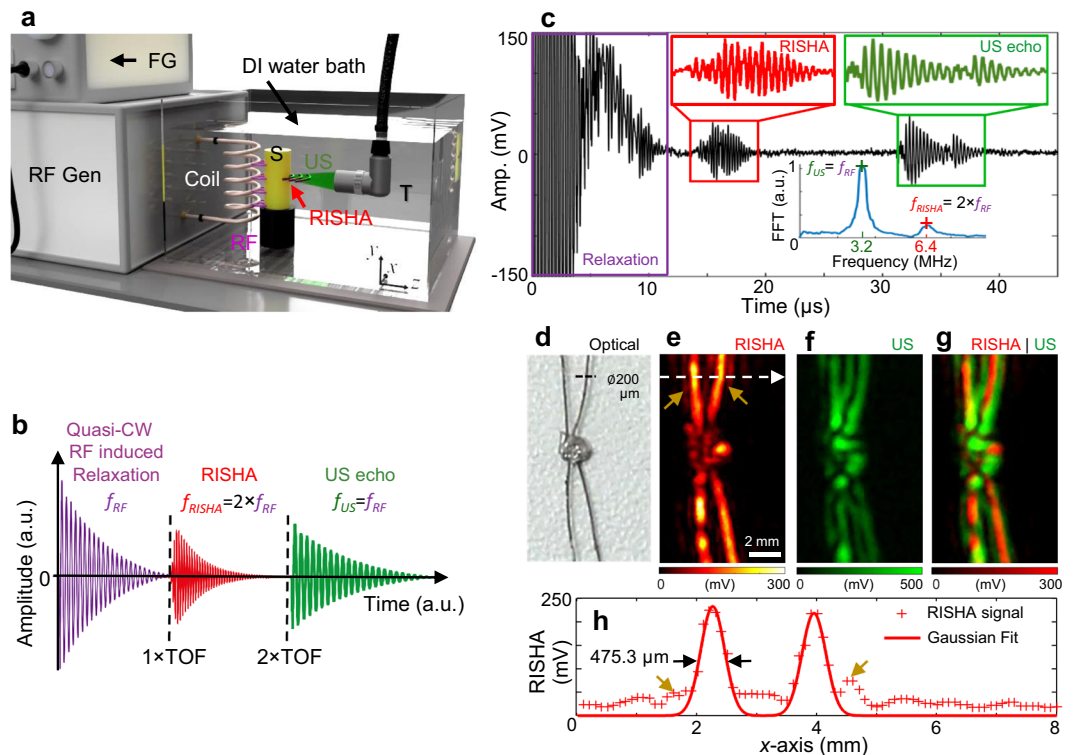
Figure 1. RISHA imaging set-up and tests on blood and copper wires. (**a**) Schematic of RISHA set-up. A function generator (FG) triggers a radiofrequency generator (RF Gen) to produce RF-field bursts. A coil couples RF energy to the samples (S) within its near-field. The induced RISHA waves are detected by an ultrasound transducer (T). The transducer also transmits ultrasound (US) waves due to electromagnetic coupling of the RF field. The coil, sample, and transducer are immersed in de-ionized (DI) water. Translational stages (not shown) scan the transducer in the xy plane. (**b**) Temporal signals involved in RISHA sensing. The transducer records at the beginning the relaxation signal during quasi-CW RF excitation induced by electromagnetic coupling (purple, frequency f_{RF}), and the US echoes (green, $f_{US} = f_{RF}$) at a time of flight of a roundtrip ($2 \times$ TOF). RISHA waves (red, $f_{RISHA} = 2 \times f_{RF}$) are detected at $1 \times$ TOF. (**c**) RISHA response of mouse blood in a polyethylene tube. The 0–12 µs activity corresponds to the transducer relaxation due to RF coupling. RISHA responses and US echoes have different TOFs. Inset Fourier transform (FFT) shows the differences of their spectral frequency: ultrasound at $f_{US} = f_{RF} = 3.2$ MHz; RISHA at $f_{RISHA} = 2 \times f_{RF} = 6.4$ MHz. (**d–h**) Dual-mode RISHA/US imaging of copper wires soldered at their crossover point. (**d**) Photograph of the wires. (**e**) RISHA image. The dashed arrow indicates the line scanned in panel h, and brown arrows indicate side lobes due to acoustic interference. (**f**) US image. (**g**) Co-registered RISHA (red) and US (green) images. (**h**) Line profile showing a target-to-background ratio (TBR) of 20 dB and a resolution of 475.3 µm. Scale bar, 2 mm.

frequency spectra of the generated RISHA waves and the US echoes are shown in the Fourier analysis in the inset of Fig. 1c. This first demonstration of blood sensing based on its electrical conductivity was achieved herein with second harmonic acoustic signals, due to the use of quasi-continuous excitation and near-field coupling.

RISHA imaging performance. To characterize the RISHA-based blood imaging system and assess its performance, we first analyzed the RISHA responses from a pair of crossed copper wires (200 µm in diameter) soldered together at their crossover point (Fig. 1d). RISHA imaging of the copper wire phantom was performed by scanning the transducer in the xy plane in steps of 100 µm. Figure 1e shows the maximum intensity projection (MIP) of RISHA responses of the crossed copper wires, based on RF energy absorption from the wires (see Methods for details of signal processing and image formation). Figure 1f shows the corresponding US echo image, related to the acoustic impedance of the wires. Figure 1g shows the co-registered dual-mode RISHA/US image, illustrating the complementary contrast of the RISHA signal (rendered in red) to the US echo signal (rendered in green). The US image appears as a 'shadow' of the RISHA image and does not overlap perfectly, due to the constructive and destructive interference patterns of its narrowband acoustic signals, similar to the effect that was reported by Mohajerani et al.[25] and confirmed by our simulations using k-Wave[12] (see Methods for k-Wave simulation, Supplementary Text 2 and Fig. S2).

Figure 1h shows a line profile of the RISHA image of copper wires (along white arrow in Fig. 1e), indicating a target-to-background ratio (TBR) of 20 dB in the RISHA image. Deconvolution[26] of the estimated FWHM by the wire diameter indicates a lateral resolution of 475.3 µm, consistent with the diffraction-limited resolution of 469 µm of the transducer at 6.4 MHz. The achieved lateral resolution is approximately $1/(2.2 \times 10^4)$ of the
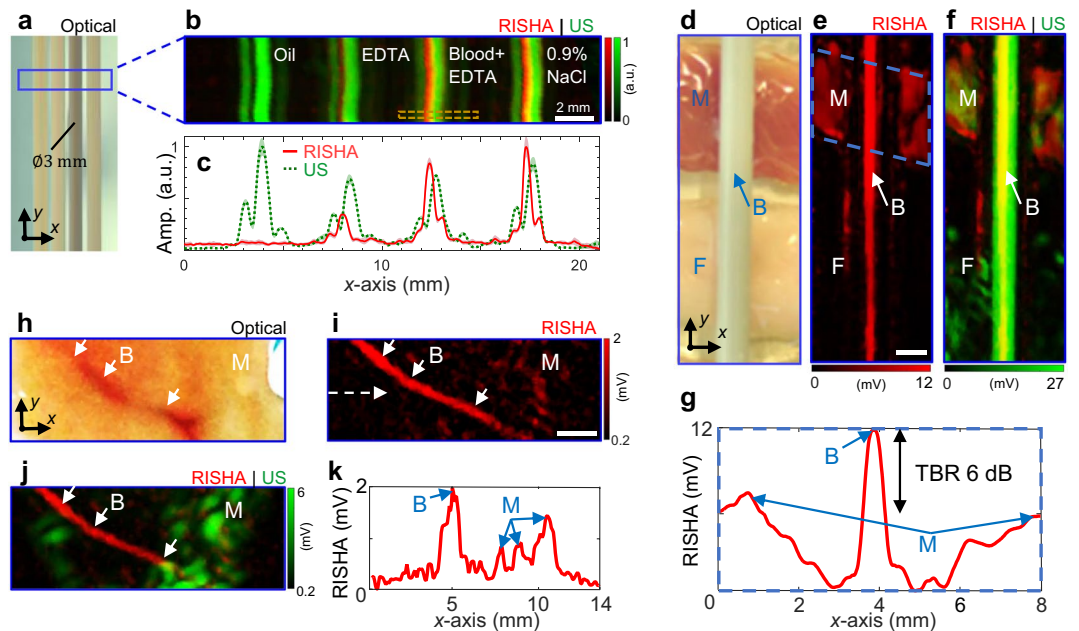
Figure 2. RISHA imaging of blood phantoms. (**a**–**c**) Imaging of polyethylene tubes (ϕ3 mm) filled with vegetable oil, an aqueous solution of anticoagulant EDTA, mouse blood containing the same EDTA concentration as the aqueous solution, or 0.9% NaCl. (**a**) Photograph of the tubes. The blue box indicates the scanned region. (**b**) Co-registered RISHA (red) and US (green) images. The dashed brown box is analyzed in Supplementary Fig. S2. The yellowish color is a result of adding red with green showing the overlapping area of the two contrasts. (**c**) Average of signals from panel b along *y*-axis (40 rows/measurements) showing relative amplitudes of RF absorption (solid red) and US echo (dashed green) in *x*-axis. The shaded color patches that is surrounding the average signal show the standard deviation of the measurements. (**d**–**g**) Imaging of a synthetic phantom containing a tube of mouse blood (B) overlaid on side-by-side pieces of porcine fat (F) and muscle (M). (**d**) Photograph of the phantom. (**e**) RISHA image. The dashed blue box indicates the region analyzed in panel g. (**f**) Co-registered RISHA and US images. The yellowish color is a result of adding red with green showing the overlapping area of the two contrasts. (**g**) Average of RISHA signals in the dashed box in panel e, along the *y*-axis. The resulting projection along the *x*-axis shows two-fold higher RF absorption (TBR 6 dB) by blood than by muscle. (**h**–**k**) Imaging of *ex-vivo* chicken tissue containing a blood vessel and muscle. Arrows indicate blood vessel. (**h**) Photograph of the tissue. (**i**) RISHA image. The dashed arrow indicates a line profile analyzed in panel k. (**j**) Co-registered RISHA and US images. (**k**) Line profile of RISHA signals along the dashed arrow in panel i showing two-fold higher RF absorption by blood than by muscle. Scale bars are 2 mm.

3.2-MHz RF wavelength used, which is 10.5 meters in de-ionized water. This ratio of RISHA resolution to RF wavelength is constant for a given detector *f*-number, which was 2 in our case (see Methods for detailed analysis of imaging resolution).

The axial resolution of RISHA is measured to be ~1.35 mm using the same copper wire due to the relatively long duration of the RF excitation burst, as shown in Supplementary Fig. S3c,d and Text 3. We also note that the axial resolution of RISHA is not limited to 1.35 mm, but can be improved by applying shorter RF-bursts for RISHA signal excitation, and converting RISHA to higher excitation frequencies in the order of 10–100 MHz[17–19].

To study the penetration depth of our RISHA imaging set-up, we imaged a copper wire of 1 mm in diameter at different depths within chicken muscle (Supplementary Text 4 and Fig. S4). The results suggest that the loss/decay of near-field RF energy in thick conductive tissue has a significant impact on the penetration depth of RISHA imaging. In its present state, the dual-mode RISHA/US imager can visualize conductive materials, such as copper wires, with a RISHA target-to-background ratio of 6 dB to a depth of 25 mm in muscle tissue (ultrasound attenuation in soft tissue[27] is 0.75 dB/cm/MHz).

RISHA imaging of blood phantoms. Whole blood exhibits good electrical conductivity (0.98 S/m at 3 MHz), suggesting nearly two-fold (6 dB) greater RF absorption than muscle tissue[28] (0.57 S/m) and 36% less RF absorption than physiological saline solution[29] (1.54 S/m). We examined the RISHA signals collected from four polyethylene tubes (Fig. 2a) filled with vegetable oil, an aqueous solution of anticoagulant ethylenediamine tetraacetic acid (EDTA, 20.1341 μL/500 μL), mouse blood with the same EDTA concentration as the aqueous solution, or 0.9% physiological saline solution (see Methods for sample preparation). The RISHA image (Fig. 2b; rendered in red) shows the RF-absorbing contents of the tubes, which is not seen by ultrasonography (rendered in green). While the US image shows similar signals for all four tubes, RISHA responses vary as expected with electrical conductivity. We show in Fig. 2c the average RISHA/US responses along the *y*-axis of Fig. 2b, together with the standard deviation of the measurements. No RISHA signal was detected from the oil tube, since oil has negligible conductivity at 3.2 MHz, and relatively low RISHA signals were detected from the anticoagulant

EDTA. Conversely, saline demonstrated the highest RISHA signals, and signals from blood showed an amplitude of ~85% of that of saline. The US images in these experiments (Fig. 2b) showed 'shadows', like the ones observed with copper wires (Fig. 1f), which we again attribute to narrowband US wave interference (see Supplementary Text 2 and Fig. S2).

To assess the sensitivity of the RISHA signals to the electrical conductivity differences between blood and surrounding tissue *ex vivo*, we imaged a synthetic experimental sample consisting of a polyethylene tube filled with mouse blood and overlaid with pieces of porcine fat and muscle tissue placed side-by-side (Fig. 2d). RISHA imaging (Fig. 2e,f) clearly resolves the blood and muscle tissue with the expected contrast of 6 dB (Fig. 2g), consistent with the conductivity-based differences of RF absorption. Because of its low conductivity[28] (0.026 S/m), fat tissue was invisible on the RISHA image (Fig. 2e). The tubing and surrounding tissues were visible in the US image (Fig. 2f) because of their strong reflectivity of US waves. The yellow areas in Fig. 2f show the overlap of RISHA signals (red) and US reflections (green). The blood tube appeared thinner on the fat-tissue side in the RISHA image in Fig. 2e, whereas the US image in Fig. 2f indicates that the transducer remained focused along the tube. Therefore, the RISHA signal decrease is unlikely due to the angulated positioning of the tube relatively to the transducer aperture. Instead, this RISHA signal variation can be attributed to the natural sedimentation of red blood cells toward the bottom of the tube, where RF absorption decreases because red blood cells are less conductive than the blood plasma in the upper part of the tube[28,30]. While in Fig. 2b the transducer is focused on the rear wall of the tubing sample, in Fig. 2f the focus of transducer is placed to the center of the tube sample. Due to different foci alignments and the resulting interference of narrowband US waves, the shadow artifact is not visible in Fig. 2f (see also Supplementary Text 2 and Fig. S2).

We further explored whether RISHA imaging could resolve intrinsic contrast of vascular structures within chicken muscle *ex vivo*. A chicken tissue of ~3 mm thick containing a blood vessel (Fig. 2h) was imaged over a 14 mm × 5 mm field of view and clearly revealed an image of the blood vessel with 6-dB contrast between blood and muscle (Fig. 2i,k) and 500-μm resolution. Figure 2j shows the dual-mode RISHA/US image. The US image (green) shows practically no contrast between vasculature and surrounding muscle. Equivalent results were obtained from thicker (5 mm) and more heterogeneous *ex vivo* samples of chicken meat containing dermis, fat and muscle (see Supplementary Text 5 and Fig. S5). In these cases, RISHA imaging resolved vasculature located >3 mm below the surface with a TBR of 12 dB.

RISHA imaging of mouse vasculature.

To complement studies on synthetic phantoms and *ex vivo* tissue, we performed RISHA imaging of a mouse ear after euthanasia. Figure 3a shows the hybrid RISHA/US image overlaid on the microscopic photograph of the scanned mouse ear, revealing that RISHA imaging allows visualization of small vessels in mouse ear with a resolution of ~500 μm, consistent with both our experiments of resolution characterization using copper wire and the diffraction-limited resolution of RISHA imaging at 3.2-MHz RF excitation.

To study the change of blood in electrical conductivity in pre- and post-mortem animal, we also performed RISHA imaging in a mouse tail, both *in vivo* (Fig. 3b) and 30 minutes after mouse euthanasia when blood oxygenation level is low (Fig. 3c; see Methods for mouse experiment procedure). Overlay of co-registered RISHA/US images on the corresponding photographs of the mouse tail pre-mortem (Fig. 3b) and post-mortem (Fig. 3c) gave comparable results: RISHA signals (red) revealed the caudal artery beneath the skin, while US signals (green) provided complementary information about overall tail structure. In this arrangement, RISHA imaging did not detect the lateral or dorsal veins, because we only focused ultrasound detection on the middle caudal artery. An analysis of normalized RISHA signal differences between the pre- and post-mortem states (Fig. 3d–f) revealed amplitude differences of less than 10% between *in vivo* and post mortem, demonstrating that blood conductivity does not depend on blood oxygenation level or other post-mortem changes. Line profiles through the caudal artery in RISHA images *in vivo* and post mortem (Fig. 3f) indicate that the TBR in both RISHA images was above 27 dB, mainly due to the fact that the conductivity of blood in the caudal artery is higher than the conductivity of skin and bone.

Discussion

We have presented a new label-free, non-invasive method to image conductivity paths within dielectric materials, including animal tissues. We showed that RF induces second harmonic acoustic responses and allows blood vessel imaging without the need to administer contrast agents. Imaging experiments *in vivo* and *ex vivo* showed that the RISHA response of blood, i.e. the blood conductivity, is independent of its oxygenation state. Our technique excites samples with RF in the high frequency band (3–30 MHz), and provides a final image resolution 2.2×10^4 times smaller than the excitation wavelength of 10.5 meters. The use of near-field narrowband energy coupling maximizes RISHA response and minimizes energy loss. RISHA imaging requires only inexpensive, widely available RF hardware as well as widely available US detection hardware, enabling simultaneously US pulse-echo imaging of the sample without additional hardware. This dual-mode RISHA/US imaging method allows pixel-by-pixel co-registration of the conductivity path and sample morphology, which provides an intuitive, holistic visual understanding of the sample. Such a technique could be used not only for biomedical imaging, but also for imaging the interior of industrial products, such as integrated circuits, revealing both the conductive paths and morphology of the circuits.

RISHA vasculature imaging offers an alternative to other blood vessel imaging methods by using inexpensive and readily available components that can lead to a low-cost and highly portable sensor. Promising applications of portable RISHA imaging could be general detection of sub-dermal blood vessels for catheter insertion, or inexpensive, disseminated measurements of vasculature, for example in characterizing loss in response to anti-tumor therapies.
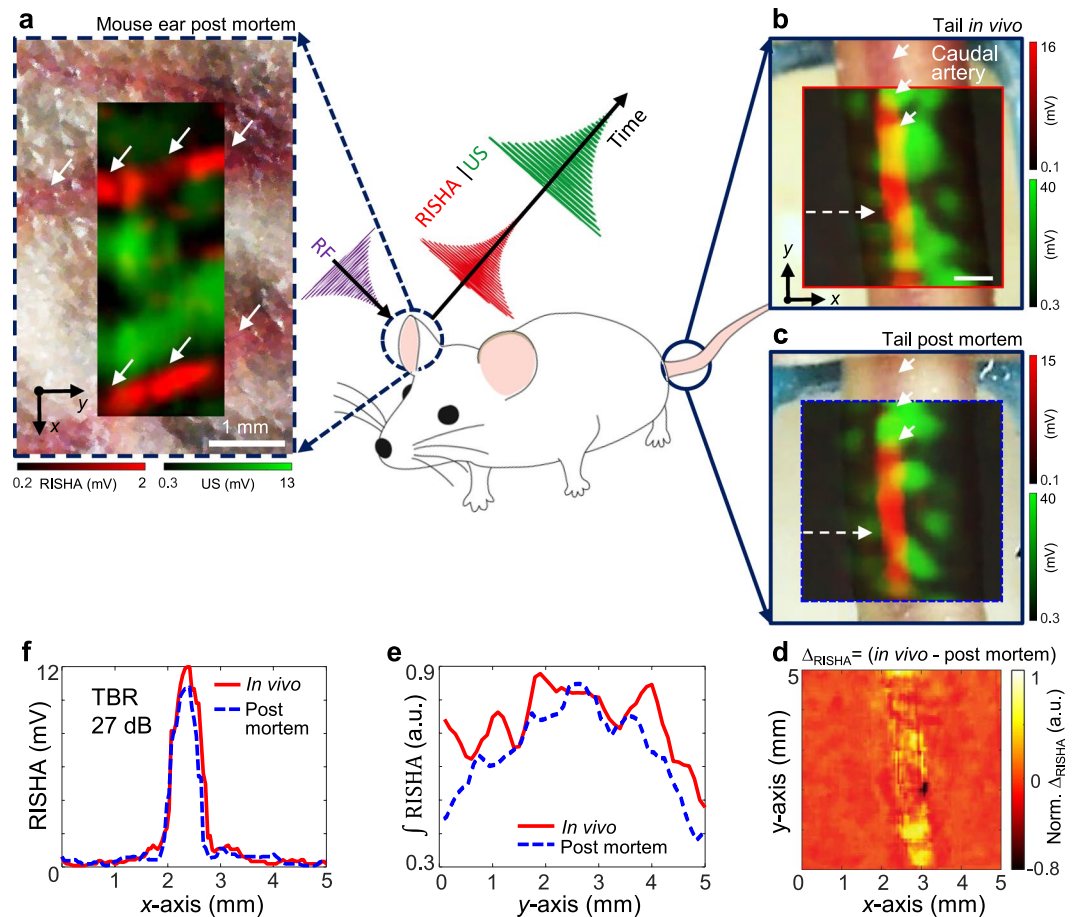
Figure 3. RISHA imaging of vasculature in living and euthanized mouse. An ear (dashed blue circle) of a mouse (illustrated in the center) was imaged after the mouse euthanasia, while the tail (solid blue circle) was imaged *in vivo* and then euthanized. (**a**) Co-registered RISHA (red) and US echo (green) images of an ear in a mouse post mortem, superimposed onto a microscopic photograph of the scanned area displaying small vessels. White arrows indicate blood vessels. (**b**) Co-registered RISHA/US images of mouse tail *in vivo*, superimposed onto the corresponding photograph. The red solid box shows the region scanned *in vivo*. Short white arrows indicate the caudal artery; the dashed arrow indicates the line profile analyzed in panel f for comparison of RF absorption. (**c**) Co-registered RISHA/US image of the same mouse tail as in panel b, but 30 mins after euthanasia of the animal. The dashed blue box shows the same scanned area as in panel *b*. Short white arrows indicate the caudal artery; the dashed arrow indicates the line profile shown in panel f. (**d**) The normalized difference map of RISHA response (arbitrary units, a.u.), $\Delta_{RISHA} = (in\ vivo - post\ mortem)$, obtained by subtracting the post-mortem signal from the pre-mortem signal, showing overall morphological changes. (**e**) The normalized integration ($\int$ RISHA) of RISHA signals in panels b and c along the *x*-axis. The resulting projection along the *y*-axis shows RF absorption by oxygenated blood in the mouse tail *in vivo* (solid red) and by deoxygenated blood after euthanasia (dashed blue). (**f**) Profiles of the lines scanned in RISHA images *in vivo* and post mortem in panels b and c, showing differences <10% in RISHA amplitude of 27 dB TBR. Scale bars are 1 mm.

Our hybrid RISHA/US imaging system enabled dual contrast imaging which was optimized for blood vessel visualization. Better anatomical images using US imaging can be achieved by focusing the transducer on hyperechoic structures like tissue bone or using multiple ultrasound sensors with different focusing depth, or by using a dedicated US pulser/receiver unit as shown in Supplementary Fig. S1a,c.

RISHA imaging has a large dynamic range[15] and can detect blood vessels with a TBR of more than 6 dB in muscle tissue and more than 27 dB in bone/skin tissues, providing a sensitive and non-invasive tool for assessing changes in blood conductivity[31]. Conductivity sensing could be more generally helpful in assessing bulk ionic content in body fluids, such as urine (1.75 S/m), where ion levels are an important marker of renal abnormalities[32,33], offering diagnostic ability in bladder and kidney diseases. Other tissues could also be imaged using RISHA non-invasively aiding to disease diagnosis, including bile (1.4 S/m at 3 MHz), gallbladder (0.9 S/m), cerebrospinal fluid (2.00 S/m), and intervertebral disc (0.83 S/m), to name a few[28,34,35].

It may be possible to bring the resolution of RISHA imaging into the micrometer range by using higher frequencies of acoustic detection (10–300 MHz), and the corresponding radiofrequency excitation (5–150 MHz) based on the second harmonic acoustic generation principle. While conductivity absorption remains as the dominant contrast[19], RISHA of high resolution/frequency may allow label-free visualization of subcellular ion

concentrations, analogous to what has been accomplished with optical/optoacoustic imaging[9]. This could make high-frequency RISHA an intriguing experimental tool for label-free cellular studies of ion transport and related processes. For example, RISHA can directly observe changes in ionic content of living cells in response to RF stimuli[36]. The ability to analyze electro-cellular[37,38] and electro-thermo-cellular interactions may allow RISHA to enrich the bioengineering toolbox with a new, non-invasive electric field method analogous to optics[39], patch-clamp[40], or magnetics based techniques[41–43].

Conventional pulsed thermoacoustic imaging at 434 MHz has been applied for breast cancer detection[44], while higher excitation frequencies at several GHz have been used to image different biological tissues based on their dielectric losses[21–23,45]. These microwave-based thermoacoustic imaging methods provide good soft tissue contrast and the contrast could be further enhanced by administering contrast agents[22,46]. Nevertheless, short-comings include low energy coupling due to far field radiation[17], and poor imaging resolution >1 mm due to the long excitation pulses typically employed (pulse modulation >500 ns). RISHA addresses several limitations of existing thermoacoustic imaging methods by using near-field coupling and quasi-CW excitation in low-MHz range. However, our RISHA imaging system is limited by lack of contrast agents in the low-RF region[46,47]. The development of contrast agent for low frequency RF absorption is challenging and requires detailed understanding of the contrast mechanism in this frequency band[46,48]. Because RISHA imaging is based on inhomogeneous RF excitation in the reactive near-field of coupling elements[17,49], future applications on thick samples larger than a mouse would require RF field strength correction[17,18].

In summary, RISHA imaging demonstrated 6-dB blood-to-muscle contrast, high dynamic range of conductivity detection, and the ability to perform simultaneous RF-induced passive ultrasound imaging using inexpensive instrumentation. We demonstrated the ability to image at depths of up to 2.5 cm in muscle using RISHA imaging. Future system optimizations can improve the resolution and sensitivity, using optimized RF-field excitation and higher frequencies. RISHA imaging could be employed in various biomedical applications non-invasively assessing vasculature, overall tissue electrical conductivity, and also for functional imaging like characterization of the relationship between blood oxygenation and conductivity as well as thermoacoustic Doppler flowmetry of blood flow.

Methods

RISHA imaging set-up. The dual-mode RISHA/US imaging system (Fig. 1a) is driven by a custom-built quasi-continuous wave RF-field generator containing a RC discharging circuit and a custom-built helical coil for near-field energy coupling. The helical coil is wound with 3 mm diameter copper wire and shielded with heat shrink tubing (TF31-9/3, HellermannTyton) with dielectric strength of 37 kV/mm. The quality factor of the RF-field generator is 20, allowing the set-up to provide narrowband stimulation at 5% FWHM-bandwidth (0.16 MHz) and a central frequency of 3.2 MHz. A function generator (33210A, Agilent Technologies) controls the repetition rate of the quasi-continuous RF bursts (1–50 Hz, max 765 mJ per pulse). We performed raster scanning with a spherically focused transducer (V311, Olympus-NDT; central frequency, 10 MHz; focus, 25.4 mm) mounted on xy-translation stages (LTA-HS, ESP 300 controller, Newport Corp) that move across the sample in 100-µm steps in the xy plane corresponding to 1/5th of the diffraction limit of the 6.4 MHz RISHA wave. The coil, sample, and transducer are immersed in a de-ionized water bath to provide efficient US and RF coupling. To remove low frequency oscillation, we used a high-pass RC filter with cutoff frequency at 300 kHz to filter the signal detected by transducer. In our experiments, a 51-dB amplifier (AU-1332, MITEQ) amplified the signals in copper wire experiments, while a 63-dB amplifier (AU-1291, MITEQ) amplified the signals in experiments with biological tissues. The amplified signals were digitized by a digital oscilloscope (TDS3054B, Tektronix). The digitized data were averaged 16 or 32 times and stored on a personal computer, which was also used for synchronizing the raster scanning and for reconstructing the images.

In our *in vivo* measurement, we used 16 times averaged signals, with 50 Hz burst repetition rate. The raster scan step size was set to 100 µm. Considering 0.1 second for the data transmission and stage scan for each data point, the total imaging time for a 10 mm × 10 mm field of view is ~70 mins.

Signal processing and image formation. Co-registered US and RISHA images can be reconstructed based on maximum intensity projections (MIPs) of the acquired acoustic signals: RISHA and US signals were distinguished based on their different frequency spectra and time of flight (Fig. 1b,c). In this work, in order to obtain optimal image target-to-background ratio, MIPs were generated based on the characteristic frequency-doubling in the Fourier spectra of the RISHA and US signals. The temporal sequences were first filtered by a low-pass filter with cutoff frequency of 20 MHz. The amplitude values of the Fourier spectrum at the frequency f_{RISHA} (6.4 MHz, for RISHA signal) or f_{US} (3.2 MHz, for US signal) were then used as the pixel value for each grid point to generate the RISHA and US images, correspondingly. Alternatively, if MIPs were generated in the time domain, a band-pass filter was first applied with a lower cutoff frequency of 2.7 MHz and higher cutoff of 3.7 MHz to the US data; and with 5.9 MHz and 6.9 MHz to the RISHA data, correspondingly. Then the images were filtered using a median filter, and the smallest pixel value was subtracted from all pixels to generate a dark background for better visualization. At each scanning point, RISHA and US signals were derived from the same acquired sequence, so co-registration of the two types of images was achieved simply by assigning the normalized RISHA image to the red channel of an RGB image, and the normalized US image to the green channel.

For better visualization of the mouse ear post mortem (Fig. 3a) and the chicken *ex vivo* results (Supplementary Fig. S5d,e), we applied a mild tubular-structure filter[50] with Gaussian kernels of diameters ranging from 240 to 640 µm, corresponding to the imaging resolution range of our set-up.

RISHA imaging resolution. The diffraction-limited lateral imaging resolution using RISHA (d_{RISHA}) is defined by the RISHA wavelength (λ_{RISHA}) and by the *f*-number of the ultrasound transducer, which is *F/D* (focus length $F = 25.4$ mm and diameter $D = 12.7$ mm). It can be calculated as:

$$d_{RISHA} = \lambda_{RISHA} \cdot \left(\frac{F}{D}\right) = \left(\frac{v_s}{f_{RISHA}}\right) \cdot \left(\frac{F}{D}\right) = \left(\frac{v_s}{2 \times f_{RF}}\right) \cdot \left(\frac{F}{D}\right)$$

(3)

where v_s is the speed of sound in water (1,480 m/s). With de-ionized water as the RF energy and acoustic coupling medium, the frequency of RF excitation relates to RF wavelength λ_{RF} as follows:

$$f_{RF} = \frac{c_0/\sqrt{\varepsilon_r \mu_r}}{\lambda_{RF}}$$

(4)

in which c_0 is the speed of electromagnetic waves in a vacuum (3×10^8 m/s), ε_r is relative permittivity of de-ionized water (80.1 at 20 °C), and μ_r is relative permeability of water ($\mu_r = 1$). Based on Eq. (3) and Eq. (4), lateral resolution with RISHA imaging can be defined as:

$$d_{RISHA} = \left(\frac{v_s \cdot \lambda_{RF}}{2 \times c_0/\sqrt{\varepsilon_r \mu_r}}\right) \cdot \left(\frac{F}{D}\right)$$

(5)

The achievable imaging resolution of RISHA appears to be a fixed fraction of the excitation RF wavelength employed. Substituting numbers into Eq. (5) yields a lateral resolution of 469 μm, corresponding to $1/(2.2 \times 10^4)$ of the RF wavelength at 3.2 MHz (according to Eq. (4), $\lambda_{RF} = 10.5$ meters). Axial resolution of RISHA imaging can then be calculated as $0.80 \times \lambda_{RISHA}$ according to Wang *et al.*[51], yielding a resolution of 188 μm.

Sample preparation: Whole blood and chemical solutions. Polyethylene tubes (Fig. 2a) with a diameter of 3 mm were filled with vegetable oil, an aqueous solution of the anticoagulant ethylenediamine tetraacetic acid (EDTA, 20.1341 μL/500 μL), mouse blood[28] ($\sigma = 0.98$ S/m) containing the same concentration of EDTA, or 0.9% physiological saline solution[29] (NaCl, $\sigma = 1.54$ S/m). To ensure the same concentration of anticoagulant, we used the same type of EDTA anticoagulant microvette (Microvette 500 K3E, Sarstedt) to collect mouse blood and to prepare the tubes containing aqueous solution of EDTA.

Sample preparation: Synthetic phantom and *ex vivo* tissue. A synthetic phantom was prepared by laying the polyethylene tube containing mouse blood on top of side-by-side pieces of porcine muscle and fat tissue *ex vivo* (Fig. 2d). Conductivity of muscle and fat are, 0.57 S/m and 0.026 S/m at 3 MHz and 20°C, respectively[28]. To preserve the ionic content of the porcine muscle and thereby its RF absorptivity, we covered it with low-density polyethylene film with a thickness of 20 μm, which shows similar acoustic impedance at 20 °C ($Z_0 = 1.73$ μPa·s/mm) as water ($Z_0 = 1.48$ μPa·s/mm). This kept acoustic losses below 0.7%. The low electrical conductivity of polyethylene[52] ($\sigma = 10^{-15}$ S/m) meant that RISHA responses at 3 MHz could be entirely attributed to the biological tissue (typically 0.01–1 S/m). The fat tissue in the phantom was not covered with polyethylene film because it was expected to show low RF absorption due to its low conductivity. The fat tissue can also be covered with same polyethylene film immersed in low RF-absorbing oil to preserve its 'RF absorptivity'.

The *ex vivo* chicken soft tissue, shown in Fig. 2h, contained a blood vessel approximately 500 μm wide surrounded by muscle tissue. To conserve its RF absorptivity, this tissue was covered with the same polyethylene film as mentioned above.

Sample preparation: Mouse vasculature experiments. All mouse procedures were approved by the Bavarian Animal Care and Use Committee and all experiments were performed in accordance with the guidelines and regulations approved by the Government of Bavaria, Germany. All imaging experiments have been performed with RF energy levels well within the safety standards defined by IEEE Standard for Safety Levels with Respect to Human Exposure to Radio Frequency Electromagnetic Fields, 3 kHz to 300 GHz[53]. The ear and tail of a CD-1 nude mouse were imaged using our dual-mode RISHA/US set-up. For *in vivo* measurements of the tail (Fig. 3b), the mouse was first anesthetized for 90 minutes by intraperitoneal injection of ketamine/xylazine (0.1 mL/g of mouse weight with 1 mL ketamine 100 mg/mL, 0.25 mL xylazine 20 mg/mL, and 6 mL physiology saline solution), then it was placed on a custom-built mouse bed above water level, and kept warm by an infrared lamp. During the experiment, the mouse tail was fixed to a 3D-printed imaging frame (blue PLA material in Fig. 3b,c) and immersed in de-ionized water. For tail imaging of the mouse after euthanasia (Fig. 3c), the animal was first injected intraperitoneally with 40 μL heparin (25 000 I.E./5 mL, Heparin-Natrium Braun) to keep blood from coagulating, and then the anesthetized mouse was sacrificed by cervical dislocation. While keeping the mouse in the same position on the mouse bed, we waited for 30 minutes to ensure low hemoglobin oxygenation level in blood. Then we scanned the tail again under the same conditions as for *in vivo* imaging. Upon finishing imaging of the mouse tail after euthanized, we changed the mouse position so that the ear was fixed to the imaging frame and scanned (Fig. 3a) under the same conditions as for the tail.

k-Wave simulation. Acoustic interference that is caused by a tube with a diameter of 3 mm and wall thickness of 0.1 mm was simulated using the k-Wave Matlab toolbox[12]. The computational grid size was set to 0.1 mm, same as the mechanical scanning step size. The ultrasound transducer characteristics were as follows: central frequency, 10 MHz; bandwidth, 73.45%; focus distance, 25.4 mm; diameter, 12.7 mm. Mass density of polyethylene material was defined to be 940 kg/m³ and ultrasound speed to be 2080 m/s. The coupling medium was water, with

a mass density of 998 kg/m³ and a speed of sound of 1,500 m/s. A time-varying, 3.2-MHz quasi-continuous US wave was specified for the transducer elements, and a time-varying RISHA wave of 6.4 MHz was specified for the aqueous content within the tube. The transducer was moved across the sample to simulate raster scanning. Signal processing and image reconstruction algorithms used in the simulation were similar to those used in imaging experiments. The analysis and result are shown in Supplementary Text 2 and Fig. S2.

Data Availability

The raw data that support the findings of this study, and the Matlab programs that are used to collect, process and reconstruct the data are available from the corresponding authors on request.

References

1. Omar, M., Schwarz, M., Soliman, D., Symvoulidis, P. & Ntziachristos, V. Pushing the optical imaging limits of cancer with multi-frequency-band raster-scan optoacoustic mesoscopy (RSOM). *Neoplasia* **17**, 208–214 (2015).
2. Dronkers, C. E., Klok, F. A. & Huisman, M. V. Current and future perspectives in imaging of venous thromboembolism. *J. Thromb. Haemost.* **14**, 1696–1710 (2016).
3. Carmeliet, P. & Jain, R. K. Angiogenesis in cancer and other diseases. *Nature* **407**, 249–257 (2000).
4. Pandian, N. G. *et al.* Ultrasound angioscopy: real-time, two-dimensional, intraluminal ultrasound imaging of blood vessels. *Am. J. Cardiol.* **62**, 493–494 (1988).
5. Errico, C. *et al.* Ultrafast ultrasound localization microscopy for deep super-resolution vascular imaging. *Nature* **527**, 499–502 (2015).
6. Camici, P. G., d'Amati, G. & Rimoldi, O. Coronary microvascular dysfunction: mechanisms and functional assessment. *Nat. Rev. Cardiol.* **12**, 48–62 (2015).
7. Taruttis, A. *et al.* Optoacoustic Imaging of Human Vasculature: Feasibility by Using a Handheld Probe. *Radiology* **281**, 256–263 (2016).
8. Taruttis, A. & Ntziachristos, V. Advances in real-time multispectral optoacoustic imaging and its applications. *Nat. Photonics* **9**, 219–227 (2015).
9. Omar, M., Soliman, D., Gateau, J. & Ntziachristos, V. Ultrawideband reflection-mode optoacoustic mesoscopy. *Opt. Lett.* **39**, 3911–3914 (2014).
10. Aguirre, J. *et al.* Precision assessment of label-free psoriasis biomarkers with ultra-broadband optoacoustic mesoscopy. *Nat. Biomed. Eng.* **1**, 0068 (2017).
11. Huang, D. *et al.* Optical coherence tomography. *Science* **254**, 1178–1181 (1991).
12. Treeby, B. E. & Cox, B. T. k-Wave: MATLAB toolbox for the simulation and reconstruction of photoacoustic wave fields. *J. Biomed. Opt.* **15**, 021314 (2010).
13. Chugh, B. P. *et al.* Measurement of cerebral blood volume in mouse brain regions using micro-computed tomography. *Neuroimage* **47**, 1312–1318 (2009).
14. Lentschig, M. G. *et al.* Breath-hold gadolinium-enhanced MR angiography of the major vessels at 1.0 T: dose-response findings and angiographic correlation. *Radiology* **208**, 353–357 (1998).
15. Kellnberger, S., Omar, M., Sergiadis, G. & Ntziachristos, V. Second harmonic acoustic responses induced in matter by quasi continuous radiofrequency fields. *Appl. Phys. Lett.* **103**, 153706 (2013).
16. Kellnberger, S. *et al.* Magnetoacoustic Sensing of Magnetic Nanoparticles. *Phys. Rev. Lett.* **116**, 108103 (2016).
17. Razansky, D., Kellnberger, S. & Ntziachristos, V. Near-field radiofrequency thermoacoustic tomography with impulse excitation. *Med. Phys.* **37**, 4602–4607 (2010).
18. Kellnberger, S., Hajiaboli, A., Razansky, D. & Ntziachristos, V. Near-field thermoacoustic tomography of small animals. *Phys. Med. Biol.* **56**, 3433–3444 (2011).
19. Omar, M., Kellnberger, S., Sergiadis, G., Razansky, D. & Ntziachristos, V. Near-field thermoacoustic imaging with transmission line pulsers. *Med. Phys.* **39**, 4460–4466 (2012).
20. Bowen, T. In *1981 Ultrasonics Symposium* 817–822 (IEEE, Chicago, IL, USA, 1981).
21. Ku, G. & Wang, L. V. Scanning microwave-induced thermoacoustic tomography: signal, resolution, and contrast. *Med. Phys.* **28**, 4–10 (2001).
22. Mashal, A., Booske, J. H. & Hagness, S. C. Toward contrast-enhanced microwave-induced thermoacoustic imaging of breast cancer: An experimental study of the effects of microbubbles on simple thermoacoustic targets. *Phys. Med. Biol.* **54**, 641–650 (2009).
23. Aliroteh, M. S. & Arbabian, A. Microwave-Induced Thermoacoustic Imaging of Subcutaneous Vasculature With Near-Field RF Excitation. *IEEE Trans. Microw. Theory Tech.* **66**, 577–588 (2018).
24. Ding, W. Z., Ji, Z. & Da, X. I. N. G. Microwave-excited ultrasound and thermoacoustic dual imaging. *Appl. Phys. Lett.* **110**, 183701 (2017).
25. Mohajerani, P., Kellnberger, S. & Ntziachristos, V. Frequency domain optoacoustic tomography using amplitude and phase. *Photoacoustics* **2**, 111–118 (2014).
26. Soliman, D., Tserevelakis, G. J., Omar, M. & Ntziachristos, V. Combining microscopy with mesoscopy using optical and optoacoustic label-free modes. *Sci. Rep.* **5**, 12902, https://doi.org/10.1038/srep12902 (2015).
27. Beard, P. Biomedical photoacoustic imaging. *Interface Focus* **1**, 602–631 (2011).
28. Gabriel, S., Lau, R. W. & Gabriel, C. The dielectric properties of biological tissues: II. Measurements in the frequency range 10 Hz to 20 GHz. *Phys. Med. Biol.* **41**, 2251–2269 (1996).
29. Mazzoleni, A. P., Sisken, B. F. & Kahler, R. L. Conductivity values of tissue culture medium from 20 °C to 40 °C. *Bioelectromagnetics* **7**, 95–99 (1986).
30. Hirsch, F. G. *et al.* The electrical conductivity of blood. I: Relationship to erythrocyte concentration. *Blood* **5**, 1017–1035 (1950).
31. Abdalla, S., Al-Ameer, S. S. & Al-Magaishi, S. H. Electrical properties with relaxation through human blood. *Biomicrofluidics* **4**, 34101 (2010).
32. Wang, J. M. *et al.* Evaluating the performance of urine conductivity as screening for early stage chronic kidney disease. *Clin. Lab.* **60**, 635–643 (2014).
33. Manoni, F. *et al.* Laboratory diagnosis of renal failure: urine conductivity and tubular function. *Minerva Urol. Nefrol.* **61**, 17–20 (2009).
34. Gabriel, S., Lau, R. W. & Gabriel, C. The dielectric properties of biological tissues: III. Parametric models for the dielectric spectrum of tissues. *Phys. Med. Biol.* **41**, 2271–2293 (1996).
35. Hasgall, P. *et al.* IT'IS Database for thermal and electromagnetic parameters of biological tissues, https://www.itis.ethz.ch/database (2018).
36. Grossman, N. *et al.* Noninvasive Deep Brain Stimulation via Temporally Interfering Electric Fields. *Cell* **169**, 1029–1041 e1016 (2017).
37. Bassett, C. A. & Pawluk, R. J. Electrical behavior of cartilage during loading. *Science* **178**, 982–983 (1972).
38. Shamos, M. H. & Lavine, L. S. Piezoelectricity as a Fundamental Property of Biological Tissues. *Nature* **213**, 267–269 (1967).

39. Boyden, E. S., Zhang, F., Bamberg, E., Nagel, G. & Deisseroth, K. Millisecond-timescale, genetically targeted optical control of neural activity. *Nat. Neurosci.* **8**, 1263–1268 (2005).
40. Mainen, Z. F. & Sejnowski, T. J. Reliability of spike timing in neocortical neurons. *Science* **268**, 1503–1506 (1995).
41. Munshi, R. *et al.* Magnetothermal genetic deep brain stimulation of motor behaviors in awake, freely moving mice. *Elife* **6**, e27069 (2017).
42. Drude, P. Zur elektronentheorie der metalle; II. Teil. galvanomagnetische und thermomagnetische effecte. *Ann. Phys. (Berl.)* **308**, 369–402 (1900).
43. Drude, P. Zur elektronentheorie der metalle; I. Teil. *Ann. Phys. (Berl.)* **306**, 566–613 (1900).
44. Kruger, R. A. *et al.* Breast cancer *in vivo*: contrast enhancement with thermoacoustic CT at 434 MHz-feasibility study. *Radiology* **216**, 279–283 (2000).
45. Nie, L., Xing, D., Zhou, Q., Yang, D. & Guo, H. Microwave-induced thermoacoustic scanning CT for high-contrast and noninvasive breast cancer imaging. *Med. Phys.* **35**, 4026–4032 (2008).
46. Ogunlade, O. & Beard, P. Exogenous contrast agents for thermoacoustic imaging: an investigation into the underlying sources of contrast. *Med. Phys.* **42**, 170–180 (2015).
47. Tamarov, K. *et al.* Electrolytic conductivity-related radiofrequency heating of aqueous suspensions of nanoparticles for biomedicine. *Phys. Chem. Chem. Phys.* **19**, 11510–11517 (2017).
48. Pramanik, M., Swierczewska, M., Green, D., Sitharaman, B. & Wang, L. V. Single-walled carbon nanotubes as a multimodal-thermoacoustic and photoacoustic-contrast agent. *J. Biomed. Opt.* **14**, 034018 (2009).
49. Nikitin, P. V., Rao, K. V. S. & Lazar, S. In 2007 IEEE *International Conference on RFID*. 167–174 (2007).
50. Jerman, T., Pernus, F., Likar, B. & Spiclin, Z. Enhancement of Vascular Structures in 3D and 2D Angiographic Images. *IEEE Trans. Med. Imaging* **35**, 2107–2118 (2016).
51. Xu, M. H. & Wang, L. H. V. Photoacoustic imaging in biomedicine. *Rev. Sci. Instrum.* **77**, 041101 (2006).
52. Adamec, V. & Calderwood, J. H. On the determination of electrical conductivity in polyethylene. *J. Phys. D: Appl. Phys.* **14**, 1487–1494 (1981).
53. IEEE Standard for Safety Levels with Respect to Human Exposure to Radio Frequency Electromagnetic Fields, 3 kHz to 300 GHz, https://doi.org/10.1109/IEEESTD.2006.99501 (2006).

Acknowledgements

Author Contributions

Y.H., S.K. and V.N. designed the research. Y.H. and S.K. contributed equally and performed the research. S.K. supervised the project, built the RF-field generator and designed the first set-up. Y.H. built the final dedicated imaging set-up, designed the image reconstruction algorithms and performed experiments. Y.H., S.K., G.S. and V.N. analyzed the data and wrote the paper.

Additional Information

Supplementary information accompanies this paper at https://doi.org/10.1038/s41598-018-33732-0.

Competing Interests: The authors declare no competing interests.

Publisher's note: Springer Nature remains neutral with regard to jurisdictional claims in published maps and institutional affiliations.

Supplementary Information for

Blood vessel imaging using radiofrequency-induced second harmonic acoustic response

Yuanhui Huang[+], Stephan Kellnberger[+,*], George Sergiadis, Vasilis Ntziachristos[*]

[+]Y.H.H. and S.K. contributed equally to this work.
[*]Correspondence should be addressed to S.K. (stephan.kellnberger@tum.de) or to V.N. (v.ntziachristos@tum.de).

This SI file includes:

Supplementary Text 1. Ultrasound signal amplitude comparison between conventional pulse/echo ultrasound and US signals generated by our RF-induced source.

Supplementary Text 2. Simulation of narrowband acoustic interference.

Supplementary Text 3. Depth resolving and axial resolution of RISHA imaging.

Supplementary Text 4. RISHA imaging depth in muscle tissue.

Supplementary Text 5. RISHA imaging of heterogeneous tissue *ex vivo*.

Supplementary Figure S1. Ultrasound signal amplitude comparison between conventional pulse/echo ultrasound and US signals generated by our RF-induced source.

Supplementary Figure S2. K-Wave simulation study of narrowband acoustic interference.

Supplementary Figure S3. Depth resolving and axial resolution of RISHA imaging.

Supplementary Figure S4. RISHA imaging in deep muscle tissue.

Supplementary Figure S5. RISHA imaging of heterogeneous biological tissue *ex vivo*.

Supplementary Text

Supplementary Text 1. Ultrasound signal amplitude comparison between conventional pulse/echo ultrasound and US signals generated by our RF-induced source.

We performed experiments to quantitatively compare the US signal strengths generated by RISHA to an US wave generated with a commercially available pulser/receiver unit (Pulser/Receiver unit 5077PR, Olympus-Panametrics, USA).

In these experiments, we used a focused ultrasound transducer (V311, central frequency, 10 MHz; bandwidth, 73.45%; focus distance, 25.4 mm; diameter, 12.7 mm, Olympus-NDT, USA) which we also employed in our RISHA imaging studies. For conventional US generation, the transducer is driven by the pulser/receiver unit with a voltage amplitude of 200 Volt. In the RF-induced US generation experiment, the transducer is driven by energy emitted from the 3.2 MHz RF pulser used for RISHA signal generation.

In a first set of experiments shown in Supplementary Fig. S1a, we quantitatively compared the transducer relaxation signal amplitude from the pulser/receiver unit (Experiment 1, dashed blue line) with the US-signal generated by the RISHA setup (Experiment 2, solid green line).

Experiment 1 - Pulser/receiver signal amplitude: Using a 200 V pulse amplitude, we measured a transducer relaxation amplitude of 743.3 mV based on -49 dB signal attenuation. This signal corresponds to the pulse amplitude of 743.3×10^{-3} Volt $\times$ 281.8 = 209.5 Volt generated by the pulser/receiver.

Experiment 2 - RISHA excitation signal amplitude: Using RISHA excitation pulses with

765 millijoule (mJ) per pulse, we measured a transducer relaxation (RF-induced US emission) peak amplitude of -99.6 mV.

According to this experiment, the difference between conventional pulser/receiver generated US and RF-induced US is 66 dB, or a factor of 2.1×10^3.

We further investigated US signal amplitudes of the pulser/receiver and the RISHA setup in pulse/echo mode on an ultrasound phantom consisting of two tubes. Supplementary Fig. S1b shows the phantom used for this study and Supplementary Fig. S1c,d displays the experimental results of the B-scan. When using the conventional US pulser/receiver unit, we recorded a peak US-echo amplitude of 73.9 mV, without any amplification or attenuation. When using RF-induced US generation, we recorded a peak US-echo amplitude of 65.2 mV, but with a 63-dB amplification (increased by 1412.5 times in voltage, AU-1291, MITEQ), corresponding to a maximum amplitude of RF-induced US echo of 65.2 mV $\div$ 1412.5 = 46.2 µV.

This experimental comparison yields a difference of 1.6×10^3, corresponding to 64 dB, between conventional US and RF-induced US, being in the same order as the transducer relaxation experiment.

Supplementary Text 2. Simulation of narrowband acoustic interference.
Supplementary Fig. S2a,b shows the misalignment appearing as 'shadow' from experimental dual-mode RISHA/US image of blood tubing in Fig. 2b, which we attribute to the narrowband characteristics of the transmitted US wave and possibly to destructive and constructive interferences of US waves back-reflected from the sample. To test this hypothesis, we used the k-Wave toolbox (see Methods) to demonstrate that when the

transducer is focused on the rear surface of the tubing, the simulated dual-mode image (Supplementary Fig. S2c) is similar to the experimental blood tubing image (Supplementary Fig. S2a). The simulated line profile (Supplementary Fig. S2d) is like the experimental one (Supplementary Fig. S2b), indicating a shift of approximately 300 μm between the RISHA and US signal peaks. Therefore, we suggest that the acoustic interference of narrowband excitation at 3.2 and 6.4 MHz causes the visual 'shadow' effect in the dual-mode RISHA/US images.

While in Fig. 2b the transducer is focused on the rear wall of the tubing sample, in Fig. 2f the focus of transducer is placed to the center of the tube sample. Due to different foci alignments and the resulting interference of narrowband US waves, the shadow artifact is not visible in Fig. 2f.

The simulation shows also side lobes in the RISHA signal (Supplementary Fig. S2c,d), which coincide with those that we observed in our copper wire experiments for determining imaging resolution (Fig. 1e,h). Therefore, we suggest that these side lobes also result from constructive and destructive interference of RISHA waves at 6.4 MHz.

Acoustic interference, in addition to explaining the 'shadow' effect and the appearance of side lobes, also explains why the full width at half maximum of our copper wire phantom in US images (~1.5 mm) appears 50% larger than the diffraction-limited resolution of 940 μm predicted for the transducer at 3.2 MHz (Fig. 1f). Therefore, acoustic interference affects the apparent US lateral resolution in US imaging mode. It may be possible to reduce these interference effects by including more frequency components when exciting samples and when reconstructing RISHA and US images.

Supplementary Text 3. Depth resolving and axial resolution of RISHA imaging.

As shown in Fig. 1b,c, RISHA enables spatial differentiation of objects in the axial direction based on time-of-flight measurements, similar to conventional time-domain optoacoustic imaging.

Firstly, to show the spatial differentiation of objects, we performed RISHA imaging on the tube samples shown in Supplementary Fig. S1b. The results are shown in Supplementary Fig. S3a,b, demonstrating that RISHA can clearly resolve the four walls of the two tube samples in axial direction.

In a second experiment, we quantitatively characterized the axial resolution of our RISHA imaging setup using the thin copper wire samples (diameter: Ø200 µm) used in Fig. 1d-h. The reconstructed RISHA B-scan of the wire is shown in Supplementary Fig. S3c, while Supplementary Fig. S3d shows the line profile of the wire indicated by the red arrow in Supplementary Fig. S3c. From the peak envelope function of the RISHA burst, we calculated a full-width at half-maximum (FWHM) of 0.9 µs which corresponds to approximately 1.35 mm.

Correspondingly, applying deconvolution of the imaged object[1], we calculated the axial resolution of the current RISHA system to 1.348 mm.

We note that, due to the relatively long duration of the RF excitation burst[2], the axial resolution of RISHA is currently limited to 1.35 mm. However, future improvements such as shorter bursts and higher excitation frequencies[3-5] can improve resolution.

Supplementary Text 4. RISHA imaging depth in muscle tissue.

To investigate the depth-penetration of RISHA imaging using low-MHz near-field RF energy, we constructed phantoms consisting of a copper wire inserted at different depths within *ex vivo* chicken muscle tissue (Supplementary Fig. S4a,b). A copper wire of 1-mm diameter was used as a reference for non-soft tissue penetration (0 mm penetration). Two phantoms were constructed (Supplementary Fig. S4a): phantom 1 consisted of the same copper wire inserted into the center of a piece of chicken muscle approximately 20 mm thick, resulting in propagation distances of 10 mm for incoming RF energy, 10 mm for outgoing RISHA waves, and 20 mm for roundtrip propagation of US waves in tissue; phantom 2 was constructed with the same copper wire as phantom 1, but with muscle tissue approximately 45 mm thick, giving a propagation distance of 25 mm for incoming RF energy, 20 mm for outgoing RISHA waves, and 40 mm for US wave roundtrip in tissue.

We performed RISHA/US imaging of these phantoms and observed loss of image quality with deeper penetration. Supplementary Fig. S4c shows dual-mode RISHA/US imaging of the reference copper wire in the absence of tissue, providing optimal imaging at "zero" penetration depth in muscle. Supplementary Fig. S4d shows copper imaging with the 20-mm thick tissue in phantom 1; Supplementary Fig. S4e shows the results with the 45-mm thick tissue in phantom 2. The loss of image quality with increasing penetration depth was confirmed by RISHA line profiles along the *x*-axis, as shown in Supplementary Fig. S4f. However, RISHA imaging maintained a target-to-background ratio (TBR) of approximately 6 dB for copper in the 45-mm muscle tissue. Supplementary Fig. S4g shows that the TBR of the corresponding US images depends less on depth. Although the frequencies of RISHA waves (6.4 MHz) and US waves

(3.2 MHz) detected in these images have a ratio of 2/1, the discrepancy in TBR between RISHA and US imaging is not likely to be a result of frequency-dependent ultrasound attenuation, which is empirically known to be 0.75 dB/cm/MHz in soft tissue[6], when the ratio of distances traveled by RISHA and US waves is considered.

These experimental results suggest that RF energy losses and the near-field distribution characteristics of the RF energy are the key determinants of penetration depth during RISHA imaging of thick conductive tissue. In its current state, the RISHA set-up allows imaging of conductive material at a TBR of 6 dB to a depth of 25 mm in muscle tissue.

Supplementary Text 5. RISHA imaging of heterogeneous tissue *ex vivo*.

In addition to imaging homogeneous chicken muscle, we also imaged more complicated, heterogeneous tissues (see Methods for sample preparation). These experiments demonstrate the rich contrast for differentiating conductive/RF-absorbing tissues at depths greater than several millimeters using RISHA imaging.

We firstly imaged chicken dermis ~5 mm thick (Supplementary Fig. S5a-c). To prevent ionic content of tissue leaching into de-ionized water, we immersed the samples in low RF-absorbing oil and wrapped them in polyethylene film. Supplementary Fig. S5c shows the dual-mode RISHA/US image with the transducer focused beneath the skin, revealing rich details of tissue heterogeneity, potentially corresponding to microstructures such as blood vessels or capillaries, glands, and other structures. The RISHA image (in red) shows tubular structures that are likely to be blood capillaries, while the corresponding US image (in green) shows skin folds of different ultrasound reflectivity.

In another chicken muscle sample of >5 mm thickness (Supplementary Fig. S5d,e),

RISHA imaging reveals similar tubular blood vessels at a depth (>3 mm) where the

vessels are invisible in the optical photograph (Supplementary Fig. S5e).

Supplementary Figures
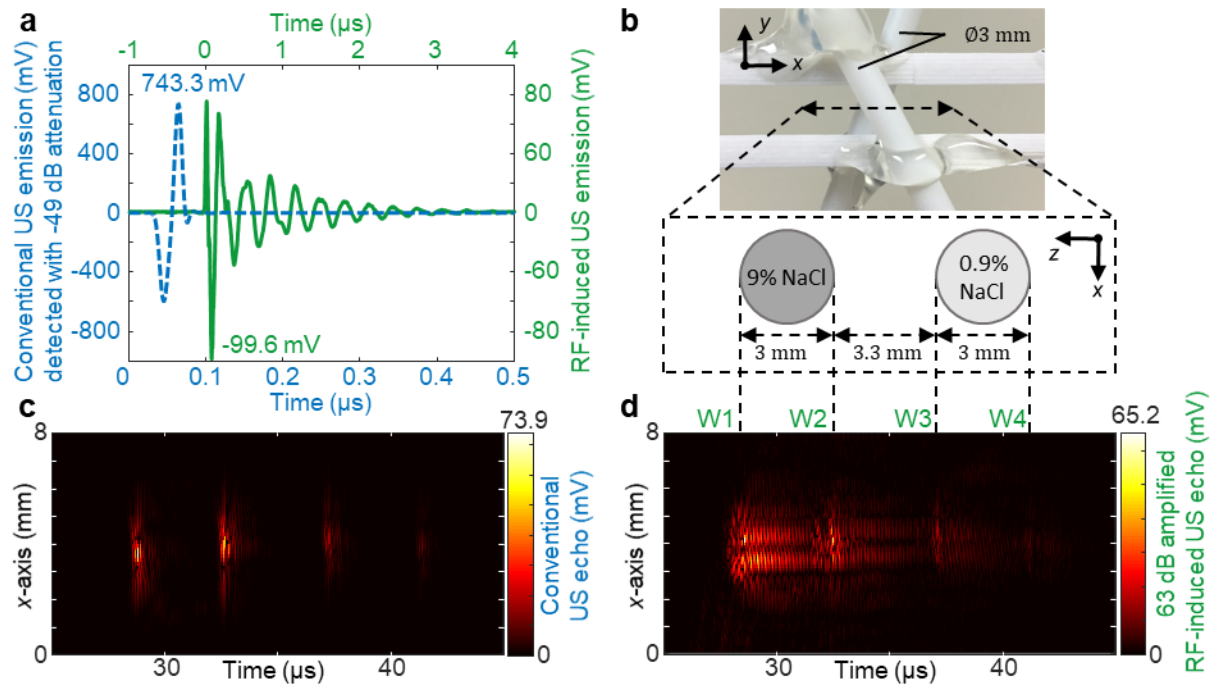
Supplementary Figure S1. Ultrasound signal amplitude comparison between conventional pulse/echo ultrasound and US signals generated by our RF-induced source. (**a**) Ultrasound emission amplitude comparison between a commercial pulser/receiver unit (dashed blue, conventional US emission, -49 dB attenuated) and the RF-induced method (solid green, RF-induced US emission). (**b-d**) Experimental results showing comparison of the ultrasound echo amplitude generated by (c) conventional and (d) our RF-induced source. (**b**) Photograph of two tubing samples (outer diameter Ø3 mm, wall thickness 100 µm) that were used in US pulse/echo imaging experiment. The tubes were filled with 9% and 0.9 % NaCl saline solution. The samples were fixated onto a 3D-printed holder and separated in axial direction (*z*-axis) by 3.3 mm. The focus of ultrasound transducer (focal length 25.4 mm, US echo appears at 33.8 µs) was positioned between the two tubing samples. (**c**) US B-scan result using conventional pulse/echo

ultrasound. The maximum US echo amplitude recorded without amplification is 73.9 mV. (**d**) US B-scan using RF-induced US generation by RISHA setup. The maximum RF-induced US echo amplitude recorded with 63 dB amplification is 65.2 mV. W1-4 indicate the temporal position of the four walls of the tubes in US echo sequence.
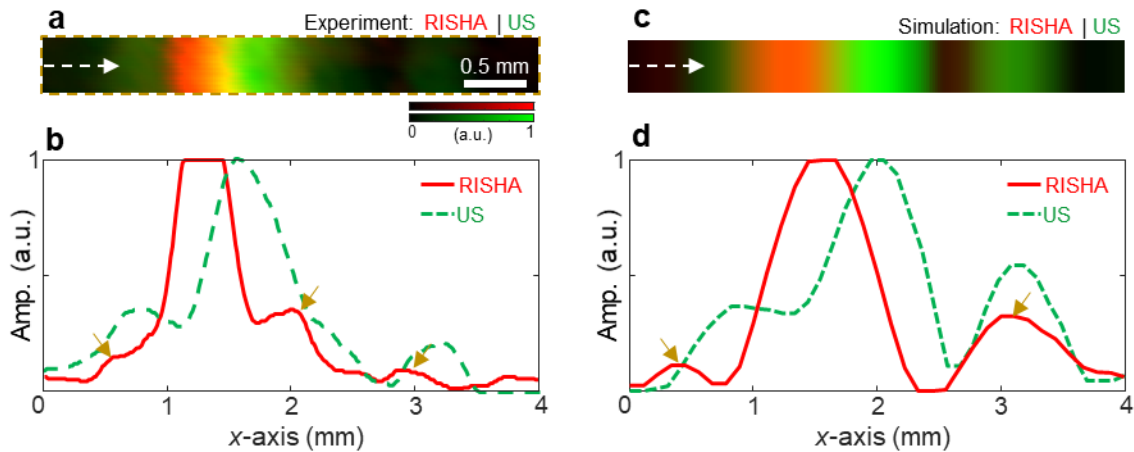
Supplementary Figure S2. k-Wave simulation study of narrowband acoustic interference. (**a**) Enlarged experimental RISHA/US image of blood tubing area enclosed in the dashed brown box in Fig. 2b, showing the 'shadow' effect on the US image (rendered in green). The red channel is the RISHA image. The dashed arrow indicates the line profiled in panel b. (**b**) Profiles of RISHA signal and US signal in experimental image of tubing sample. (**c-d**) k-Wave simulation of RISHA/US imaging of tubing with a diameter of 3 mm containing conductive sample, like the experimental phantom of tubing containing blood. (**c**) Simulated dual-mode RISHA/US image showing similar 'shadow' effect acquired when the focus of the transducer was set to the rear surface of the tubing sample. The dashed arrow indicates the line profiled in panel d. (**d**) Simulated profiles of RISHA signal and US signal along the arrow in panel c, showing lateral displacement of

~300 μm due to acoustic interference. Brown arrows indicate side lobes, which are also visible in the experimental RISHA images of copper wires in Fig. 1e,h. Scale bar, 0.5 mm.
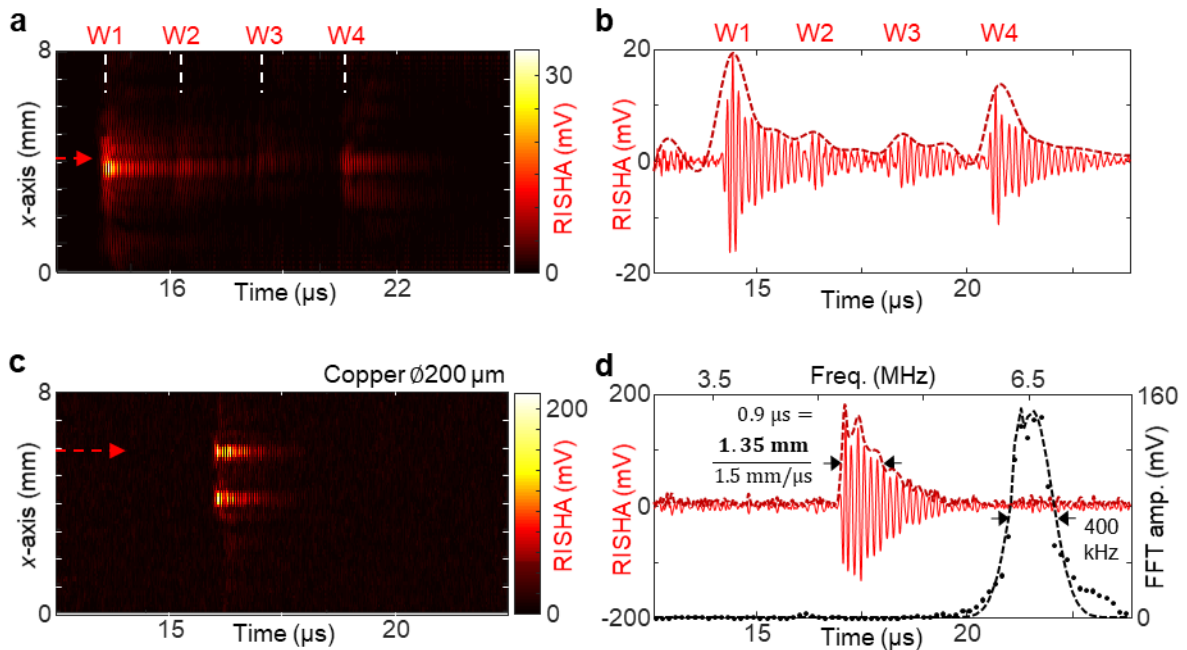
**Supplementary Figure S3. Depth resolving and axial resolution of RISHA imaging.**
(**a-b**) Depth-resolution performance of RISHA imaging. (**a**) RISHA B-scan of tube samples as shown in Supplementary Fig. S1, showing the ability of RISHA to resolve the tubes in the axial direction. The focus of ultrasound transducer (RISHA signal appears at 16.9 μs) was positioned between the two tubing samples. The dashed white line segments indicate in axial direction the position of the four walls (W1-4) of the tubing samples. The dashed red arrow indicates the line profile shown in panel b. (**b**) The temporal waveform of RISHA signal acquired at position indicated by arrow in panel a. The temporal waveform shows the time-of-flight difference of four walls of the two tube samples as indicated by location of W1-4 corresponding to the signal peak envelope. (**c-**

d) RISHA axial resolution characterization. (**c**) RISHA B-scan of the copper wires

sample with diameter Ø200 µm along the dashed white arrow in Fig. 1e. The dashed red

arrow indicates the line profile analyzed in panel d. (**d**) The temporal waveform of

RISHA signal (solid red) acquired at position indicated by arrow in panel c. The RISHA

burst duration is estimated from the peak envelope of the RISHA signal (dashed dark red)

to be 3.3 µs; the FWHM of the RISHA burst duration is then estimated from the peak

envelope function to be 0.9 µs, corresponding to a size of 1.35 mm given speed of sound

of 1.5 mm/µs. The Fourier transform (FFT, dashed black curve fitted using FFT data

points) shows the central frequency (6.5 MHz) and FWHM bandwidth (400 kHz) of the

RISHA signal.
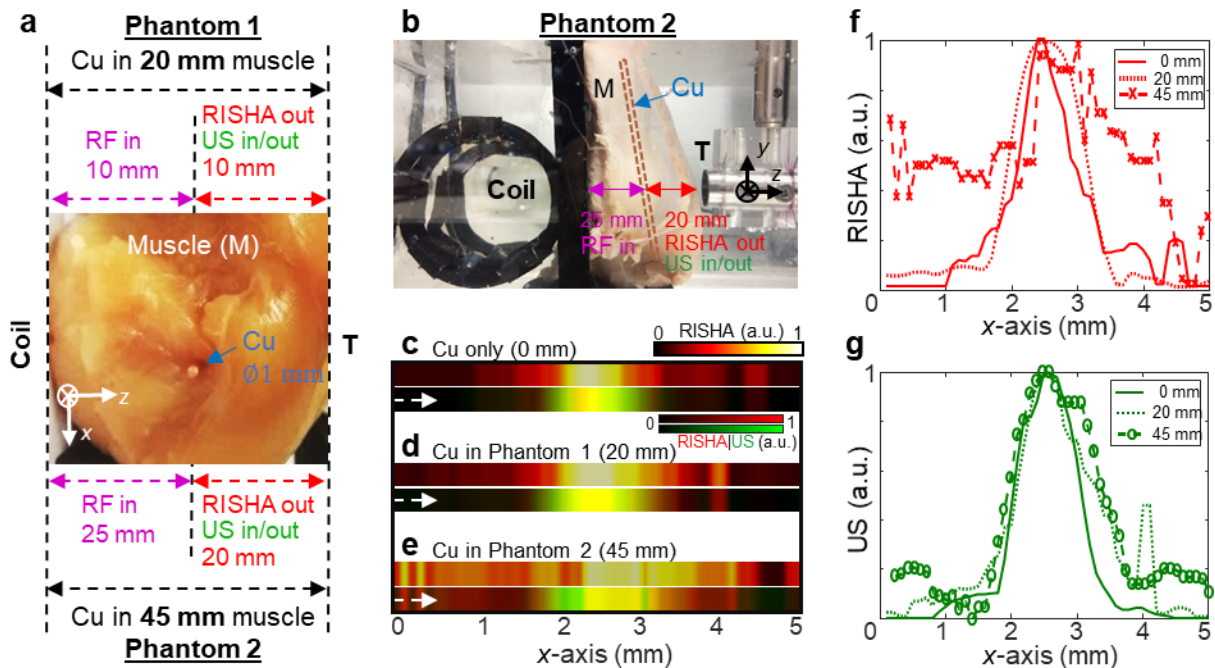
Supplementary Figure S4. RISHA imaging in deep muscle tissue. (**a**) Cross-sectional

photograph of the phantoms showing penetration depth. As indicated, phantoms were

placed between the energy coupling coil and the ultrasound transducer (T). Phantom 1

comprised chicken muscle (M) ~20 mm thick containing in its center a copper wire (Cu, Ø1 mm, blue arrow), providing 10 mm RF penetration depth, 10 mm RISHA wave travel distance to transducer, and 20 mm roundtrip US travel distance in tissue. Phantom 2 comprised chicken muscle ~45 mm thick containing in its center the same copper wire, providing 25 mm RF penetration depth, 20 mm RISHA wave travel distance, and 40 mm roundtrip US travel distance in tissue. The photograph shows phantom 2. (**b**) Photograph of phantom 2 when installed in imaging chamber, with the copper wire (Cu) artificially illustrated as a dashed brown rectangle. (**c-e**) RISHA images, and co-registered RISHA/US images with RISHA (red) and US (green) responses of copper wire imaged (**c**) in the absence of any muscle (0 mm), (**d**) in 20 mm thick muscle tissue (phantom 1), and (**e**) in 45 mm thick muscle tissue (phantom 2). Dashed arrows indicate line profiles analyzed in panels f and g. (**f**) RISHA signal profiles of copper imaged without any muscle (0 mm) or in 20 or 45 mm muscle tissue, along the arrows in panels c-e, respectively. (**g**) US echo signal profiles of copper imaged without any muscle (0 mm) or in 20 or 45 mm muscle tissue, along the arrows in panels c-e, respectively.
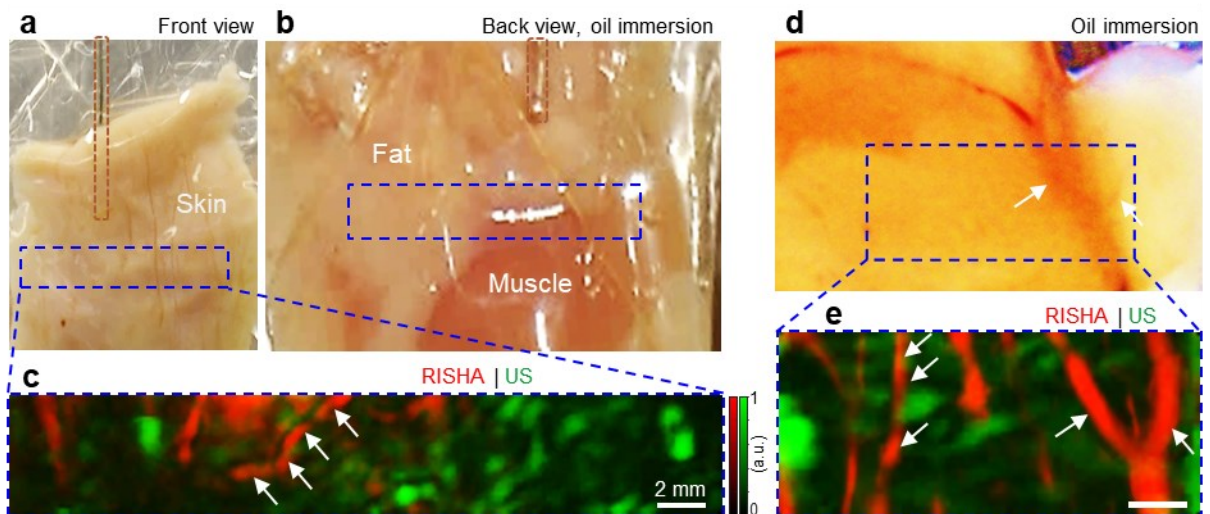
Supplementary Figure S5. RISHA imaging of heterogeneous biological tissue *ex vivo*. (**a-c**) RISHA/US imaging on a sample consisting of chicken dermis tissue approximately 5 mm thick containing skin, fat, muscle, blood capillaries, as well as a copper wire as positioning reference (indicated by dashed brown box). The dermis sample is shown in panel (**a**) front view/transducer view, and (**b**) back view. The sample was immersed in vegetable oil and wrapped in polyethylene film to preserve conductivity/RF absorptivity. The dashed blue box indicates the area scanned. (**c**) Co-registered RISHA/US image of the sample area as indicated in panel a, with RISHA signals rendered in red and US signals rendered in green. White arrows indicate vasculature. (**d-e**) RISHA/US image of a sample of chicken muscle >5 mm thick containing blood vessels (white arrows). The sample was immersed in vegetable oil and wrapped in polyethylene film to preserve conductivity/RF absorptivity. The blue dashed box indicates the area scanned. (**d**) Photograph of the thick muscle sample. (**e**) Co-registered RISHA/US image of the area within the dashed blue box in panel d. Tubular structures likely corresponding to blood vessels (arrows). Scale bars, 2 mm.

References

1   Soliman, D., Tserevelakis, G. J., Omar, M. & Ntziachristos, V. Combining microscopy with mesoscopy using optical and optoacoustic label-free modes. *Sci. Rep.* **5**, 12902; 10.1038/srep12902 (2015).

2   Kellnberger, S., Omar, M., Sergiadis, G. & Ntziachristos, V. Second harmonic acoustic responses induced in matter by quasi continuous radiofrequency fields. *Appl. Phys. Lett.* **103**, 153706 (2013).

3   Razansky, D., Kellnberger, S. & Ntziachristos, V. Near-field radiofrequency thermoacoustic tomography with impulse excitation. *Med. Phys.* **37**, 4602-4607 (2010).

4   Kellnberger, S., Hajiaboli, A., Razansky, D. & Ntziachristos, V. Near-field thermoacoustic tomography of small animals. *Phys. Med. Biol.* **56**, 3433-3444 (2011).

5   Omar, M., Kellnberger, S., Sergiadis, G., Razansky, D. & Ntziachristos, V. Near-field thermoacoustic imaging with transmission line pulsers. *Med. Phys.* **39**, 4460-4466 (2012).

6   Beard, P. Biomedical photoacoustic imaging. *Interface Focus* **1**, 602-631 (2011).

APPLIED SCIENCES AND ENGINEERING

Noninvasive visualization of electrical conductivity in tissues at the micrometer scale

Yuanhui Huang[1,2], Murad Omar[1,2†], Weili Tian[3‡], Hernán Lopez-Schier[3],
Gil Gregor Westmeyer[1,4§], Andriy Chmyrov[1,2], George Sergiadis[1,2,5||], Vasilis Ntziachristos[1,2]*

Despite its importance in regulating cellular or tissue function, electrical conductivity can only be visualized in tissue indirectly as voltage potentials using fluorescent techniques, or directly with radio waves. These either requires invasive procedures like genetic modification or suffers from limited resolution. Here, we introduce radio-frequency thermoacoustic mesoscopy (RThAM) for the noninvasive imaging of conductivity by exploiting the direct absorption of near-field ultrashort radio-frequency pulses to stimulate the emission of broadband ultrasound waves. Detection of ultrasound rather than radio waves enables micrometer-scale resolutions, over several millimeters of tissue depth. We confirm an imaging resolution of <30 μm in phantoms and demonstrate microscopic imaging of conductivity correlating to physical structures in 1- and 512-cell zebrafish embryos, as well as larvae. These results support RThAM as a promising method for high-resolution, label-free assessment of conductivity in tissues.

INTRODUCTION

Distributions of electrical conductivity in cells depend on the concentrations and mobilities of critical charged species (1), such as proteins, nucleic acids, sodium, potassium, and calcium. Many diseases cause imbalances in the cellular distributions of these ions and thus changes in local conductivities (2); examples include allergic diseases (3), cancer (4, 5), diabetes mellitus (6), cardiovascular diseases (7), neuronal dysfunctions (8), and renal abnormalities (9). Therefore, since the invention of patch-clamp techniques (10) by Sakmann and Neher in 1976, and the earlier, voltage-clamp technique (11) by Hodgkin and Huxley in 1952, there have been an explosion of studies elucidating the role of conductivity in tissue physiology, in addition to the electrical behaviors of single ion channel up to a whole cellular network in the nervous system. Patch-clamp is an electrode-based technique that can record electrical signals of isolated cells or tissues (12), but is limited to single-point measurements requiring elaborate skill in order to bring the electrode to close proximity to cellular membranes. Similarly, high-resolution, but superficial, topological conductivity mapping was achieved using micro/nano-pipette–based scanning ion-conductance microscopy (13) and cantilever-based conductive atomic force microscopy (14). The evolution of electrical impedance tomography (15), using surface electrodes, enables noninvasive measurements of in vivo conductivity changes with high temporal resolution but suffers from poor spatial resolution of

centimeters due to the multi-path nature of electric currents. Moreover, whole-brain imaging methods such as magnetoencephalography or magnetocardiography using advanced quantum sensing can detect minuscule magnetic fields induced by the small current changes of, for example, action potentials in neurons but offer poor spatial resolution and require a bulky cryogen-cooled superconducting quantum interference device (16).

To image electrical signals with high resolution, there have been notable developments in the field of optical imaging using fluorescence dyes or genetically engineered proteins that are sensitive to voltage (17) or transient flux of ions (18). These methods are based on electrochromic compounds that reversibly change color by voltage-controlled electrochemical oxidation and reduction (17) or Förster resonance energy transfer (FRET)–based chromophores that couple electronic excitation states of proximate molecules via nonradiative dipole-dipole interactions (17). These techniques have revealed, for example, the receptive map of mouse whiskers (19), the clock and olfactory neurons in model animals (20), <10 ms temporal resolution recordings of single action potential using optical electrophysiology techniques (21), and the possible neurophysiological foundation of gamma rhythm in diseases such as autism and schizophrenia (22). However, fluorescence techniques require invasive measurements to deliver the dyes to the location or require genetic modifications of organisms. Moreover, access to the tissue imaged may also require invasive methods that give access to the depth-limited microscopy method. Recent studies also showed that terahertz (also mid-infrared) spectroscopy can be used to indicate label-free membrane potential change based on vibrational spectra (23) but similarly require invasive procedures because of the very superficial nature of operation, typically reaching depths of only tens of micrometers to a few hundred micrometers. Micrometer-range resolution of conductivity in tissue has also been shown possible using quantum sensing (optical resonance to electric or magnetic field changes) that exploits a crystal defect's spin state, such as nitrogen vacancy in diamond (24) to sense the electrical signals from physiological process. However, such electron spin manipulation when used noninvasively to tissue requires close proximity to the site of the activity (25) and thus have often been conducted in in vitro studies. The imaging depth is also limited by the readout fluorescence light.

[1]Institute for Biological and Medical Imaging (IBMI), Helmholtz Zentrum München, D-85764 Neuherberg, Germany. [2]Chair of Biological Imaging at the Central Institute for Translational Cancer Research (TranslaTUM), School of Medicine, Technical University of Munich, D-81675 Munich, Germany. [3]Research Unit Sensory Biology and Organogenesis, Helmholtz Zentrum München, D-85764 Neuherberg, Germany. [4]Institute of Developmental Genetics (IDG), Helmholtz Zentrum München, D-85764 Neuherberg, Germany. [5]Suzhou Institute of Biomedical Engineering and Technology, Chinese Academy of Sciences, 215163 Suzhou, China.
†Present address: Butterfly Network, Guilford, CT 06437, USA.
‡Present address: Division of Molecular Neurogenetics, German Cancer Research Center (DKFZ), Heidelberg 69120, Germany.
§Present address: Department of Neurobiological Engineering, TUM Department of Chemistry and TUM School of Medicine, Technische Universität München, D-81675 München, Germany.
||Present address: Aristotle University of Thessaloniki, 54124 Thessaloniki, Greece.
*Corresponding author. Email: v.ntziachristos@tum.de

Long-wavelength electromagnetic (EM) radiation, such as microwaves and radio waves, penetrates deep into dielectric materials. Microwave (10^{-3} to 1 m, 300 to 0.3 GHz) imaging provides label-free contrast of the complex electrical conductivity/permittivity of tissue because of dielectric heating and wave reflection of the tissue to the incident irradiation and has been demonstrated for breast cancer imaging (26). The diffraction-limited resolution of microwave imaging is proportional to wavelength (typically >1 mm), while axial resolution was reported to achieve super resolution of 10 μm (27). Electrical conductivity measurements can also be inferred from the water self-diffusion tensor, determined by diffusion tensor magnetic resonance imaging (MRI), at resolutions of a few millimeters (28). However, besides offering indirect measurements of conductivity, MRI requires expensive instrumentation not typically available in the biological laboratory, and further improving the resolution would require excessively strong magnetic fields not readily available.

Here, we researched methodology to offer label-free, noninvasive measurements of electrical conductivity at high resolutions of a few tens of micrometers, reaching several millimeters of depth inside tissue. To achieve such performance, we researched a novel implementation of thermoacoustic imaging (29), by detecting the conductivity-induced absorption of low megahertz range radio frequency (RF; 20 kHz to 300 GHz) in tissue, using ultrasound (US) waves generated in response to this absorption. Mathematical treatment of the arrival of US waves over time, measured in multiple positions on the tissue surface, reconstructs maps of absorption due to electrical conductivity in tissues. The method differs from optoacoustic (photoacoustic) imaging that is based on the absorption of light (30). Several implementations of thermoacoustic imaging have been used for breast cancer imaging (31) at 434 MHz at 1.5-mm resolution, using long RF pulses (>1-μs width), using mixed contrast from free ions and polarized molecules in tissue (32). Resolution >300 μm has also been achieved at microwave frequencies 1.2 to 6 GHz (λ = 25 to 5 cm) (33). Compared to microwave and millimeter-wave excitation, low-frequency RF penetrates deeper into tissue (34) because attenuation (energy drops to $1/e^2$) is much lower at low frequencies than at high frequencies (14.3-cm penetration into muscle at 27.12 MHz versus 1.7 cm at 2.45 GHz).

In this work, we explore the concept of near-field excitation combined with optoacoustic mesoscopy using high-bandwidth US detection. Near-field excitation allows efficient nonradiative excitation of US waves using RF energy to tissue, as opposed to the aforementioned microwave systems (31), whereby a large part of the radiated EM energy is reflected and/or dissipated in space but not in tissue. Efficient coupling enables, in turn, the use of ultrashort RF pulses (10 to 100 ns) for broadband US excitation (32), which give rise to broadband US waves and high-resolution imaging. To develop an imaging method for in vivo imaging, we coupled the concept of near-field RF excitation to raster scan mesoscopic detection enabling high-resolution tomographic imaging. We postulated that 1.5-ns RF pulse excitation coupled with an open transmission line would afford orders of magnitude better resolution than allowed by the meters-long wavelength of the RF pulse itself and allow conductivity imaging with resolutions in the range of a few tens of micrometers. To examine this postulation, we developed a novel raster-scanning radio-frequency thermoacoustic mesoscopy (RThAM) arrangement and imaged copper and suture phantoms to demonstrate the resolution gains. To examine whether in vivo imaging could be performed, we also visualized the free ionic content distribution in small zebrafish embryos of ~1 mm in diameter, revealing rich details of the electrical conductivity based on tomographic images. We further demonstrate the quantitative potential of RThAM in imaging conductivity changes during zebrafish embryonic development and in zebrafish larvae, revealing complex spatial patterns in vivo. Our study showcases the high axial and lateral imaging resolution of conductivity in tissues achievable using RThAM, which could be more generally used for noninvasive, label-free investigations that are complementary to electrode- or fluorescence-based methods.

RESULTS

Principle of RThAM

Figure 1A illustrates a schematic of RThAM (see details in Materials and Methods, fig. S1, and notes S1 and S2). RThAM requires nanosecond pulses and a substantial energy density in the form of an electrical field to generate detectable thermoacoustic signals (30). On the basis of the principle of reactive near-field coupling (35), substantial amounts of pulsed RF energy in nanoseconds could be deposited locally to stimulate sufficient Joule heating in conductive tissue for microscopic thermoacoustic imaging. Accordingly, we engineered an open transmission line (open TxLine; similar to twin leads) that is made of parallel plates. Compared to previous efforts using near-field coupling to generate high-strength thermoacoustic signals (32, 35–37), the open TxLine of RThAM "concentrates" the nanosecond pulsed RF energy homogeneously in the form of an electric field between the plates, like in parallel-plate capacitors (note S1). Exposed to an electric field that is stronger than the Johnson noise-equivalent field strength, a charged ion is accelerated along or against the electric field lines depending on the charge types. The added kinetic energy of the ion dissipates as heat due to collisions with other particles in the medium, causing a temperature rise and the subsequent thermal expansion, thus eventually emanating thermoacoustic waves (dashed red circles in Fig. 1A). The excitation source we used is a commercialized RF pulser built with a drift step recovery diode (FPG 10-10NK1, FID GmbH), delivering a near-Gaussian pulse with a full width at half maximum (FWHM) of 1.5 ns and an excitation frequency up to 300 MHz at −6 dB. To optimally couple the RF energy to tissue, we used silicone oil with a low dielectric constant (ε_r = 2.45 at 20°C; PSF-2cSt, Clearco Products), which avoids field strength decrease because of high permittivity dielectrics like water (ε_r = 80.1 at 20°C). An RF pulse energy of up to 2.91 mJ was thus coupled in the cross-sectional area between the TxLine (note S1), allowing high-strength thermoacoustic signal generation. However, thermoacoustic wave is dissipated severely in silicone oil (note S2). Because water attenuates US waves less than silicone oil (5 dB/mm in silicone oil, against 0.97 dB/mm in water at 50 MHz), we therefore attached a deionized water bag in front of a transducer (central frequency, 50 MHz; 90.66% bandwidth; focus, 6 mm; diameter, 6.35 mm; V3330, Olympus NDT) to couple the thermoacoustic waves. Thermoacoustic signals were amplified at the US transducer using a 63-dB low-noise amplifier (AU-1291, MITEQ) and then digitized by a 500 MSamples/s PCI (peripheral component interconnect) data acquisition card (CompuScope 12502-128M, Gage Applied). Raster scanning was performed by controlling two linear stages to collect two-dimensional (2D) grid data points. The 3D signals were reconstructed into images using a beam-forming algorithm (30). From the reconstructed 3D image, we can analyze either a single slice
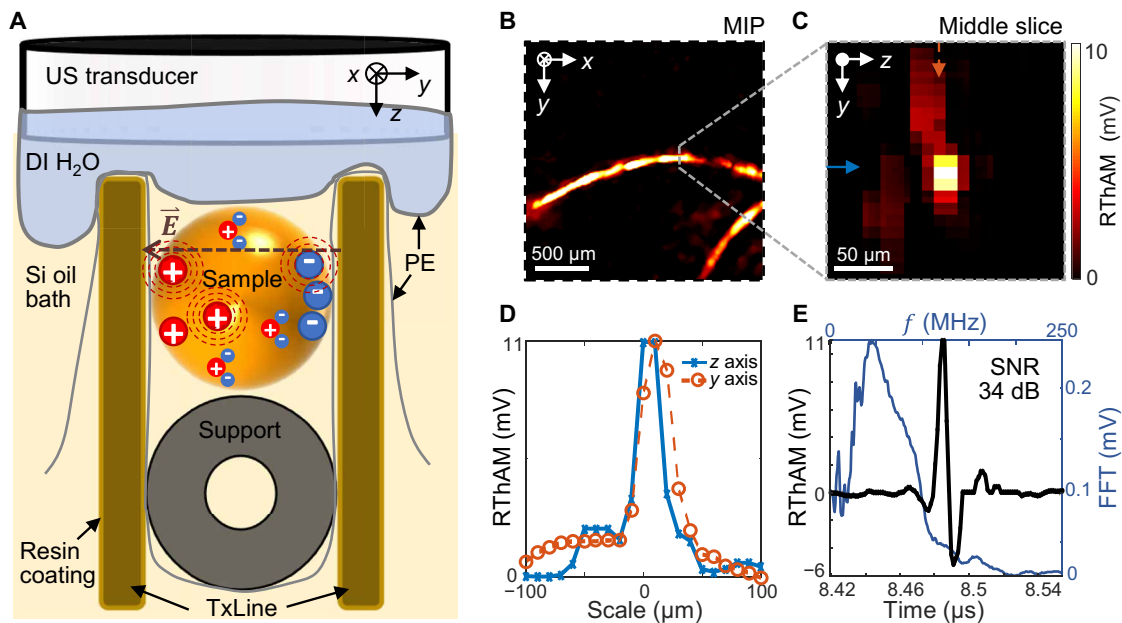
Fig. 1. The principle and performance of RThAM. (**A**) Schematic showing the RThAM imaging principle. We used silicone oil (Si oil) as dielectric medium in an open transmission line (TxLine) and coupled an RF field $[\vec{E}(t)]$ to the biological sample (supported by a tubing of ⌀1 mm) to excite thermoacoustic wave (dashed red circles). The thermoacoustic wave is coupled by deionized water (DI H$_2$O) contained by PE film to an ultrasound (US) transducer. Resin coating to the copper and an extra PE film are applied to avoid direct contact between the sample and TxLine. (**B** and **C**) RThAM image of two copper wires (diameter, 50 µm) formed (B) by MIP in the xy plane and (C) by a slice (indicated by the dotted gray line) in the yz plane. (**D**) Line profiles showing a FWHM of 23 µm in the z axis (axial) and 33 µm in the y axis (lateral) along the solid blue and dashed arrows indicated in (C), respectively. (**E**) A temporal RThAM signal (black curve) showing an SNR of 34 dB and its Fourier transform (FFT; blue curve) showing the frequency components and a central frequency at 47 MHz.

or a maximum intensity projection (MIP) of a stack of the consecutive slices, representative of the conductivity distribution of the sample.

To image conductivity only (excluding permittivity), we chose an excitation frequency below 300 MHz. In this range, dielectric absorption by polar molecules is minimal (*32, 38*), as shown by both theory (*39*) and experiment (*36, 38*). For example, the dielectric-to-conductivity absorption ratio is about 1% at frequencies between 13.67 and 36.335 MHz (<5% up to 300 MHz), corresponding to the current RThAM US detection bandwidth of 27.34 to 72.67 MHz according to the second harmonic generation principle (*36*). We have confirmed the linear relation between electrical conductivity and thermoacoustic responses at low frequencies [low compared to the picosecond relaxation time of polar molecules (*40*)] using blood (*36*) and aqueous NaCl solutions (*36, 38*). RThAM is thus designed to show predominantly contrast from conductivity, especially for tissues with a high ionic content, such as blood, body fluids, cerebellum fluids, gray matter in the brain, retinas, corneas, and the aqueous humor in the eye (*39*).

RThAM imaging performance

To characterize the RThAM setup, we raster-scanned the transducer in 10-µm steps over a 2.2 × 2.2 mm^2 field of view (FOV) with a pair of copper wires (⌀50 µm; electrical conductivity σ = 5.8 × 10^7 S/m) placed in the TxLine made of water as dielectrics (note S2). Figure 1B shows the resulting thermoacoustic mesoscopic image that was formed by an MIP along the depth/z axis (see Materials and Methods for signal processing and image formation). Figure 1C shows a cross-sectional image in the yz plane, and Fig. 1D shows the profiles of the copper wire in the lateral and axial directions. Inspection

of the copper wire profiles reveals an FWHM of 23 µm in the z direction (axial) and 33 µm in the xy plane (lateral). The apparent axial FWHM is a result of the 13-µm skin depth (at which depth the RF field strength decreases to 1/e and the energy to 1/e^2) of the 25-MHz RF field in copper (fig. S1G, and note S3), while the apparent lateral FWHM is a result of the cylindrical shape of the copper wire and the limited acceptance angle of the US transducer. Figure 1E shows a temporal sequence of the maximum RThAM amplitude. A 34-dB signal-to-noise ratio (SNR) was achieved due to both the excellent RF energy coupling to the sample and the high electrical conductivity/RF absorption of copper, which affords high sensitivity and a broad dynamic range for conductivity measurements. Fourier analysis (blue line) shows that the signal contains frequency components centered at ~50 MHz, extending to 100 MHz, which reflects the detection bandwidth of the transducer. Because of the second harmonic generation of the thermoacoustic signal (*36*), the induced RThAM wave oscillates at the second harmonic of the excitation RF. Therefore, the detected 50-MHz RThAM signal corresponds to the absorption of RF at 25 MHz, with a wavelength of 12 m. The achieved RThAM resolution is about 0.5 × 10^6 times shorter than the excitation wavelength. Even though the super-resolution ratio remains the same, the resolution is scalable to microscopic regime by applying higher frequencies of excitation and detection, e.g., using 100-MHz US detection and the same phantom we managed to image 7 and 16 µm in axial and lateral resolution, respectively (fig. S2 and note S4). Note that a long oil path in the hybrid oil/water coupling medium of RThAM could deteriorate the acoustic resolution (fig. S3, A and B and note S5). To minimize this deterioration, we used the sample bed to position the sample close to the water bag

so that the oil path was less than 1 mm. Because RThAM resolution is acoustically limited, similar to conventional optoacoustic mesoscopy (*30*, *41*), the polarization of the excitation field does not change the resolution, but higher contrast can result from longitudinal objects that are aligned with field polarization compared to those that are perpendicular to the field (fig. S3, C to E, and note S6).

Imaging single-cell stage embryos

To test our hypothesis that RF absorption could be exploited to resolve microscale spatial variation of electrical conductivity, we imaged zebrafish (*Danio rerio*) embryos using our hybrid oil/water coupling RThAM system. The single-cell embryo offers a simple anatomical structure with marked conductivity differences (*42*); since the egg yolk consists primarily of lipids, the egg cell comprises a blastodisc where genetic materials are contained and duplicated and the albumen area containing proteins for development. We chose this compartmental structure as an imaging model to evaluate the RThAM ability to resolve conductivity contrast in vivo. Another advantageous feature of this imaging model is that the embryo is a self-contained system protected by chorion, uncontaminated by extrinsic ions. Figure 2A shows an optical bright-field microscopic image of a one-cell stage (zygote period) zebrafish embryo at $^1/_2$ hour post-fertilization (hpf). The localized blastodisc in the animal pole and a large yolk are clearly visible. For subsequent RThAM imaging, the egg cell was immersed in silicone oil intact (Fig. 1A). Figure 2B shows the RThAM image of the embryo formed by MIP and Fig. 2C shows an overlay of the RThAM image on the bright-field microscopic photo. Movie S1 shows the 3D distribution of RThAM contrast of the embryo. Visually, the brightest region in the RThAM image corresponds to the developing blastodisc. Strong RThAM response suggests enhanced RF absorption, high electrical conductivity, and therefore high ion concentration in the developing cell region. We show in Fig. 2D a profile across the blastodisc and yolk. The RThAM signal from the blastodisc area was found to be on average five times higher than from the yolk area. We would expect the blastodisc-to-yolk signal ratio to be even higher. However, there is a background signal (~20 mV in Fig. 2D), which might be a result of an ionic content in the surrounding albumen of the embryo (movie S1). Besides the apparently rich contrast, we also noticed some fine features of size <38 μm in the yolk region. They might be a result of the propagation of duct-type structures or angiogenesis originated from the animal pole that is developing into the embryonic fish body. Further studies are needed to confirm correlations between the RThAM images and known fine structures of within a zebrafish egg.

Multicellular stage structures

To visualize more of these fine and complex multicellular structures in three dimensions, we imaged an embryo in a later developmental stage with RThAM (512 cells). An embryo at the 512-cell stage is interesting for 3D imaging because finer structures form as the mid-blastula transition starts (*42*)—the deep cells in between the yolk syncytial layer and the outermost enveloping cells split asynchronously, becoming motile and streaming over the yolk toward periphery. Figure 2E shows a bright-field microscope image of the zebrafish embryo 4 hpf, in which the blastomeres were at the 512-cell stage. We would again expect a stronger signal from the more ion-rich region containing the blastomeres. Figure 2 (F and G) shows the RThAM MIP image of the embryo and the corresponding overlay

with the bright-field image. Movie S2 showed the 3D distribution of the RThAM contrast. While it appears that there are strong signals from both the blastomere and yolk regions, a cross-sectional image in the *xz* plane (Fig. 2H and movie S2) indicates that the apparent signals from the yolk actually originate from the embryo surface. This again supports the idea that the yolk consists of mostly non-RF absorbing material (primarily lipids). The distribution of RThAM signals in 3D that were surrounding the yolk probably reflected the spread of cells from animal pole in the developing embryo. It is further apparent from Fig. 2H that the most intense signals emanate from the area corresponding to the blastodisc center, where there is a high density of splitting deep cells. Figure S4 (A and B) shows a 200-μm slice of the RThAM image in the *xy* plane at the depth of the blastomeres' center and an overlay of this slice on the bright-field image. Within this image slice, a maximum SNR of 29 dB (fig. S4C) and features as small as 45 μm (fig. S4D) were recorded.

Contrast in zebrafish larvae

We further probed the limits of RThAM by imaging zebrafish larvae at more advanced stages [<5 days post-fertilization (dpf)], at which larvae contain discrete internal organs. Furthermore, the optical transparency of zebrafish larvae at this stage facilitates the comparison of RThAM and optical contrast. We expected to see regions with high ionic content (*43*), and thus high electrical conductivity compared to the background tissues, such as muscle (0.65 S/m at 25 MHz) or fat (0.06 S/m). Examples of these regions are blood (1.15 S/m) in the circulatory system, intestines (1.47 S/m) in the digestive system, urine (1.75 S/m) in the bladder, vitreous (1.50 S/m) and aqueous humor (2.01 S/m) in the eyes, or cerebrospinal fluid (2.01 S/m) in the brain (0.22 to 0.55 S/m). Figure 2I shows a transparent Casper-type zebrafish larva at 3 dpf in low-power optical reflection-mode microscopy, in which most internal organs and tissues of interested are clearly visible. Figure 2J shows a 150-μm-thick RThAM *xy* slice at the depth of the spinal cord, overlaid on a negative image of the optical contrast. Figure 2K shows the contrast distributions along depths obtained by projecting the 3D data cube in the *x* direction and forming a B-scan–like *yz* MIP image. High-RF energy absorption can be observed in areas that correlate with the eyes, blood/heart, forebrain/midbrain, and ventral areas containing the intestines, bladder, and pancreas. We also note some discernable RThAM contrast from the trunk, which emanates from muscle or dorsal/ventral blood vessels. We observed little contrast in the yolk sac region, which was expected because the yolk mainly consists of hydrophobic lipids. Similar contrasts were observed from 4-dpf wild-type larvae in both the sagittal (fig. S5, A to C) and the coronal positions (fig. S5, D to F, and movie S3). However, a precise delineation of the RThAM contrasts in terms of the optical contrast was not possible.

DISCUSSION

The direct, noninvasive observation of electrical conductivity in a biological system with microscale resolution was an unmet technical challenge. We introduced herein RThAM, which employs ultrashort RF pulses and an open transmission line for near-field energy coupling, to record higher-resolution images of conductive materials versus previous thermoacoustic systems. We challenged the limits of this system by imaging zebrafish eggs and larvae and observed correlations between microscale biological structures with high
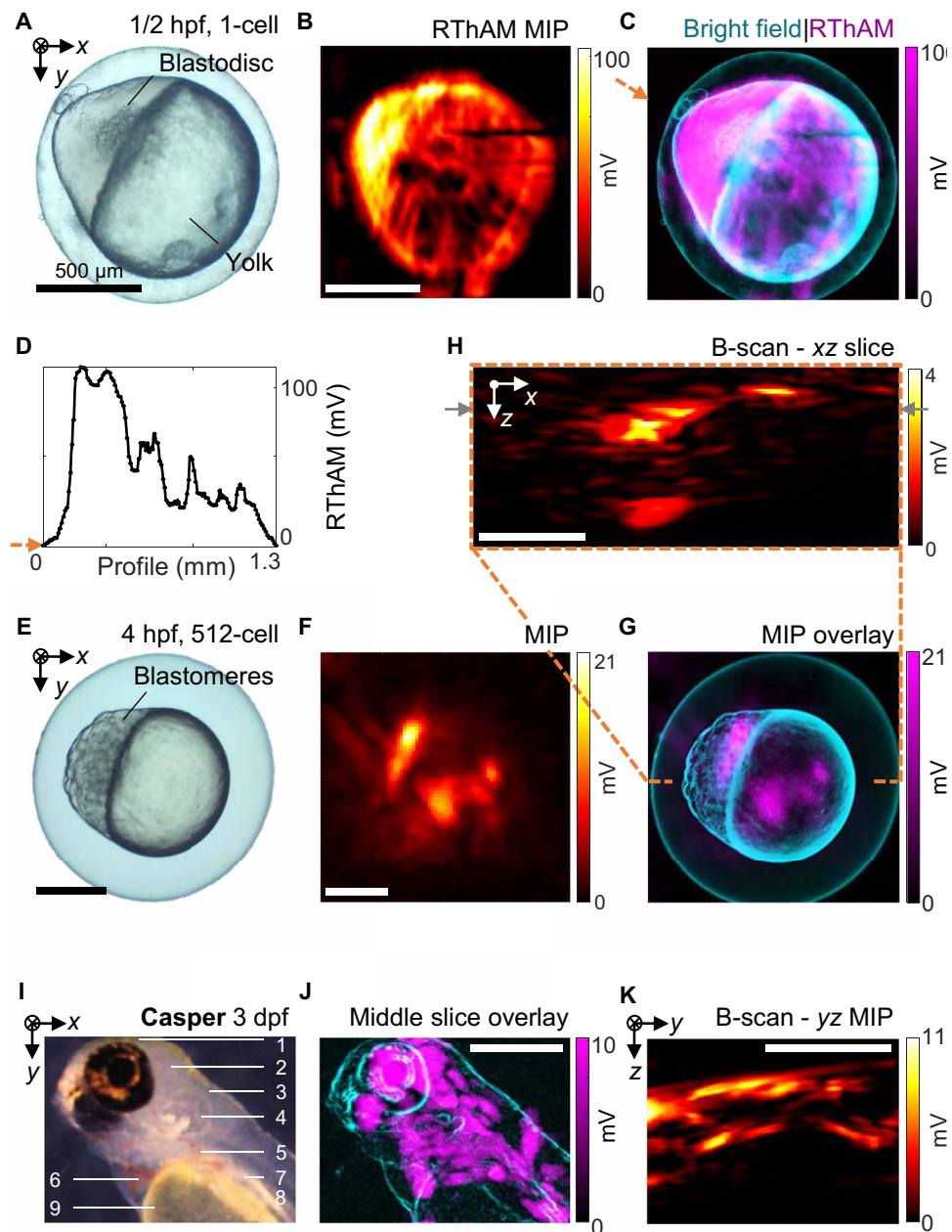
Fig. 2. RThAM imaging of developmental zebrafish embryos and larvae. (**A** to **D**) Imaging of a one-cell stage embryo ($1/2$ hpf). (A) Bright-field microphotograph. (B) RThAM MIP image. (C) An overlay of RThAM MIP onto the microphotograph. (D) The profile along the arrow in (C) showing dominant RF absorption in the blastodisc versus the yolk. (**E** to **H**) Imaging of a 512-cell stage embryo (4 hpf). (E) Bright field. (F) RThAM MIP. (G) Overlay. (H) An *xz*-plane B-scan along the dashed orange line in (G), showing intense absorption from the blastomere region and the absorption originated from the surface of the embryo. The gray arrows indicate the B-scan analyzed in fig. S4. (**I** to **K**) Imaging of a transparent Casper zebrafish larva at 3 dpf. (I) Optical reflection-mode microphotograph of the larva in the coronal view with annotation of major anatomical features: (1) forebrain; (2) midbrain; (3) hindbrain; (4) inner ear; (5) liver, intestine, and pancreas; (6) heart; (7) swim bladder; (8) spinal cord and vessels/muscles in the trunk; and (9) yolk sac. (J) An overlay of an RThAM slice (~150 μm in thickness) onto the microphotograph (edge-filtered). (K) MIP in the *yz* plane. Scale bars, 500 μm.

expected ionic content and RThAM contrast. These are the highest-resolution thermoacoustic images of biological samples to date.

By applying ultrashort RF pulses (1.5 ns) and an open transmission line design, we determined the upper limit of RThAM's resolution to be ~30 μm using a 50-MHz transducer (Fig. 1), and scaled up to 7 μm using a 100-MHz transducer (fig. S2 and note S4), both of

which are approximately 500,000 times smaller than the excitation wavelength. RThAM resolution is thus only limited acoustically, similar to conventional optoacoustic mesoscopy (*30*, *41*), and the polarization of the excitation field does not change the resolution. However, it is worth noting that the polarized field affords a stronger contrast from objects that are parallel, rather than perpendicular, to the field

polarization (fig. S3 and notes S5 and S6). Previous thermoacoustic systems that used similar near-field energy coupling and short RF pulses have only demonstrated in copper wire phantom resolutions (32) of up to 40 μm or separation (44) of up to 105 μm. Similarly, magnetic field–mediated thermoacoustic imaging has demonstrated a 185-μm separation between aluminum sheets (45). Using a magnetic field to induce eddy currents in conductive matter could potentially provide a similar resolution for conductivity imaging at greater penetration depths than other thermoacoustic methods (46, 47). Microwave-based thermoacoustic systems that used amplitude modulation (31) have demonstrated resolutions of about 300 μm, but the resolution was limited by modulation width and irrespective of the radiation wavelength. The improved resolution demonstrated by RThAM increases the relevance of thermoacoustic imaging for biological applications.

RThAM demonstrated the ability to resolve ionic content in small model organisms with unprecedented microscale resolution. We demonstrated this contrast in zebrafish embryos indicating conductivity distributions as small as 30 to 45 μm in 3D (Fig. 2, A to H, fig. S4, and movies S1 and S2). The strong 3D RThAM responses come primarily from the blastodisc/blastomere area in embryos, where the genetic materials are primarily concentrated in a cell before division. Conversely, the lipid-rich yolk shows low RThAM contrast, likely because of its hydrophobic contents. We also coregistered RThAM images of zebrafish larva with corresponding optical and US images (Fig. 2, I to K, fig. S5, and movie S3). Again, RThAM contrast was observed to correlate strongly with organs with high expected conductivity, such as the eyes, brains, cardiovascular systems, and organs in the ventral region. Furthermore, the yolk sac of the larva showed little contrast, analogous to our observations in the embryos. Our observations confirmed a previous study of in vitro tissue electrical properties (43) and extended the range of intrinsic contrast sources available for RF-induced thermoacoustic imaging (32, 36). Compared to previous microwave-induced thermoacoustics, which visualize both the electrical conductivity and permittivity (48), RThAM is less sensitive to the polar molecules like water because the frequency (300 MHz) used is too low to induce measurable dielectric heating via electric dipole relaxation (40).

It is worth noting that the ultrashort RF field pulse also serves as an impulse source to remotely excite in transducer ultra-wideband US emissions via the inverse piezoelectric effect, making RThAM passively built-in with an auto-coregistered high-frequency US microscopy (see Materials and Methods, and US features like spinal cord shown in fig. S5E, green channel; see also movies S1 to S3). Compared to the passive US imaging previously described in a low-megahertz RF (36) thermoacoustic imager (resolution ~0.5 mm), or in the microwave (33, 48)–induced counterparts (resolution >1 mm due to long excitation pulse width), RThAM offers a passive US imaging resolution in theory limited only by the employed transducer bandwidth, similar to raster-scan optoacoustic mesoscopy (30). Perhaps this aspect of RThAM could be exploited to achieve not only multimodal imaging but also multiphysical stimulations for active measurements.

RThAM might offer a new perspective for observing life phenomena by a direct observation on the ionic content in tissue that plays as both a regulator and an indicator in critical physiological processes (3, 6, 8, 9). For applications such as imaging large changes in blood/fluid distribution, RThAM scanning speeds need to be improved, for example, by using continuous scanning and data streaming (30, 41),

a transducer array to obtain B-scan images at each excitation (49), or ergodic relay acoustic detection (50) for snapshot imaging in lateral plane. Beyond biological imaging, high-resolution RThAM may find applications in characterization of semiconductor doping profiles (51). However, such applications would be predicated on a more fundamental understanding of the contrast mechanisms. Further research would be required to establish precise knowledge on microscopic electrical conductivity distribution in small organisms. In the current state, RThAM is also limited in FOV because of the fixed dielectric gap size in impedance-matched transmission lines. Specifically, the dielectric used, silicone oil for RF coupling purposes, limits RThAM application for in vivo studies. Innovative RF coupling methods using water as a dielectric would be highly desirable to enable higher-resolution and in vivo studies. The image quality of future iterations of RThAM could potentially be improved by introducing detection and signal processing techniques that were developed for optoacoustic mesoscopy (30), by using an RF excitation source that matches the frequency range to the detection bandwidth (e.g., 10 ns pulser for RThAM 100 MHz), or by using elements with a higher coupling efficiency using water as couplant for RF and US (table S1 and notes S1 and S2).

In conclusion, we demonstrated the ability of RThAM to noninvasively visualize microscale biological structures by exploiting electrical conductivity as contrast. This technology could potentially motivate research into applications, for which direct electrical conductivity readouts could be of use, like angiogenesis of tumors for early-stage detection, ablation monitoring of cancerous tissue, diagnosis of renal abnormalities diagnosis and neuronal dysfunctions, as well as semiconductor doping profiling or printed circuit board inspection.

MATERIALS AND METHODS
Setup
As shown in fig. S1A, an RF pulser (FPG 10-10NK1, FID GmbH) generates 5- to 10-kV pulses of 1.5 ns at 1 to 10^4 Hz pulse repetition rate (PRR). We used a flexible 50-ohm coaxial cable (RG213/U, Pasternack Enterprises) to deliver the energy. To prevent system damage in case of impedance mismatching, we inserted a custom-built 1.5-dB T-pad passive attenuator of 50-ohm impedance before feeding the RF pulse into the energy coupling element. The energy coupling element is an open TxLine by design. Custom-built 50-ohm termination consists of 4-by-4 RF power resistors (CHF3725CNP, Bourns). To optimize the electric field strength in the TxLine (notes S1 and S2), we used light silicone oil [PSF-2CSt Silicone Fluid, Clearco Products; specific gravity 873 kg/m^3; speed of sound (SoS), 931 m/s] as dielectric, which exhibits dielectric breakdown strength ≥14 kV/mm, viscosity 2 cSt at 25°C, and dielectric constant $\varepsilon_r = 2.45$. To maximize RF energy coupling, the open TxLine was built with 1-mm dielectric height and 3-mm conductor width from a 0.3-mm-thick copper sheet (Fig. 1A), to have a 50-ohm characteristic impedance matching the pulse source and the termination load (fig. S1C). As a result, a pulsed RF energy of 2.91 mJ was coupled through a cross section of 1×3 mm^2 of TxLine (note S1). As shown in Fig. 1A, to prevent direct contact between the samples and TxLines, we first sprayed a thin layer of resin (Plastik 70, Kontakt Chemie) on the surface of the copper conductors and then placed a 20-μm-thick polyethylene (PE) film between sample and copper conductors. Biological samples were supported by a PE tubing of 1-mm outer diameter. The sample and TxLine were immersed in silicone oil.

We used a USB microscope (DigiMicro Profi, DNT) to help with sample installation and positioning. To ensure good acoustic coupling, we used the abovementioned PE film to contain deionized water (5.5×10^{-6} S/m) so as to couple RThAM/US waves in the detection path of the transducer (see coupling mode comparison in table S1). We assumed that the deionized water and tubing above/in the open TxLine and the applied resin and contact-avoiding film do not substantially change the electric field in the TxLine. Within the deionized water bag, we placed a spherically focused piezoelectric transducer (V3330, Olympus-NDT; central frequency, 50 MHz; 90.66% bandwidth; focus, 6 mm; diameter, 6.35 mm). To enable raster scan in 3D space, we mounted the transducer to xy translation stages (M-683.2U4 and M-404.2PD, Physik Instrumente) and mounted the imaging chamber containing the open TxLine, dielectrics, and samples to a z stage (M-404.2PD). The scanning step is 5 to 25 μm in general. We used a 63-dB amplifier (AU-1291, MITEQ) to amplify signals detected by the US transducer and a data acquisition card (CompuScope 12502-128M, Gage-Applied; sampling rate, 500 MS/s; 1024 hardware averages) to digitize the signals. Digitized data were stored in a personal computer, which was also used for synchronizing raster scanning and reconstructing the images in Matlab. A typical raster scan in RThAM mode takes 20 min for a FOV of 1.5×1.5 mm^2 using 10-μm steps.

We designed an open TxLine of 25-ohm characteristic impedance for characterization experiments using the copper wire samples (Fig. 1, fig. S2, and note S2). Biological tissues, because of their low conductivity (typically a few S/m) and low RThAM signal generation using our chosen RF pulser, require silicone oil and water bag to couple the RThAM signals, but copper generates high thermoacoustic (32) signals because of its high conductivity $\sigma = 5.8 \times 10^7$ S/m. So, in the attempt to use water as dielectric, we used a deionized water–filled open TxLine to couple the RF energy and the US/RThAM waves. The 25-ohm open TxLine is constructed with copper sheet as a conductor with a dielectric gap of 6 mm and a conductor width of 3.5 mm. The TxLine is matched to the 50-ohm source, by inserting before it a 25-ohm resistor in series and terminating it with a 25-ohm load. This 6-mm-gap open TxLine uses water as a dielectric medium and has more operational space for sample handling, but it delivers 72 times less energy flux than the 1-mm oil gap TxLine used for this work, and 1069 times less RF intensity (difference between RF energy attenuation of pure water and pure oil, 30.29 dB) because of the polarization field of water molecule (notes S1 and S2 and table S1) and therefore is not suitable for biological tissue experiments.

Signal processing and image formation

After acquiring the RThAM signals using Matlab, we apply wavelet-based denoising, band-pass filtering corresponding to the −12-dB bandwidth of the transducer, and spatial high-pass filtering to eliminate noise and signals out of the detection bandwidth. To the resulting dataset, we apply 3D median filter to ensure smoothness. We selected a uniform SoS just below that of water, whereby the highest resolution and contrast reconstruction is obtained. For higher image quality and more precise quantitative measurements, the acoustic velocity mismatch will have to be taken into account in a priori reconstructions using SoS and structural information (note S5) (52–54). RThAM images are reconstructed based on filtered back projection algorithm and showed using MIP of the reconstructed signals. If a middle slice is required instead of a MIP of the whole stack, either a single slice or the MIP of a few consecutive adjacent slices at the

desired depth was used. In the resulting image, we subtract the smallest pixel value from all pixels to generate a dark background for better visualization. For the images shown, we saturated 0.4% of the pixels to have a dynamic range fit for our screen display. With the 3D volumetric data, we used ImageJ to generate movies S1 to S3 to demonstrate the 3D distribution of RThAM contrast. The SNR calculation of a given temporal sequence is based on the square of integrated signal points and the square of standard deviation of the noise data points.

Pulse-echo ultrasonography

The US emission, from the same transducer as used by RThAM, was induced via inverse piezoelectric effect caused by RF interference (36). The echo US was detected in the same temporal sequence but at a time point approximately twice that of the RThAM signal because of the round trip propagation of active US (36). Therefore, the US-MIP is innately coregistered with RThAM-MIP, pixel by pixel. We used this pulse-echo US image to coregister the optical and RThAM image here. However, to make the best out of US imaging, we used the transducer in active US mode to exploit its inverse piezoelectric effect by active pulsing using a function generator (DG4162, Rigol Technologies; fig. S1A), instead of the passive US emission because of fringe EM energy coupling to the transducer. Therefore, a function generator was used to send pulses to the transducer. To multiplex the usage of detection chain and amplifier, a bypass circuit composed of two back-to-back Schottky diodes was inserted between a transducer and an amplifier to prevent overload of the amplifier in transmission mode. The active US imaging mode is also raster-scanned, which takes about 3 min for a FOV of 1.5×1.5 mm^2, if given 50-kHz PRR.

Sample preparation

Copper wire phantoms used for RThAM characterization experiments consisted of copper enameled wire of 50-μm diameter. The first step was to remove the insulating layer by heating. Then, two segments of copper wires were knotted at the cross. Before placing the copper phantom into the imaging chamber of the 25-ohm open TxLine, we sprayed a layer of insulating resin (Plastik 70, Kontakt Chemie) onto the sample bed to fix the position of the copper phantom. For the experiment in fig. S3 (C to E), a coil of copper wire (∅100 μm) was wrapped around a tubing (∅600 μm) to show the polarization effect of the electric field depending on the orientation of the wire.

Suture (polyamide ∅50 μm, 1647 ETHILON Nylon Suture) shown in fig. S3 (A and B) was wrapped around a tubing (∅800 μm) to show the in-plane resolution in hybrid oil/water coupling RThAM. The suture phantom was soaked in 10% w/v NaCl solution [1.71 M, ~28.86 S/m according to Widodo et al. (55)] for 2 hours and placed wet in an open transmission line.

Zebrafish embryos of 0.5 and 4 hpf from the wild-type zebrafish were imaged to show cellular RF absorption (Fig. 2, A to H, and fig. S4). The embryos were photographed with a benchtop bright-field microscope before installation in the imaging chamber. The bright-field microphotograph was used later as reference to validate the RThAM image contrast. Before placing the embryo into the imaging chamber, we inserted a PE film to guarantee noncontact between the embryo and the conductors, despite the resin layer. To fix the position of embryos, we applied the abovementioned resin on the surface of the support tubing, before placing the sample. Two

minutes after the embryos were placed, we filled the imaging chamber with silicone oil. Given the water layer on the egg, the embryos continued to develop after the installation.

Zebrafish larvae of 3 and 4 dpf were imaged to show endogenous RF absorption at the organ level. We took 3-dpf Casper zebrafish larvae for RThAM imaging in sagittal view (Fig. 2, I to K). First, the larva was photographed in a bright-field benchtop microscope for referencing purposes, to validate the contrast from RTAM imaging. Then, after the PE film and resin were applied to prevent direct contact, we anesthetized the larva and placed the zebrafish in sagittal position, which were confirmed by a desktop USB microscope. Two minutes after the sample placement, we filled in the TxLine with silicone oil and placed the oil tank on a z-axis motorized stage for RThAM imaging. The same procedure was performed to prepare a 4-dpf wild-type zebrafish larva in the sagittal and coronal position as shown in fig. S5, in which the optical photos were taken by the desktop USB microscope to confirm the position before and after RThAM.

RF field distribution in open transmission line

The EM simulations to examine the electric field distribution in our TxLines (fig. S1, D and E) were performed using a 3D EM simulation tool (CST Studio Suite, Student Edition). The geometric dimensions and dielectrics of the open TxLines are the same as designed (silicone oil dielectric constant, 2.45; dielectric height/gap, 1 mm; conductor thickness, 0.3 mm; width, 3 mm; length, 100 mm; 50-ohm RF input port; and RF load). The copper conductors were set to be perfect electric conductors. To compare the difference in electric field distribution with and without a phantom, a water-content phantom (spherical egg, $\varepsilon_r = 80.1$; $\sigma = 1$ S/m) was inserted. The boundaries were set to be open in all directions.

SUPPLEMENTARY MATERIALS

Supplementary material for this article is available at http://advances.sciencemag.org/cgi/content/full/7/20/eabd1505/DC1

View/request a protocol for this paper from Bio-protocol.

REFERENCES AND NOTES

1. M. Dressel, M. Scheffler, Verifying the Drude response. *Ann. Phys.* **15**, 535–544 (2006).
2. P. Grasland-Mongrain, C. Lafon, Review on biomedical techniques for imaging electrical impedance. *IRBM* **39**, 243–250 (2018).
3. J. Matthias, J. Maul, R. Noster, H. Meinl, Y.-Y. Chao, H. Gerstenberg, F. Jeschke, G. Gasparoni, A. Welle, J. Walter, K. Nordström, K. Eberhardt, D. Renisch, S. Donakonda, P. Knolle, S. Soll, S. Grabbe, N. Garzorz-Stark, K. Eyerich, T. Biedermann, D. Baumjohann, C. E. Zielinski, Sodium chloride is an ionic checkpoint for human T_H2 cells and shapes the atopic skin microenvironment. *Sci. Transl. Med.* **11**, eaau0683 (2019).
4. D. Haemmerich, S. T. Staelin, J. Z. Tsai, S. Tungjitkusolmun, D. M. Mahvi, J. G. Webster, In vivo electrical conductivity of hepatic tumours. *Physiol. Meas.* **24**, 251–260 (2003).
5. V. D. Schepkin, F. C. Bejarano, T. Morgan, S. Gower-Winter, M. Ozambela Jr., C. W. Levenson, In vivo magnetic resonance imaging of sodium and diffusion in rat glioma at 21.1 T. *Magn. Reson. Med.* **67**, 1159–1166 (2012).
6. D. M. Gordon, S. R. Ash, Lack of correlation of glucose levels in filtered blood plasma to density and conductivity measurements. *ASAIO J.* **55**, 227–230 (2009).
7. M. Schaefer, W. Gross, J. Ackemann, M. M. Gebhard, The complex dielectric spectrum of heart tissue during ischemia. *Bioelectrochemistry* **58**, 171–180 (2002).
8. T. J. Jentsch, C. A. Hubner, J. C. Fuhrmann, Ion channels: Function unravelled by dysfunction. *Nat. Cell Biol.* **6**, 1039–1047 (2004).
9. F. Manoni, L. Fornasiero, M. Ercolin, A. Tinello, M. Ferrian, S. Valverde, G. Gessoni, Laboratory diagnosis of renal failure: Urine conductivity and tubular function. *Minerva Urol. Nefrol.* **61**, 17–20 (2009).
10. E. Neher, B. Sakmann, Single-channel currents recorded from membrane of denervated frog muscle fibres. *Nature* **260**, 799–802 (1976).
11. A. L. Hodgkin, A. F. Huxley, Propagation of electrical signals along giant nerve fibres. *Proc. R. Soc. Lond B* **140**, 177–183 (1952).
12. J. Abbott, T. Ye, K. Krenek, R. S. Gertner, S. Ban, Y. Kim, L. Qin, W. Wu, H. Park, D. Ham, A nanoelectrode array for obtaining intracellular recordings from thousands of connected neurons. *Nat. Biomed. Eng.* **4**, 232–241 (2019).
13. P. K. Hansma, B. Drake, O. Marti, S. A. Gould, C. B. Prater, The scanning ion-conductance microscope. *Science* **243**, 641–643 (1989).
14. X. D. Cui, A. Primak, X. Zarate, J. Tomfohr, O. F. Sankey, A. L. Moore, T. A. Moore, D. Gust, G. Harris, S. M. Lindsay, Reproducible measurement of single-molecule conductivity. *Science* **294**, 571–574 (2001).
15. R. H. Bayford, Bioimpedance tomography (electrical impedance tomography). *Annu. Rev. Biomed. Eng.* **8**, 63–91 (2006).
16. E. Boto, N. Holmes, J. Leggett, G. Roberts, V. Shah, S. S. Meyer, L. D. Muñoz, K. J. Mullinger, T. M. Tierney, S. Bestmann, G. R. Barnes, R. Bowtell, M. J. Brookes, Moving magnetoencephalography towards real-world applications with a wearable system. *Nature* **555**, 657–661 (2018).
17. N. Vogt, Voltage sensors: Challenging, but with potential. *Nat. Methods* **12**, 921–924 (2015).
18. E. S. Boyden, F. Zhang, E. Bamberg, G. Nagel, K. Deisseroth, Millisecond-timescale, genetically targeted optical control of neural activity. *Nat. Neurosci.* **8**, 1263–1268 (2005).
19. W. Akemann, H. Mutoh, A. Perron, J. Rossier, T. Knöpfel, Imaging brain electric signals with genetically targeted voltage-sensitive fluorescent proteins. *Nat. Methods* **7**, 643–649 (2010).
20. G. Cao, J. Platisa, V. A. Pieribone, D. Raccuglia, M. Kunst, M. N. Nitabach, Genetically targeted optical electrophysiology in intact neural circuits. *Cell* **154**, 904–913 (2013).
21. Y. Gong, M. J. Wagner, J. Zhong Li, M. J. Schnitzer, Imaging neural spiking in brain tissue using FRET-opsin protein voltage sensors. *Nat. Commun.* **5**, 3674 (2014).
22. V. S. Sohal, F. Zhang, O. Yizhar, K. Deisseroth, Parvalbumin neurons and gamma rhythms enhance cortical circuit performance. *Nature* **459**, 698–702 (2009).
23. H. J. Lee, D. Zhang, Y. Jiang, X. Wu, P.-Y. Shih, C.-S. Liao, B. Bungart, X.-M. Xu, R. Drenan, E. Bartlett, J.-X. Cheng, Label-free vibrational spectroscopic imaging of neuronal membrane potential. *J. Phys. Chem. Lett.* **8**, 1932–1936 (2017).
24. R. Schirhagl, K. Chang, M. Loretz, C. L. Degen, Nitrogen-vacancy centers in diamond: Nanoscale sensors for physics and biology. *Annu. Rev. Phys. Chem.* **65**, 83–105 (2014).
25. C.-C. Fu, H.-Y. Lee, K. Chen, T.-S. Lim, H.-Y. Wu, P.-K. Lin, P.-K. Wei, P.-H. Tsao, H.-C. Chang, W. Fann, Characterization and application of single fluorescent nanodiamonds as cellular biomarkers. *Proc. Natl. Acad. Sci. U.S.A.* **104**, 727–732 (2007).
26. N. K. Nikolova, Microwave imaging for breast cancer. *IEEE Microw. Mag.* **12**, 78–94 (2011).
27. P. Wang, Z. Li, P. Liu, Y. Pei, Super resolution in depth for microwave imaging. *Appl. Phys. Lett.* **115**, 044101 (2019).
28. T. Voigt, U. Katscher, O. Doessel, Quantitative conductivity and permittivity imaging of the human brain using electric properties tomography. *Magn. Reson. Med.* **66**, 456–466 (2011).
29. T. Bowen, Radiation-induced thermoacoustic soft tissue imaging, in *Proceedings of the 1981 Ultrasonics Symposium*, Chicago, IL, USA, 14 to 16 October 1981.
30. M. Omar, J. Aguirre, V. Ntziachristos, Optoacoustic mesoscopy for biomedicine. *Nat. Biomed. Eng.* **3**, 354–370 (2019).
31. R. A. Kruger, K. D. Miller, H. E. Reynolds, W. L. Kiser Jr., D. R. Reinecke, G. A. Kruger, Breast cancer in vivo: Contrast enhancement with thermoacoustic CT at 434 MHz-feasibility study. *Radiology* **216**, 279–283 (2000).
32. M. Omar, S. Kellnberger, G. Sergiadis, D. Razansky, V. Ntziachristos, Near-field thermoacoustic imaging with transmission line pulsers. *Med. Phys.* **39**, 4460–4466 (2012).
33. L. Nie, D. Xing, Q. Zhou, D. Yang, H. Guo, Microwave-induced thermoacoustic scanning CT for high-contrast and noninvasive breast cancer imaging. *Med. Phys.* **35**, 4026–4032 (2008).
34. C. C. Johnson, A. W. Guy, Nonionizing electromagnetic wave effects in biological materials and systems. *Proc. IEEE* **60**, 692–718 (1972).
35. D. Razansky, S. Kellnberger, V. Ntziachristos, Near-field radiofrequency thermoacoustic tomography with impulse excitation. *Med. Phys.* **37**, 4602–4607 (2010).
36. Y. Huang, S. Kellnberger, G. Sergiadis, V. Ntziachristos, Blood vessel imaging using radiofrequency-induced second harmonic acoustic response. *Sci. Rep.* **8**, 15522 (2018).
37. M. S. Aliroteh, A. Arbabian, Microwave-induced thermoacoustic imaging of subcutaneous vasculature with near-field RF excitation. *IEEE Trans. Microw. Theory Tech.* **66**, 577–588 (2018).
38. K. Tamarov, M. Gongalsky, L. Osminkina, Y. Huang, M. Omar, V. Yakunin, V. Ntziachristos, D. Razansky, V. Timoshenko, Electrolytic conductivity-related radiofrequency heating of aqueous suspensions of nanoparticles for biomedicine. *Phys. Chem. Chem. Phys.* **19**, 11510–11517 (2017).
39. S. Gabriel, R. W. Lau, C. Gabriel, The dielectric properties of biological tissues: III. Parametric models for the dielectric spectrum of tissues. *Phys. Med. Biol.* **41**, 2271–2293 (1996).
40. R. Buchner, J. Barthel, J. Stauber, The dielectric relaxation of water between 0°C and 35°C. *Chem. Phys. Lett.* **306**, 57–63 (1999).

41. J. Aguirre, M. Schwarz, N. Garzorz, M. Omar, A. Buehler, K. Eyerich, V. Ntziachristos, Precision assessment of label-free psoriasis biomarkers with ultra-broadband optoacoustic mesoscopy. *Nat. Biomed.* **1**, 0068 (2017).

42. K. Kawakami, E. E. Patton, M. Orger, *Zebrafish: Methods and Protocols, Methods in Molecular Biology* (Methods and Protocols Second Edition, Springer, 2016), 366 pp.

43. P. A. Hasgall, F. Di Gennaro, C. Baumgartner, E. Neufeld, B. Lloyd, M. C. Gosselin, D. Payne, A. Klingenböck, N. Kuster, IT'IS Database for thermal and electromagnetic parameters of biological tissues. Version 4.0 (2018).

44. C. Lou, S. Yang, Z. Ji, Q. Chen, D. Xing, Ultrashort microwave-induced thermoacoustic imaging: A breakthrough in excitation efficiency and spatial resolution. *Phys. Rev. Lett.* **109**, 218101 (2012).

45. S. Liu, R. Zhang, Y. Luo, Y. Zheng, Magnetoacoustic microscopic imaging of conductive objects and nanoparticles distribution. *J. Appl. Phys.* **122**, 124502 (2017).

46. X. Feng, F. Gao, R. Kishor, Y. Zheng, Coexisting and mixing phenomena of thermoacoustic and magnetoacoustic waves in water. *Sci. Rep.* **5**, 11489 (2015).

47. X. H. Feng, F. Gao, Y. J. Zheng, Magnetically mediated thermoacoustic imaging toward deeper penetration. *Appl. Phys. Lett.* **103**, 083704 (2013).

48. W. Luo, Z. Ji, S. Yang, D. Xing, Microwave-pumped electric-dipole resonance absorption for noninvasive functional imaging. *Phys. Rev. Appl.* **10**, 024044 (2018).

49. J. Li, A. Chekkoury, J. Prakash, S. Glasl, P. Vetschera, B. Koberstein-Schwarz, I. Olefir, V. Gujrati, M. Omar, V. Ntziachristos, Spatial heterogeneity of oxygenation and haemodynamics in breast cancer resolved in vivo by conical multispectral optoacoustic mesoscopy. *Light Sci. Appl.* **9**, 57 (2020).

50. Y. Li, L. Li, L. Zhu, K. Maslov, J. Shi, P. Hu, E. Bo, J. Yao, J. Liang, L. Wang, L. V. Wang, Snapshot photoacoustic topography through an ergodic relay for high-throughput imaging of optical absorption. *Nat. Photonics* **14**, 164–170 (2020).

51. M. P. Murrell, M. E. Welland, S. J. O'Shea, T. M. H. Wong, J. R. Barnes, A. W. McKinnon, M. Heyns, S. Verhaverbeke, Spatially resolved electrical measurements of SiO$_2$ gate oxides using atomic force microscopy. *Appl. Phys. Lett.* **62**, 786–788 (1993).

52. X. L. Deán-Ben, V. Ntziachristos, D. Razansky, Effects of small variations of speed of sound in optoacoustic tomographic imaging. *Med. Phys.* **41**, 073301 (2014).

53. H. Yang, D. Jüstel, J. Prakash, V. Ntziachristos, Modeling the variation in speed of sound between couplant and tissue improves the spectral accuracy of multispectral optoacoustic tomography. *Proc. SPIE* **10890**, 1089027 (2019).

54. H. Yang, D. Jüstel, J. Prakash, A. Karlas, A. Helfen, M. Masthoff, M. Wildgruber, V. Ntziachristos, Soft ultrasound priors in optoacoustic reconstruction: Improving clinical vascular imaging. *Photoacoustics* **19**, 100172 (2020).

55. C. S. Widodo, H. Sela, D. R. Santosa, The effect of NaCl concentration on the ionic NaCl solutions electrical impedance value using electrochemical impedance spectroscopy methods. *AIP Conf. Proc.* **2021**, 050003 (2018).

56. R. Feymann, R. B. Leighton, M. Sands, *The Feynman Lectures on Physics* (Addison-Wesley, 1965).

Citation: Y. Huang, M. Omar, W. Tian, H. Lopez-Schier, G. G. Westmeyer, A. Chmyrov, G. Sergiadis, V. Ntziachristos, Noninvasive visualization of electrical conductivity in tissues at the micrometer scale. *Sci. Adv.* **7**, eabd1505 (2021).

Noninvasive visualization of electrical conductivity in tissues at the micrometer scale

Yuanhui HuangMurad OmarWeili TianHernán Lopez-SchierGil Gregor WestmeyerAndriy ChmyrovGeorge SergiadisVasilis Ntziachristos

View the article online
https://www.science.org/doi/10.1126/sciadv.abd1505
Permissions
https://www.science.org/help/reprints-and-permissions

Use of think article is subject to the Terms of service

Science Advances

MAAAS

Supplementary Materials for

Noninvasive visualization of electrical conductivity in tissues at the micrometer scale

Yuanhui Huang, Murad Omar, Weili Tian, Hernán Lopez-Schier, Gil Gregor Westmeyer, Andriy Chmyrov, George Sergiadis, Vasilis Ntziachristos*

*Corresponding author. Email: v.ntziachristos@tum.de

The PDF file includes:

Notes S1 to S6
Table S1
Figs. S1 to S5
Legends for movies S1 to S3
References

Other Supplementary Material for this manuscript includes the following:

(available at advances.sciencemag.org/cgi/content/full/7/20/eabd1505/DC1)

Movies S1 to S3

Supplementary Text

Note S1. RF field distribution / homogeneity and coupling in RThAM

To test our assumption of a homogeneous electric field in the TxLine, we performed simulation studies (see Materials and Methods) of the RF field distribution at 300 MHz using commercial EM simulation software (CST studio), with and without a sample present. Figure S1D shows the result without sample, and fig. S1E shows that with a water-rich sample installed (spherical egg with permittivity of 80.1 and conductivity 1 S/m). Less than 3 dB in E-field inhomogeneity is observed inside the water sample and therefore we assumed the E-field is homogeneous inside aqueous samples. For lower frequencies, the field is expected to be more homogeneous than the simulation. This simulation supported the validity of our choice of an open TxLine for near-field coupling and represented one of the key advantages of this RF coupling method (confirmed with suture in fig. S3, A and B). Compared to other coupling methods (*32, 35–37*), the open TxLine is capable of homogeneously 'concentrating' the pulsed RF energy in a tight 3D space between the two conductor plates. Therefore, for spherical absorbers such homogeneous field distribution in sample chamber would yield homogeneous contrast in RThAM 3D FOV.

We evaluate the coupling efficiency of RF energy to the antenna by the percentage of power that is transmitted through open transmission line and finally absorbed by the 50-ohm terminator. Figure S1C shows the voltage standing wave ratio (VSWR) measured at the input to TxLine with a vector network analyzer (VNA Master MS2036A, Anritsu). The VSWR at 300 MHz of 1.36 indicates >97% power transmission. The pulse energy of our RF pulser $E_{pulse} = V_p^2 / Z_0 \times \tau = (10 \times 10^3 \text{ volt})^2 / 50 \text{ Ohm} \times 1.5 \times 10^{-9}$ second $= 3 \times 10^{-3}$ J, which is 3 mJ. Here V_p is the peak voltage, Z_0 the resistance of RF load, τ the pulse width. As a result, this design of open TxLine enabled RF energy coupling of 0.97×3 mJ $= 2.91$ mJ was coupled through a cross-section of 1×3 mm^2 of TxLine, laying down the foundation to high SNR RThAM signal generation.

The coupling efficiency from open transmission line to tissue, which is in fact the thermoacoustic generation efficiency, can be estimated by the conductivity (σ) loss via Joule heating: $H_0 = \sigma|E|^2$ where E is the electric field strength in dielectric medium that reduces the strength of external electric field by a factor of the dielectric constant ε_r [Chapter 10. Dielectrics, Feynman Lectures on Physics Volume II (*56*)]. Here we applied a simplified electrostatic analysis because we considered the dielectric relaxation of polar molecules to be instantaneous [for water (*40*) the relaxation time is 1.1 ps at 298 K].

Note S2. Coupling media for RF energy and US wave

Table S1 summarizes the theoretical RF field strength decrease and US attenuations in different coupling modes of RThAM using the same open transmission line, with the same dielectric gap, and assuming ideal impedance matching to 50 ohm. We have shown the simulation results in fig. S1 (D to E) to show the electric field strengths in oil and in aqueous egg sample. Inspecting the field strength relative to the peak in the cross-sectional plane shows a decrease of -37 dB at the sample center and -14 dB in the oil region that is undisturbed by the sample. Thus, the simulated field strengths indeed are close to the predicted values, shown in table S1 (obtained by a simplified theoretical analysis considering only the polarization field effect). We note that the difference in the simulated field strengths between the oil and aqueous samples (23 dB) is lower than the predicted difference of 30.29 dB (table S1). However, this difference between the simplified theoretical prediction and simulation does not change the conclusion of table S1 — hybrid coupling is better than either pure oil or pure water coupling in our scenario considering both RF field and US coupling. For finer predictions, we believe it would be necessary to carry out more

detailed modeling, for example by considering the local fields at the conductors' edges, sample properties, imperfections in engineering, etc.

Because the mechanism of RF-induced thermoacoustic generation ($p_0 \approx \Gamma\sigma|E|^2$) relies on the E-field strength to generate detectable thermoacoustic signals, our energy coupling strategy is to maximize the electric field strength (E) established in the coupling medium that supports the sample, as allowed by the output voltage of our pulser and the limiting electric breakdown voltage of the medium. Only impedance matching does not satisfy the requirement and we need to further optimize the portion of energy/strength in the form of electric field relative to magnetic field. However, to combine RF field excitation and US wave detection for high resolution RThAM imaging, one of the challenges lies in coupling the RF field and US wave. Usually, a couplant that is efficient to deliver electric field energy is suboptimal for US wave coupling. For example, if we optimized for US wave coupling, and used de-ionized water as a dielectrics for the open TxLine, the delivered RF field would be a result of the external electric field minus the polarized electric field in water, which results in an RF field that is reduced by the dielectric constant of water, $\varepsilon_r = 80.1$ at 293 K. That is the case in the copper wire characterization experiments (Fig. 1 and fig. S2). We chose de-ionized water as the dielectric to fill the TxLine (dielectric gap 6 mm) in order to optimize for US coupling and biological experiments. This water-filled TxLine has characteristic impedance of 25 ohm and matched with two 25-ohm RF resistors before and after it. It is not 50 ohm because a 50 ohm line will have unrealistic dielectric gap of 110 mm. Since the RThAM generation of copper is strong, this energy coupling element is sufficient. But such TxLine design was found experimentally insufficient to excite detectable RThAM signal from biological tissue. Instead, we chose oil as dielectrics to fill TxLine because of its low dielectric constant (negligible polarization E-field) which gives us in return shorter dielectric gap (1 mm, see Materials and Methods) than a 25-ohm TxLine using de-ionized water, and therefore higher electric field strength and desirable energy flux delivered to sample. But oil-filled TxLine brings challenge in US wave coupling.

Due to viscosity of oil (30 cSt for mineral oil, same for kitchen oil) and low speed of sound (SoS; 900 m/s), oil attenuates US wave strongly. According to Stokes' law of acoustic attenuation, we calculated and showed in fig. S1F the US attenuation in mineral oil (viscosity 30 cSt; specific gravity 870 kg/m^3; SoS 985 m/s; M8410, Sigma Aldrich), silicone oil of 2 cSt (viscosity 2 cSt; specific gravity 872 kg/m^3; SoS 931 m/s; PSF-2cSt, Clearco Products), silicone oil of 0.65 cSt (viscosity 0.65 cSt; specific gravity 760 kg/m^3; SoS 891 m/s; PSF-0.65cSt, Clearco Products), and in de-ionzed water (viscosity 0.89 cSt; specific gravity 980 kg/m^3; SoS 1480 m/s). Water is the best US couplant among all not only because our transducers have been optimized for water immersion applications like biological tissue imaging, but also because water attenuation (0.97 dB/mm at 50 MHz) for US wave is the least among these four couplants. The mineral oil is the worst because it attenuates 20.62 dB/mm for 50 MHz US wave. Between 2-cSt and 0.65-cSt silicone oil we did not choose 0.65-cSt because in this viscosity range silicone oil is volatile in air at room temperature. The 2-cSt silicone oil though has an US attenuation of 5 dB/mm, we manage to mitigate the attenuation by using another de-ionized water bag to couple the RThAM wave generated from biological sample.

Lastly the acoustic impedance difference between de-ionized water/tissue and 2 cSt oil is only 80%, suggesting a negligible transmission loss of 0.83 dB for one transmission. Given tissue-oil and oil-water interfaces, the total transmission loss due to acoustic impedance mismatching would be 1.66 dB. As a result, if given a RThAM wave generated inside a tissue and later reached the surface, assuming the oil path is 1 mm and water/tissue path in sum is 5 mm (the focus of transducer is at 6 mm), the total loss before the RThAM signal is detected by US transducer, is 1.66 dB + 0.97 dB/mm × 5 mm + 5 dB/mm × 1 mm = 11.51 dB which is far less than the 31.66 dB loss when using 2-cSt oil only for US coupling. As

also illustrated in table S1, pure oil coupling induces 38.61-dB total loss, while pure water coupling induces 43.89-dB total loss, among which the hybrid coupling solution demonstrates 20.95-dB total loss—the least among the three coupling modes.

To evaluate the effect of coupling methods in RThAM images, we also characterized the imaging resolution using a NaCl-soaked suture with a diameter of 50 µm, as shown in figs. S3 (A and B). Despite the overall low image contrast, we found that contrast along suture varied by <6 dB and that the narrowest width of suture appeared to be ~50 µm, while in the thicker oil the suture appeared to be ~100 µm in size. This result implies that there is only little difference between the system coupling configurations for resolution characterization if the oil path is <1 mm, justifying the use of water-coupled 25-ohm TxLine to characterize hybrid coupled RThAM imaging resolution. A longer path of silicone oil may deteriorate the resolution of RThAM. However, due to the short path of oil between the sample and water couplant, we did not see obvious effects in the zebrafish embryo sample, in which fine features <38 µm in size are visible in the yolk region (Fig. 2D). Similar fine structures (45 µm) were also observed in fig. S4. In zebrafish larvae measurements, due to the thinner size of the sample, the oil path may increase, resulting in a degradation of resolution. This is why in these experiments the sample bed was brought closer to the water bag so that the oil path is smaller than 1 mm. We therefore considered the difference negligible in resolution between hybrid oil/water coupling and pure water coupling.

Note S3. Skin depth of RF energy into copper

One might ask why copper wire of 50 µm in diameter can give in RThAM image a resolution characterization found to be 23 µm axial and 33 µm lateral resolution in RThAM 50 MHz configuration (Fig. 1). Figure S1G shows a relation between skin depth in copper along frequency of RF energy. Keeping second harmonic thermoacoustic generation in mind, the RF absorption at f_{RF} in conductive matter gives rise to thermoacoustic/RThAM wave of $f_{RThAM} = 2 \times f_{RF}$. If we simplified the detection model, a 50 MHz central frequency transducer detects a RThAM signal of $f_{RThAM} = 50$ MHz. This means the RThAM signal is induced due to a conductive absorption of the 25-MHz RF energy. The layer that absorbs has a thickness of 13 µm, meaning reaching at this depth the RF field strength decreases to 1/e and RF energy to $1/e^2$. In contrast, the apparent lateral FWHM is a result of the cylindrical shape of the copper wire and the limited acceptance angle of the US transducer.

Note S4. RThAM 100 MHz setup and characterization

Figure S2 illustrates the performance in terms of imaging resolution and signal-to-noise ratio (SNR), measured from a pair of copper wires (Ø50 µm) using transducer of 100 MHz central frequency (spherically focused; focus 1.5 mm; diameter 1.5 mm; HFM18, Sonaxis). Figure S2 (A and B) show the xy and yz images of the copper, respectively. Some signal from the background area could be the instant glue we applied to fix the position of copper wire sample. Figure S2C shows the profiles of lines in the yz image which demonstrates the achieved lateral FWHM of 16 µm and axial FWHM of 7 µm. Figure S2D is a temporal sequence of maximum RThAM amplitude showing the 28-dB SNR achieved and the signal frequency components up to 150 MHz. This experiment shows that the resolution of RThAM imaging is scalable and determined only by the applied RF pulse width, f-number and the detection bandwidth of transducer. But before applying RThAM 100 MHz to biological studies, US attenuation in the detection acoustic path would have to be reduced to <10 dB with proper design. The energy coupling element used for this experiment is a 25-ohm open TxLine with de-ionized water as dielectrics (6-mm dielectric gap and 3.5-mm conductor width). The wide gap and polar dielectric medium have substantially reduced the RF field strength (table S1). We tried to image biological samples with this TxLine with 50-MHz transducer but failed to obtain RThAM signals.

In current work, we chose to work with 50 MHz instead in order to guarantee substantial deposition of nanosecond pulsed RF energy offered by silicone oil dielectric, which attenuate US wave at 100 MHz by 20 dB/mm (fig. S1F). But as a result, the total loss of using the optimal hybrid oil/water coupling for RThAM 100 MHz is 49.44 dB (table S1) and thus not applicable for biological imaging experiments. We noticed that the zebrafish larvae images [Fig. 2 (I to K) and fig. S5 (E and F)] seemed worse in resolution than that of embryos [Fig. 2 (A to G) and fig. S4 (A to D)]. We attribute the reason to dispersive attenuation due to longer path of silicone oil (which can be adjusted using the sample bed to keep oil path <1 mm) for the case of larvae than for the case of embryos because larvae are smaller in thickness than embryos thus inducing a longer silicone oil gap between water bag and larvae attenuating more severely the thermoacoustic waves.

Note S5. Acoustic velocity mismatch in oil/water hybrid coupling and reconstruction

We choose an SoS during reconstruction that maximizes images quality by minimizing the influence of acoustic velocity mismatch on image reconstruction. Acoustic velocity mismatch can cause refraction and has been demonstrated (*52, 53*) to induce reconstruction errors in localization, dimensions (smearing and deformation), by creating artefacts, and reducing imaging contrast and resolution, if the velocity mismatch is large or the acoustic paths are long. The effects are significant as well when the SoS varies with detection angle, such as in concaved array detection (*52, 53*), which relies on an SoS map to calculate the distance matrix and sum up the signals accordingly. An incorrect assumption of the SoS could create artefacts that do not exist in sample. In the case of RThAM the velocity mismatch appears large (931 m/s for silicone oil, and 1480 m/s for water), but the oil acts as a layer (<1 mm) between the sample (<1 mm) and water couplant (5 mm). However, the oil path and the sample thickness are very small compared to the water path. Informed by our previous work (*52*), we tried and selected a uniform SoS that is just below that of water, whereby the highest resolution and contrast reconstruction is obtained. In effect, we considered the effect of acoustic velocity mismatch insignificant. However, for higher image quality, precision in quantitative measurements, the acoustic velocity mismatch will have to be considered in a priori reconstructions using SoS and structural information (*53, 54*).

Note S6. Effects of polarized excitation field on RThAM resolution and contrast

We expect the resolution to be symmetric in lateral plane because RThAM resolution is acoustically limited as conventional optoacoustic mesoscopy (*30, 41*). However, for longitudinal absorbers that are thin and long such as muscle or neural fibers, the polarized electric field would represent the contrast differently depending on the relative orientation of the fibers to the polarization of the field. Such asymmetric contrast can be understood at the level of charge carriers. For aligned orientation, the charge carriers would be accelerated by the RF field for longer distance along the fiber, i.e., larger converted and absorbed kinetic energy, while for the orientation perpendicular to the field polarization the absorbed RF energy is minimum. Future applications and interpretation of the RThAM contrast would need to consider this asymmetry effect.

To confirm, we have made another measurement using copper wire of 100 μm in diameter (fig. S3, C to E). For such experiments carbon fibers are interesting but we did not use carbon fiber (5–10 μm diameter) because its diameter is too small for current RThAM 50 MHz setup and the corresponding high central frequency US (~200 MHz) attenuates too severely for RThAM 100 MHz in hybrid oil/water coupling. Upon improvements in excitation energy density and acoustic coupling efficiency, carbon fiber should serve as a standard resolution target for thermoacoustic microscopy. The copper phantom results shown in fig. S3 (C to E) confirmed the homogeneous in-plane resolution, which is limited by acoustic diffraction and scanning step of the used transducer. The size (100 μm) of copper wires was correctly represented in

RThAM image for both orientation along x and y axis. As expected, the image showed clearly higher contrast from the wire orientation that is parallel to the field polarization compared to the perpendicular orientation.

Supplementary Table

Table S1. Coupling mode comparison: pure oil, pure water, hybrid oil/water at 50 and 100 MHz assuming same dielectric gap and ideal impedance matching.

| Coupling method	Permittivity ε_r	Polarization induced net field energy decrease $1/\varepsilon_r^2$	US trans. loss at interface(s)	100 MHz US attenuation dB/mm × length	100 MHz Total attenuation	50 MHz US attenuation dB/mm × length	50 MHz Total attenuation
Pure oil	2.45	-7.78 dB	-0.83 dB	-20×6 = -120 dB	**-128.61 dB**	-5×6 mm = -30 dB	**-38.61 dB**
Pure water	80.1	-38.07 dB	0	-4×6 mm = -24 dB	**-62.07 dB**	-0.97×6 mm = -5.82 dB	**-43.89 dB**
Hybrid oil/water	2.45	-7.78 dB	-0.83×2 dB	-4×5 - 20×1 = -40 dB	**-49.44 dB**	-0.97×5 - 5×1 = -11.51 dB	**-20.95 dB**

Supplementary Figure
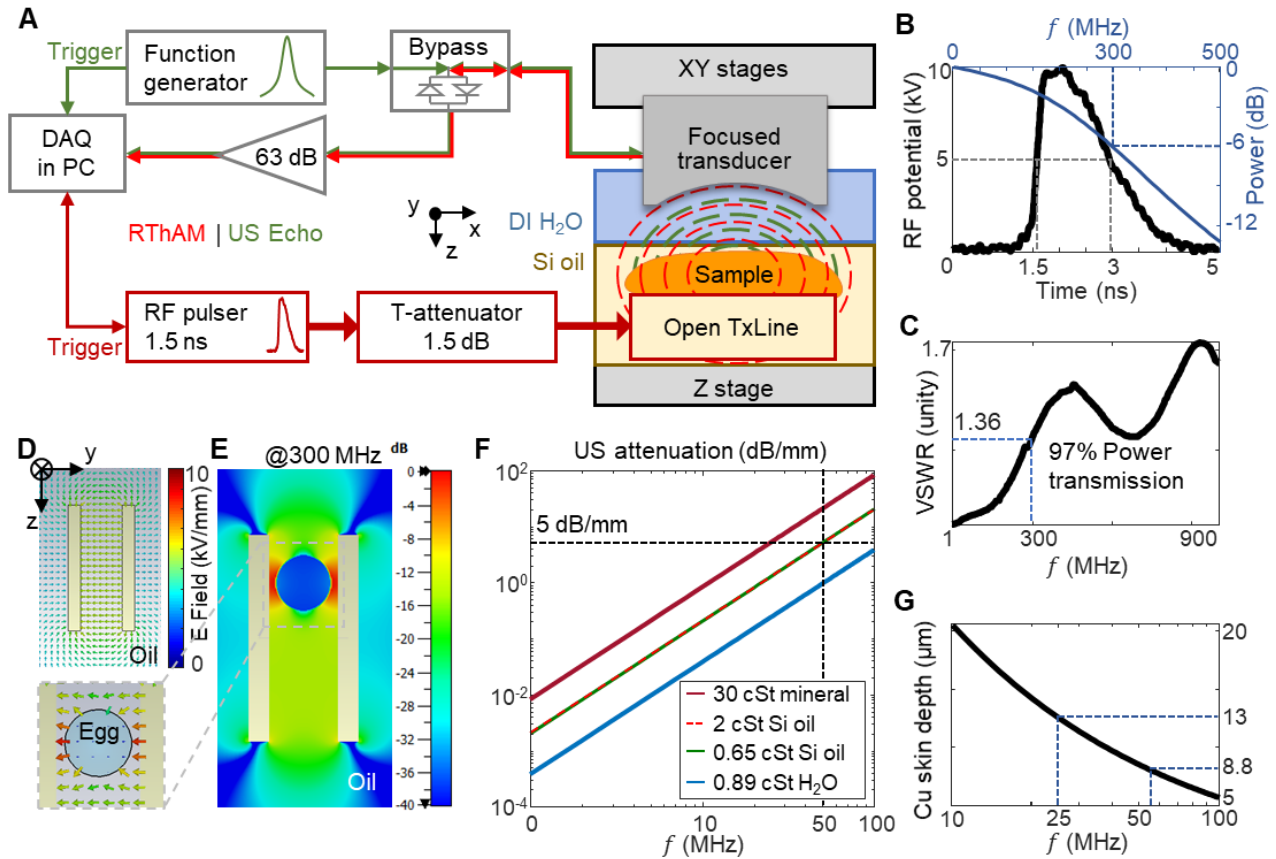
Fig. S1. Schematic and characteristics of RThAM setup. (**A**) Diagram of the RThAM setup. RF pulser generates 5–10 kV, 1.5 ns pulses which are coupled via coaxial cable to the sample in between the open TxLine. Conductive sample that absorbs the RF energy, generates acoustic wave (RThAM signal; dashed red arcs) due to thermoacoustic effect. The RThAM waves are coupled by de-ionized water (DI H_2O) to a spherically focused US transducer. The RThAM signal is amplified by a 63-dB amplifier and digitized by a data acquisition card (DAQ) in a personal computer (PC). The DAQ is triggered by either the RF pulser or function generator used in active US imaging. The PC synchronizes the setup, scans the stages to perform raster scan in the xy plane, stores and reconstructs the images. The custom-built bypass circuit is inserted to allow for ultrasonography using function generator exciting US emission in transducer. (**B**) A profile of RF pulse (black) showing the pulse width of 1.5 ns. The Fourier transform of RF pulse (blue) showing -6 dB cut-off frequency at 300 MHz. (**C**) The measured VSWR with a sample installed in the open TxLine to show the matched impedance for RF energy transmission below 300 MHz. (**D and E**) The EM simulation results at 300 MHz showing (**D**) E-field strength distribution in oil couplant without sample and (**E**) with the 'Egg' sample (permittivity of 80.1; conductivity 1 S/m) installed. (**F**) US attenuation below 100 MHz at room temperature in couplants with different viscosity: 30-cSt mineral oil, 2- and 0.65-cSt silicone oil, and 0.89-cSt water. At 50 MHz, US attenuation in silicone oil is 5 dB/mm, and in water is less than 1 dB/mm. (**G**) Skin depth in copper (Cu) of RF below 100 MHz. At 25 MHz, corresponding to 50-MHz RThAM signal, the skin depth is 13 μm (8.8 μm for RF at 54.5 MHz) beyond which only $1/e^2$ energy is left.
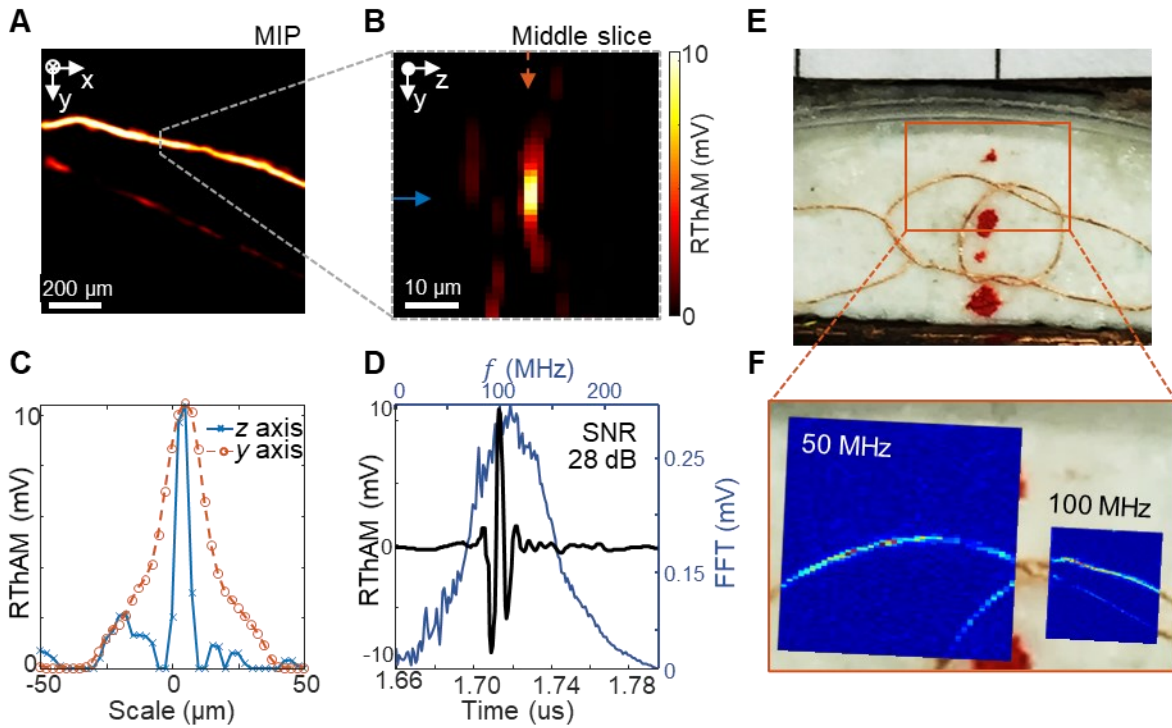
Fig. S2. RThAM 100 MHz performance characterization. (**A** and **B**) RThAM image of a pair of ⌀ 50 µm copper wires in the *xy* plane (**A**) and in the *yz* plane (**B**). Signals from background could be a result from the instant glue applied to keep the wires in position. The dotted grey line in (A), indicates the cross-sectional *yz* image shown in (B). Scale bar in (A) is 200 µm and in (B) 10 µm. The solid blue and dashed orange arrows in (B) indicates the *z*-axial and *y*-axial profile shown in (C), respectively. (**C**) 7 µm axial resolution and 16 µm lateral resolution shown by the *z*-axis (solid blue with cross marker) and *y*-axis (dashed orange with circle marker) profiles along the lines indicated in (B), respectively. (**D**) A temporal signal (black) of 28 dB signal-to-noise ratio and its Fourier transform (blue) showing frequency components and central frequency at 109 MHz. (**E** and **F**) A photograph of the copper phantom used for resolution characterization experiments (E) with RThAM 50 MHz image (jet colormap version of Fig. 1B) overlaid on the left and RThAM 100 MHz [jet colormap version of (A)] on the right in (F). Photo Credit: Yuanhui Huang, TUM.
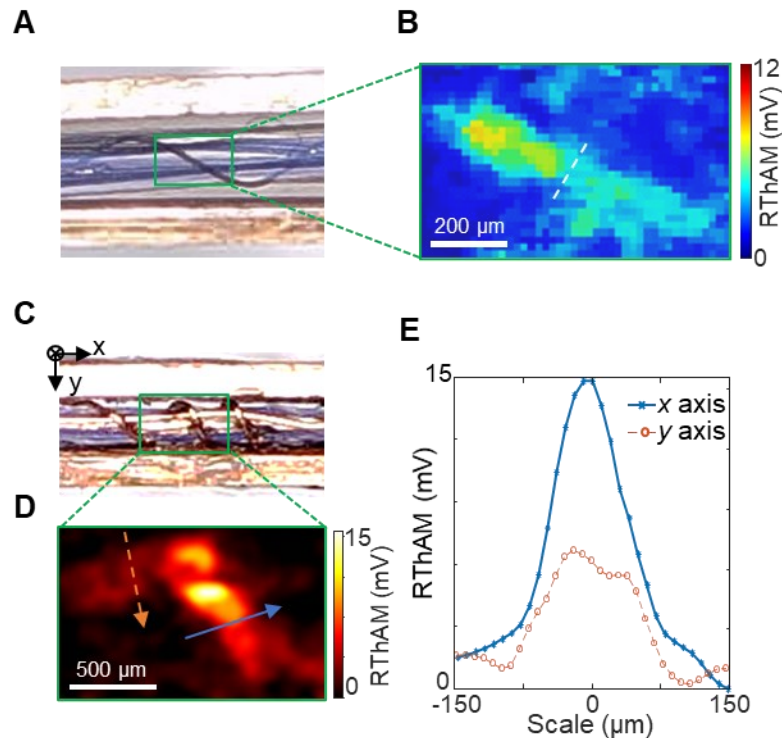
Fig. S3. Saline-soaked suture and copper in RThAM 50 MHz using hybrid oil/water coupling. (A and B) A suture (polyamide ⌀50 µm) wrapped around a tubing (⌀800 µm) showing the in-plane resolution in hybrid oil/water coupling. The suture phantom was soaked in 10% w/v NaCl solution [1.7 mM; ~28.86 S/m according to Widodo *et al.* (*55*)] for two hours and placed wet in the open transmission line. **(A)** An optical photo showing the imaged suture extending into the sample space, with central segment affected by a shorter oil path. **(B)**. The RThAM image showing the small variations in the contrast of the suture. The slight background contrast may result from the residual NaCl saline on the surface of tubing. Note that the narrowest part (dashed white line) of the phantom was measured to be ~50 µm in width. **(C to E)** A coil of copper wire (⌀100 µm) wrapped around tubing (⌀600 µm) showing the polarization effect of the electric field depending on the orientation of sample. **(C)** An optical photo showing the imaged "cross" in the copper coil phantom in hybrid oil/water coupling. **(D)**. The RThAM image showing the cross with similar size but different contrast intensity because of the polarized excitation field. The arrows indicate the profiles shown in (E). **(E)** Profiles along arrows indicated in (B) showing the relative contrast and apparent size of sample with orientations perpendicular (*x* axis; solid blue) and parallel (*y* axis; dotted orange) to the field polarization. Photo Credit: Yuanhui Huang, TUM.
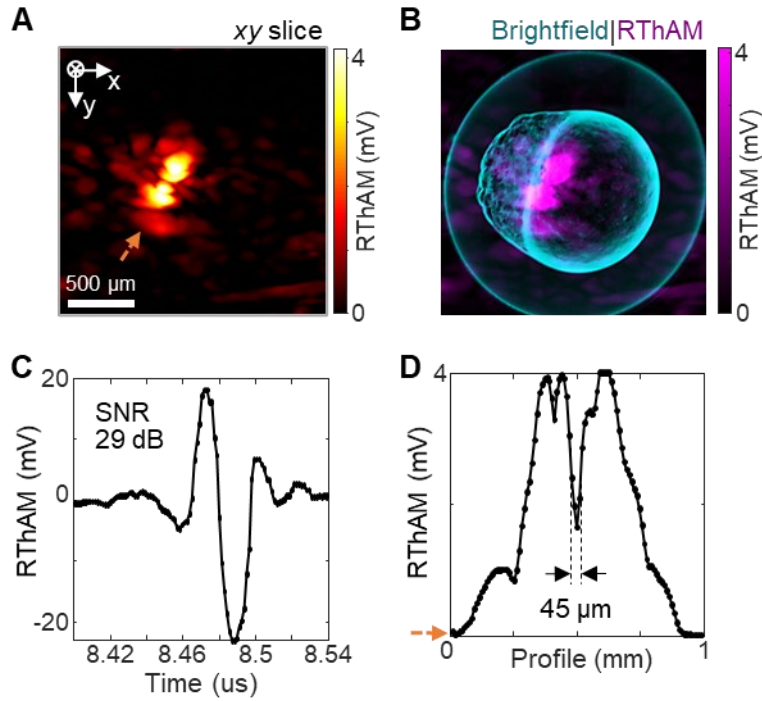
Fig. S4. RThAM cross-section in depth and profile. (**A**) A cross-sectional RThAM image of the embryo four hpf shown in Fig. 2 (E to H). The image is formed by using a middle slice (200 µm) in the *z*-axis direction along arrows indicated in Fig. 2H. Dotted orange arrow indicates the profile analyzed in (D). (**B**) An overlay of RThAM image slice onto the microphotograph of the embryo showing strong RF absorption on the interface of blastomeres and the yolk. (**C**) An example RThAM signal, showing the achieved 29-dB SNR in cells. The signal was taken from the maximum pixel in Fig. 2F. (**D**) The line profile indicated in (A), showing the relative RF absorption in the embryo and the resolution power down to 45 µm.
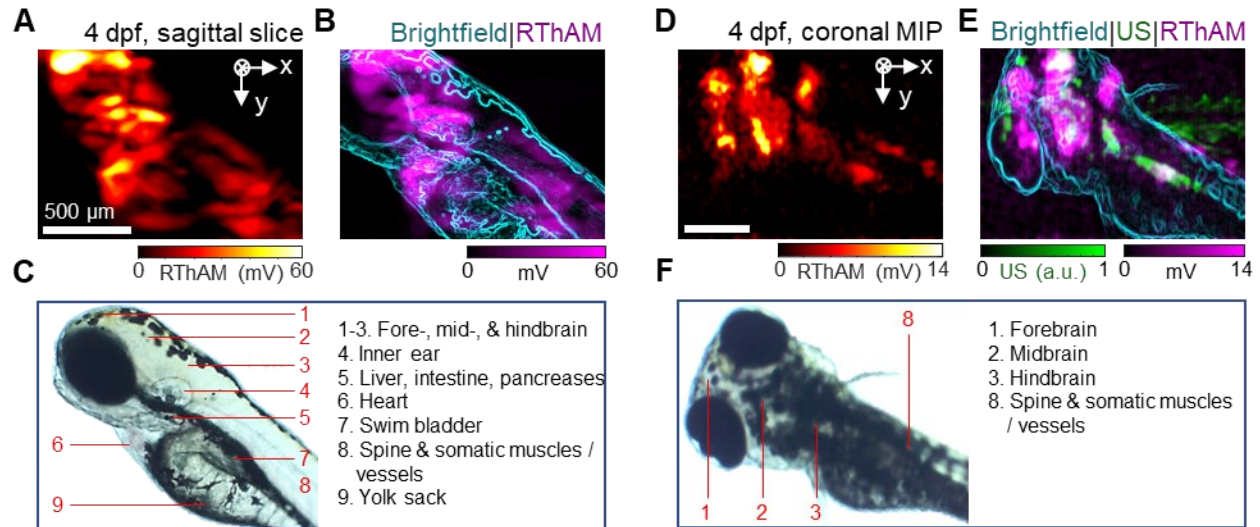
Fig. S5. RThAM imaging on wild type zebrafish larvae of four dpf. (**A** to **C**) Larva in the sagittal position. (**A**) RThAM slice (~150 μm in thickness) at the depth of the spinal cord in a hot map of the zebrafish in sagittal view showing the major contrast from the head, abdomen, and trunk region. (**B**) An overlay of the RThAM slice (magenta) onto the reflection-mode optical image (bright field; edge filtered; cyan). (**C**) A bright-field microphotograph of the zebrafish larva with annotation of major anatomical features. (**D** to **F**) Larva in the coronal (see 3D distribution in movie S3) position. (**D**) The RThAM MIP in hot map of the zebrafish in coronal position showing the major contrast from the head, abdomen, and trunk region. (**E**) An overlay of the RThAM MIP (magenta), US pulse-echo image (green), and the bright field microphotograph (cyan, edge filtered) showing coregistered features in hybrid appearance. The whitish areas are a result of blending magenta and green, i.e., the overlapping area between RThAM and US contrast. (**F**) Bright-field microphotograph of the larva in coronal position with annotation of major anatomical features in the view. Scale bars are 500 μm.

Supplementary Movie Caption

Movie S1. RThAM 3D of zebrafish embryo at 1 cell stage. Dual-mode RThAM/US imaging of the same sample as Fig. 2 (A to D) at 0.5 hpf. The mesh sphere is added manually for localization purpose using ImageJ. The flat object is the polyethylene film used as water bag. The simultaneous dual-mode 3D image renders RThAM contrast in red and US pulse-echo contrast in green.

Movie S2. RThAM 3D of zebrafish embryo at 512 cell stage. Dual-mode RThAM/US imaging of the same sample as Fig. 2 (E to H) at 4 hpf. The mesh sphere is added manually for localization purpose using ImageJ. The flat object is the polyethylene film used as water bag. The simultaneous dual-mode 3D image renders RThAM contrast in red and US pulse-echo contrast in green.

Movie S3. RThAM 3D of wildtype zebrafish larva at 4 dpf. Dual-mode RThAM/US imaging of the same sample as supplementary fig. S5 (D to F). The simultaneous dual-mode 3D image renders RThAM contrast in red and US pulse-echo contrast in green. Some US contrast can also be seen from the exposed part of sample bed (tubing used to support the sample), and from copper plates of open transmission line.

REFERENCES AND NOTES

1. M. Dressel, M. Scheffler, Verifying the Drude response. *Ann. Phys.* **15**, 535–544 (2006).

2. P. Grasland-Mongrain, C. Lafon, Review on biomedical techniques for imaging electrical impedance. *IRBM* **39**, 243–250 (2018).

3. J. Matthias, J. Maul, R. Noster, H. Meinl, Y.-Y. Chao, H. Gerstenberg, F. Jeschke, G. Gasparoni, A. Welle, J. Walter, K. Nordström, K. Eberhardt, D. Renisch, S. Donakonda, P. Knolle, D. Soll, S. Grabbe, N. Garzorz-Stark, K. Eyerich, T. Biedermann, D. Baumjohann, C. E. Zielinski, Sodium chloride is an ionic checkpoint for human T_H2 cells and shapes the atopic skin microenvironment. *Sci. Transl. Med.* **11**, eaau0683 (2019).

4. D. Haemmerich, S. T. Staelin, J. Z. Tsai, S. Tungjitkusolmun, D. M. Mahvi, J. G. Webster, In vivo electrical conductivity of hepatic tumours. *Physiol. Meas.* **24**, 251–260 (2003).

5. V. D. Schepkin, F. C. Bejarano, T. Morgan, S. Gower-Winter, M. Ozambela Jr, C. W. Levenson, In vivo magnetic resonance imaging of sodium and diffusion in rat glioma at 21.1 T. *Magn. Reson. Med.* **67**, 1159–1166 (2012).

6. D. M. Gordon, S. R. Ash, Lack of correlation of glucose levels in filtered blood plasma to density and conductivity measurements. *ASAIO J.* **55**, 227–230 (2009).

7. M. Schaefer, W. Gross, J. Ackemann, M. M. Gebhard, The complex dielectric spectrum of heart tissue during ischemia. *Bioelectrochemistry* **58**, 171–180 (2002).

8. T. J. Jentsch, C. A. Hubner, J. C. Fuhrmann, Ion channels: Function unravelled by dysfunction. *Nat. Cell Biol.* **6**, 1039–1047 (2004).

9. F. Manoni, L. Fornasiero, M. Ercolin, A. Tinello, M. Ferrian, S. Valverde, G. Gessoni, Laboratory diagnosis of renal failure: Urine conductivity and tubular function. *Minerva Urol. Nefrol.* **61**, 17–20 (2009).

10. E. Neher, B. Sakmann, Single-channel currents recorded from membrane of denervated frog muscle fibres. *Nature* **260**, 799–802 (1976).

11. A. L. Hodgkin, A. F. Huxley, Propagation of electrical signals along giant nerve fibres. *Proc. R. Soc. Lond B* **140**, 177–183 (1952).

12. J. Abbott, T. Ye, K. Krenek, R. S. Gertner, S. Ban, Y. Kim, L. Qin, W. Wu, H. Park, D. Ham, A nanoelectrode array for obtaining intracellular recordings from thousands of connected neurons. *Nat. Biomed. Eng.* **4**, 232–241 (2019).

13. P. K. Hansma, B. Drake, O. Marti, S. A. Gould, C. B. Prater, The scanning ion-conductance microscope. *Science* **243**, 641–643 (1989).

14. X. D. Cui, A. Primak, X. Zarate, J. Tomfohr, O. F. Sankey, A. L. Moore, T. A. Moore, D. Gust, G. Harris, S. M. Lindsay, Reproducible measurement of single-molecule conductivity. *Science* **294**, 571–574 (2001).

15. R. H. Bayford, Bioimpedance tomography (electrical impedance tomography). *Annu. Rev. Biomed. Eng.* **8**, 63–91 (2006).

16. E. Boto, N. Holmes, J. Leggett, G. Roberts, V. Shah, S. S. Meyer, L. D. Muñoz, K. J. Mullinger, T. M. Tierney, S. Bestmann, G. R. Barnes, R. Bowtell, M. J. Brookes, Moving magnetoencephalography towards real-world applications with a wearable system. *Nature* **555**, 657–661 (2018).

17. N. Vogt, Voltage sensors: Challenging, but with potential. *Nat. Methods* **12**, 921–924 (2015).

18. E. S. Boyden, F. Zhang, E. Bamberg, G. Nagel, K. Deisseroth, Millisecond-timescale, genetically targeted optical control of neural activity. *Nat. Neurosci.* **8**, 1263–1268 (2005).

19. W. Akemann, H. Mutoh, A. Perron, J. Rossier, T. Knöpfel, Imaging brain electric signals with genetically targeted voltage-sensitive fluorescent proteins. *Nat. Methods* **7**, 643–649 (2010).

20. G. Cao, J. Platisa, V. A. Pieribone, D. Raccuglia, M. Kunst, M. N. Nitabach, Genetically targeted optical electrophysiology in intact neural circuits. *Cell* **154**, 904–913 (2013).

21. Y. Gong, M. J. Wagner, J. Zhong Li, M. J. Schnitzer, Imaging neural spiking in brain tissue using FRET-opsin protein voltage sensors. *Nat. Commun.* **5**, 3674 (2014).

22. V. S. Sohal, F. Zhang, O. Yizhar, K. Deisseroth, Parvalbumin neurons and gamma rhythms enhance cortical circuit performance. *Nature* **459**, 698–702 (2009).

23. H. J. Lee, D. Zhang, Y. Jiang, X. Wu, P.-Y. Shih, C.-S. Liao, B. Bungart, X.-M. Xu, R. Drenan, E. Bartlett, J.-X. Cheng, Label-free vibrational spectroscopic imaging of neuronal membrane potential. *J. Phys. Chem. Lett.* **8**, 1932–1936 (2017).

24. R. Schirhagl, K. Chang, M. Loretz, C. L. Degen, Nitrogen-vacancy centers in diamond: Nanoscale sensors for physics and biology. *Annu. Rev. Phys. Chem.* **65**, 83–105 (2014).

25. C.-C. Fu, H.-Y. Lee, K. Chen, T.-S. Lim, H.-Y. Wu, P.-K. Lin, P.-K. Wei, P.-H. Tsao, H.-C. Chang, W. Fann, Characterization and application of single fluorescent nanodiamonds as cellular biomarkers. *Proc. Natl. Acad. Sci. U.S.A.* **104**, 727–732 (2007).

26. N. K. Nikolova, Microwave imaging for breast cancer. *IEEE Microw. Mag.* **12**, 78–94 (2011).

27. P. Wang, Z. Li, P. Liu, Y. Pei, Super resolution in depth for microwave imaging. *Appl. Phys. Lett.* **115**, 044101 (2019).

28. T. Voigt, U. Katscher, O. Doessel, Quantitative conductivity and permittivity imaging of the human brain using electric properties tomography. *Magn. Reson. Med.* **66**, 456–466 (2011).

29. T. Bowen, Radiation-induced thermoacoustic soft tissue imaging, in *Proceedings of the 1981 Ultrasonics Symposium*, Chicago, IL, USA, 14 to 16 October 1981.

30. M. Omar, J. Aguirre, V. Ntziachristos, Optoacoustic mesoscopy for biomedicine. *Nat. Biomed. Eng.* **3**, 354–370 (2019).

31. R. A. Kruger, K. D. Miller, H. E. Reynolds, W. L. Kiser Jr., D. R. Reinecke, G. A. Kruger, Breast cancer in vivo: Contrast enhancement with thermoacoustic CT at 434 MHz-feasibility study. *Radiology* **216**, 279–283 (2000).

32. M. Omar, S. Kellnberger, G. Sergiadis, D. Razansky, V. Ntziachristos, Near-field thermoacoustic imaging with transmission line pulsers. *Med. Phys.* **39**, 4460–4466 (2012).

33. L. Nie, D. Xing, Q. Zhou, D. Yang, H. Guo, Microwave-induced thermoacoustic scanning CT for high-contrast and noninvasive breast cancer imaging. *Med. Phys.* **35**, 4026–4032 (2008).

34. C. C. Johnson, A. W. Guy, Nonionizing electromagnetic wave effects in biological materials and systems. *Proc. IEEE* **60**, 692–718 (1972).

35. D. Razansky, S. Kellnberger, V. Ntziachristos, Near-field radiofrequency thermoacoustic tomography with impulse excitation. *Med. Phys.* **37**, 4602–4607 (2010).

36. Y. Huang, S. Kellnberger, G. Sergiadis, V. Ntziachristos, Blood vessel imaging using radiofrequency-induced second harmonic acoustic response. *Sci. Rep.* **8**, 15522 (2018).

37. M. S. Aliroteh, A. Arbabian, Microwave-induced thermoacoustic imaging of subcutaneous vasculature with near-field RF excitation. *IEEE Trans. Microw. Theory Tech.* **66**, 577–588 (2018).

38. K. Tamarov, M. Gongalsky, L. Osminkina, Y. Huang, M. Omar, V. Yakunin, V. Ntziachristos, D. Razansky, V. Timoshenko, Electrolytic conductivity-related radiofrequency heating of aqueous suspensions of nanoparticles for biomedicine. *Phys. Chem. Chem. Phys.* **19**, 11510–11517 (2017).

39. S. Gabriel, R. W. Lau, C. Gabriel, The dielectric properties of biological tissues: III. Parametric models for the dielectric spectrum of tissues. *Phys. Med. Biol.* **41**, 2271–2293 (1996).

40. R. Buchner, J. Barthel, J. Stauber, The dielectric relaxation of water between 0°C and 35°C. *Chem. Phys. Lett.* **306**, 57–63 (1999).

41. J. Aguirre, M. Schwarz, N. Garzorz, M. Omar, A. Buehler, K. Eyerich, V. Ntziachristos, Precision assessment of label-free psoriasis biomarkers with ultra-broadband optoacoustic mesoscopy. *Nat. Biomed.* **1**, 0068 (2017).

42. K. Kawakami, E. E. Patton, M. Orger, *Zebrafish: Methods and Protocols, Methods in Molecular Biology* (Methods and Protocols Second Edition, Springer, 2016), 366 pp.

43. P. A. Hasgall, F. Di Gennaro, C. Baumgartner, E. Neufeld, B. Lloyd, M. C. Gosselin, D. Payne, A. Klingenböck, N. Kuster, IT'IS Database for thermal and electromagnetic parameters of biological tissues. Version 4.0 (2018).

44. C. Lou, S. Yang, Z. Ji, Q. Chen, D. Xing, Ultrashort microwave-induced thermoacoustic imaging: A breakthrough in excitation efficiency and spatial resolution. *Phys. Rev. Lett.* **109**, 218101 (2012).

45. S. Liu, R. Zhang, Y. Luo, Y. Zheng, Magnetoacoustic microscopic imaging of conductive objects and nanoparticles distribution. *J. Appl. Phys.* **122**, 124502 (2017).

46. X. Feng, F. Gao, R. Kishor, Y. Zheng, Coexisting and mixing phenomena of thermoacoustic and magnetoacoustic waves in water. *Sci. Rep.* **5**, 11489 (2015).

47. X. H. Feng, F. Gao, Y. J. Zheng, Magnetically mediated thermoacoustic imaging toward deeper penetration. *Appl. Phys. Lett.* **103**, 083704 (2013).

48. W. Luo, Z. Ji, S. Yang, D. Xing, Microwave-pumped electric-dipole resonance absorption for noninvasive functional imaging. *Phys. Rev. Appl.* **10**, 024044 (2018).

49. J. Li, A. Chekkoury, J. Prakash, S. Glasl, P. Vetschera, B. Koberstein-Schwarz, I. Olefir, V. Gujrati, M. Omar, V. Ntziachristos, Spatial heterogeneity of oxygenation and haemodynamics in breast cancer resolved in vivo by conical multispectral optoacoustic mesoscopy. *Light Sci. Appl.* **9**, 57 (2020).

50. Y. Li, L. Li, L. Zhu, K. Maslov, J. Shi, P. Hu, E. Bo, J. Yao, J. Liang, L. Wang, L. V. Wang, Snapshot photoacoustic topography through an ergodic relay for high-throughput imaging of optical absorption. *Nat. Photonics* **14**, 164–170 (2020).

51. M. P. Murrell, M. E. Welland, S. J. O'Shea, T. M. H. Wong, J. R. Barnes, A. W. McKinnon, M. Heyns, S. Verhaverbeke, Spatially resolved electrical measurements of SiO_2 gate oxides using atomic force microscopy. *Appl. Phys. Lett.* **62**, 786–788 (1993).

52. X. L. Deán-Ben, V. Ntziachristos, D. Razansky, Effects of small variations of speed of sound in optoacoustic tomographic imaging. *Med. Phys.* **41**, 073301 (2014).

53. H. Yang, D. Jüstel, J. Prakash, V. Ntziachristos, Modeling the variation in speed of sound between couplant and tissue improves the spectral accuracy of multispectral optoacoustic tomography. *Proc. SPIE* **10890**, 1089027 (2019).

54. H. Yang, D. Jüstel, J. Prakash, A. Karlas, A. Helfen, M. Masthoff, M. Wildgruber, V. Ntziachristos, Soft ultrasound priors in optoacoustic reconstruction: Improving clinical vascular imaging. *Photoacoustics* **19**, 100172 (2020).

55. C. S. Widodo, H. Sela, D. R. Santosa, The effect of NaCl concentration on the ionic NaCl solutions electrical impedance value using electrochemical impedance spectroscopy methods. *AIP Conf. Proc.* **2021**, 050003 (2018).

56. R. Feymann, R. B. Leighton, M. Sands, *The Feynman Lectures on Physics* (Addison-Wesley, 1965).